Metal/Ligand Interactions in Metal Oxide Surfaces and Nanostructures

Jihan Lubani

Université Fédérale
Toulouse Midi-Pyrénées

THÈSE

En vue de l'obtention du
DOCTORAT DE L'UNIVERSITÉ DE TOULOUSE

Délivré par l'Université Toulouse 3 - Paul Sabatier

Cotutelle internationale: Universita Degli Studi Di Perugia

Présentée et soutenue par

Jihan LUBANI

Le 8 juin 2022

Interactions métal/ligand à la surface doxydes métalliques et de nanostructures

---

Ecole doctorale : **SDU2E - Sciences de l'Univers, de l'Environnement et de l'Espace**

Spécialité : **Surfaces et interfaces continentales, Hydrologie**

Unité de recherche :
GET - Geosciences Environnement Toulouse

Thèse dirigée par
Marc BLANCHARD et Filippo DE ANGELIS

Jury

Mme Claudia DRAGONETTI, Examinatrice
M. Marc BLANCHARD, Directeur de thèse
M. Filippo DE ANGELIS, Co-directeur de thèse
M. Luigi VACCARO, Président

Università degli Studi di Perugia and **Université Paul Sabatier**

PhD thesis in Chemical Sciences

Academic year 2021/2022

METAL/LIGAND INTERACTIONS IN METAL OXIDE SURFACES AND NANOSTRUCTURES

Jihan Lubani

Tutors

Filippo De Angelis (Full Professor)

Simona Fantacci (Senior Rsearcher)

Marc Blanchard (CNRS Research Director)

Merlin Méheut (Senior Researcher)

Coordinator of Doctoral School

Prof. Luigi Vaccaro

Résumé

En géochimie environnementale, l'augmentation de la production et des applications des nanoparticules de ZnO entraîne une augmentation de leur rejet dans l'environnement. Bien que l'on sache que les nanoparticules sont de plus en plus utilisées dans différents domaines de l'activité humaine, la quantification de leur libération dans l'environnement est assez difficile en raison des données limitées sur leur prévalence actuelle et prévue dans les produits commerciaux. Les difficultés techniques associées à la quantification des niveaux de nanoparticules de ZnO dans l'environnement ont conduit à la nécessité de prédire les concentrations environnementales en fonction de la pénétration du marché des nanomatériaux, de l'utilisation connue des produits ainsi que du devenir/comportement. Une fois rejetées dans l'environnement, les nanoparticules de ZnO peuvent présenter différents comportements. Dans ce travail, nous avons concentré notre étude théorique sur l'évaluation de l'effet de surface sur la signature isotopique afin d'identifier si les nanoparticules de ZnO ont une composition isotopique de Zn différente des cristaux de ZnO massifs dans des conditions d'équilibre. La structure cristalline de ZnO, des modèles de surface et des nanoparticules sont les trois types de modèles structuraux qui sont considérés pour discuter de l'effet de surface et des propriétés isotopiques des nanoparticules de ZnO. Les propriétés isotopiques sont déterminées à partir des fréquences vibrationnelles par la détermination des rapports de fonction de partition réduits (facteurs β). Nous avons optimisé la structure de ZnO et nous avons calculé les fréquences vibrationnelles sur cette structure afin de déterminer le

facteur de fractionnement à l'équilibre pour le Zn. La valeur du facteur β pour le volume de ZnO où les atomes de Zn sont coordonnés quatre fois avec les atomes d'O est de 3,96 ‰ à 273 K. La rigidité des liaisons interatomiques qui contrôlent le facteur β a été évaluée par la constante de force interatomique (190 Ry/ bohr²). Nous avons ensuite étudié les surfaces $(1\,0\,\bar{1}\,0)$ et $(2\,\bar{1}\,\bar{1}\,0)$ à l'aide de modèles de « slab » périodiques. Pour les deux modèles, les facteurs β de Zn montrent des résultats très similaires à ceux de la structure cristalline, cependant, les atomes de Zn de surface affichent des facteurs β plus élevés. Ce fractionnement s'explique par le changement de coordination de quatre dans la structure en masse à trois à la surface. Cette sous-coordination des atomes de Zn à la surface provoque le raccourcissement des liaisons Zn-O et l'augmentation des facteurs β. Les facteurs β augmentent proportionnellement à la constante de force interatomique. Cette relation reflète la forte dépendance du fractionnement isotopique avec les constantes de force interatomique. Les mêmes surfaces $(1\,0\,\bar{1}\,0)$ et $(2\,\bar{1}\,\bar{1}\,0)$ ont été utilisées pour explorer l'interaction et l'adsorption de l'eau sur ces surfaces. Cette adsorption permet la coordination complète des atomes de Zn de surface et donc le nombre de coordination est de 4 pour tous les atomes Zn de la surface, ce qui se traduit par une uniformisation des facteurs β entre la surface et l'intérieur du cristal. De plus, nous avons étudié une nanoparticule de ZnO constituée de la surface polaire (0001) en haut et en bas et de la surface apolaire $(1\,0\,\bar{1}\,0)$ sur les côtés. Nous avons adsorbé des molécules d'eau sur la surface (0001), afin de saturer les atomes de surface sous-coordonnés et en même temps de minimiser le dipôle le long de l'axe c. Les résultats des nanoparticules sont cohérents avec ceux dérivés des calculs effectués sur les modèles de surface, avec de petites variations dues à une relaxation structurelle plus importante dans le calcul des nanoparticules. La corrélation entre les facteurs β et les constantes de force pour cette nanoparticule est la même que pour les modèles précédents. Cela suit la règle générale des liaisons courtes concentrant les isotopes lourds. Notre modélisation d'une nanoparticule de ZnO suggère que cet effet de surface peut avoir un impact sur la signature isotopique globale des plus petites nanoparticules. Dans la structure ZnO, la relaxation de surface n'affecte que les deux premières couches atomiques, ne se propage pas loin dans la structure, limitant l'effet de surface sur la signature isotopique. Nous pouvons nous attendre à trouver des effets de surface plus importants dans les matériaux présentant une forte relaxation de surface, avec des éléments chimiques associés à de grandes variations isotopiques, et avec éventuellement des processus d'oxydoréduction liées à les surfaces des nanoparticules.

Dans le domaine du patrimoine culturel, l'oxyde de zinc (ZnO) est un pigment blanc typique des peintures qui se dégrade dans l'huile en formant des savons métalliques ; ce sont en général des complexes d'ions zinc avec des acides gras à longue chaîne qui proviennent du processus de vieillissement du liant huileux. Il a été émis l'hypothèse que la dégradation du ZnO est initialisée par l'interaction du pigment ZnO avec les fonctionnalités carboxyliques formées par les réactions d'auto-oxydation. Compte tenu de l'incertitude qui existe encore dans le mécanisme de dégradation atomistique du ZnO et de son importance pour la conservation des œuvres d'art, il est important de clarifier les différentes étapes du processus de dégradation du ZnO pour aider les restaurateurs à travailler. Dans ce travail, nous avons étudié certaines des étapes clés potentielles du processus de dégradation réactive. Sur la base des données expérimentales disponibles sur les voies de dégradation possibles, une séquence d'intermédiaires plausibles et de voies de réaction est calculée pour estimer la thermodynamique de la réaction et mettre en évidence les mécanismes possibles liés à la stabilité des différents produits de dégradation. Nous nous sommes d'abord concentrés sur l'interaction entre le ZnO et différents acides carboxyliques d'huile qui sont des produits de dégradation courants et pourraient s'adsorber à la surface du ZnO. Nous associons cette étape d'adsorption à l'initialisation de la voie de dégradation puis nous caractérisons les éventuels intermédiaires et produits finaux. À partir du pigment ZnO, nous construisons un cluster qui s'est déjà avéré être un bon modèle pour décrire les propriétés électroniques et optiques du ZnO. Nous nous sommes focalisés sur l'étude de (i) l'interaction entre le ZnO et les acides carboxyliques et les acétates, qui sont des fragments réactifs plausibles de la dégradation de l'huile, et (ii) la formation des produits de dégradation du ZnO, les carboxylates de Zn. Nous avons étudié l'adsorption de l'acide acétique/acétate à la surface de ZnO, dans le milieu de faible polarité, qui peut être considérée comme l'initialisation de la voie de réaction qui conduit à la formation de savon métallique. Nous avons optimisé l'adsorption de l'acide acétique (AcH) en explorant différents modes d'adsorption pour étudier leur stabilité correspondante. La configuration optimisée la plus stable montre l'acide acétique adsorbé sur deux centres Zn adjacents par une configuration bidentate pontée transférant le proton à un oxygène de la surface ZnO, donc dans un mode d'adsorption dissociative. La configuration la plus stable de l'acétate est celle où les deux acétates coordonnés s'unissent sur des couples Zn différents. Nous nous concentrons sur l'énergétique associée à la liaison de l'acide acétique/acétate à la surface de ZnO, ce qui donne des indications sur l'occurrence de ces processus. Les réactions d'adsorption sont exothermiques prouvant que l'acide acétique et l'acétate chimique s'adsorbent sur la surface de ZnO et que ces systèmes d'adsorption

pourraient être des intermédiaires plausibles des voies réactionnelles globales de la dégradation. De plus, en comparant les différences d'énergie (ΔE) des réactions nous avons trouvé que les systèmes d'adsorption associés à l'acide acétique sont plus favorisés que ceux adsorbant l'acétate. Cette exothermie plus élevée pour l'adsorption de l'acide acétique est le résultat entre l'énergie de la dissociation des protons (étape faiblement endothermique) et celle de l'adsorption des protons (étape fortement exothermique). Nous avons ensuite validé notre approche cluster en optimisant les espèces impliquées dans la réaction d'adsorption la plus favorable, en utilisant une approche avec conditions aux limites périodiques. Les résultats obtenus sont compatibles confirmant ainsi l'adéquation du modèle pour étudier ce type de voie de réactivité. Suite au mécanisme de dégradation hypothétique, les ions zinc migrent de ZnO pendant le séchage de la peinture et se lient aux groupes carboxylate. Nous nous sommes concentrés sur cette étape de dégradation, à savoir la formation de Zn $(AcO)_2$ à partir de l'ion Zn^{2+} libéré de la surface de ZnO et des deux unités d'acétate, qui représentent une phase intermédiaire lors du séchage de l'huile et aboutissent à l'apparition finale de savon métallique. A partir des mêmes réactifs, cluster ZnO et acide acétique/acétate, les produits sont : (i) le cluster ZnO avec une lacune Zn sur la surface laissant le cluster protoné par le transfert de protons de l'acide acétique ou déprotoné en combinaison avec l'acétate, et (ii) le dicarboxylate de Zn. Nous avons optimisé les deux clusters ZnO avec une lacune Zn, en explorant différentes positions de l'ion libéré et des protons à la surface pour les réactions avec les acides, alors qu'aucun proton n'a été ajouté pour les réactions avec l'acétate. Nous avons constaté que les réactions impliquant l'acide acétique sont exothermiques mais elles sont endothermiques pour le cas de l'acétate. Ces valeurs endothermiques sont surestimées en raison de la négligence de l'équilibre de charge sur la surface de ZnO qui, d'autre part, devrait être au moins partiellement présent dans le système réaliste. On peut conclure que les réactions impliquant l'acide acétique sont favorisées par rapport à celles avec l'acétate. En comparant les deux voies de réaction étudiées, nous avons constaté que l'adsorption d'acide acétique/acétate sur la surface de ZnO est thermodynamiquement favorisée par rapport à la libération d'ions Zn^{2+} de la surface pour former des complexes de Zn. Ces résultats sont cohérents avec l'hypothèse selon laquelle la voie de réaction conduisant à la formation de savons métalliques est initiée par l'adsorption d'acide carboxylique/carboxylate à la surface du cluster ZnO. Cette adsorption présente une voie de la réaction globale qui conduit à la formation de savon métallique. Pour évaluer comment la longueur de la chaîne acide affecte l'interaction et la complexation acide-ZnO, nous considérons également l'acide hexanoïque. En suivant la même stratégie appliquée ci-dessus, nous partons de l'acide

hexanoïque/hexanoate et du cluster ZnO comme réactifs. Nous nous concentrons sur les réactions qui conduisent à l'acide hexanoïque@ZnO et à l'hexanoate@ZnO les plus stables en milieu de faible polarité. L'énergétique associée à ces réactions montre une tendance similaire trouvée pour l'acide acétique/acétate. Cependant, les énergies de réaction avec l'acide hexanoïque/hexanoate sont calculées plus grandes que celles analogues impliquant l'acide acétique. L'augmentation de l'exothermicité de ces étapes réactives avec les acides hexanoïques est liée à l'augmentation de la capacité de donneur d'électrons de la chaîne la plus longue. Par conséquent, nous pourrions conclure que la dégradation est favorisée par les acides carboxyliques à chaînes plus longues. L'acide acétique reste cependant un bon modèle pour individualiser les principales étapes réactives de la formation des complexes de Zn. Selon les systèmes optimisés les plus stables étudiés dans la partie précédente, nous avons étudié les réactions de formation des complexes hexanoate Zn. Nous observons que l'adsorption de l'acide hexanoïque/hexanoate sur la surface de ZnO est favorisée par rapport à la libération de l'ion Zn de la surface pour former des complexes de Zn en accord avec les résultats obtenus pour l'acide acétique. Ces deux réactions étudiées représentent un modèle simplifié des étapes clés des voies de dégradation plus complexes du ZnO.

En photocatalyse, des réactions peuvent avoir lieu en utilisant la lumière et un semi-conducteur : dans ce mécanisme, une paire électron-trou est générée lors de l'exposition d'un matériau semi-conducteur à la lumière, puis l'électron excité est utilisé pour réduire une espèce acceptrice tandis que le trou peut simultanément oxyder une espèce donneuse. Les propriétés photocatalytiques du TiO_2 en font un photocatalyseur idéal. Il affiche une énergie de bande interdite élevée et est connu pour rendre le processus de dégradation photocatalytique peu coûteux et facile sous la lumière solaire. Le ZnO a également montré un immense potentiel en tant que photocatalyseurs et présente des propriétés similaires à celles du TiO_2. Ce travail donne un aperçu des effets de la photocatalyse pour dégrader le coronavirus à l'aide de semi-conducteurs à oxyde métallique TiO_2 et ZnO. Dans cette étude préliminaire, nous nous sommes concentrés sur l'interaction entre TiO_2/ZnO et des modèles phospholipidiques qui ressemblent à l'enveloppe du coronavirus et pourraient s'adsorber à la surface. Nous avons optimisé un modèle simplifié de phospholipide où les groupes méthyle remplacent les longues chaînes alkyle des acides gras. Nous avons étudié différents modes d'adsorption du phospholopide à la surface de TiO_2. La configuration optimisée la plus stable montre quatre atomes d'oxygène de coordination, deux du groupe phosphate (adsorbés sur deux centres Ti adjacents par une coordination bidentate pontée) et les deux autres du groupe

carboxylate, où l'interaction la plus importante est liée à l'oxygène adsorbé du groupe phosphate et apportant ainsi la plus grande contribution à la stabilisation du système. L'énergétique associée à la liaison de la molécule phospholipidique à la surface de TiO_2 donne des indications sur l'occurrence de ces processus. Nous avons dupliqué la surface de TiO_2 et en comparant les différences d'énergie (ΔE) des réactions d'adsorption nous avons trouvé que le système d'adsorption associé à une plus grande surface est favorisé par rapport à celui de plus petite surface présentant la même géométrie d'adsorption. Cette différence d'énergie peut s'expliquer par les interactions entre les molécules de phospholipides de différentes copies qui déstabilisent le système dans les modèles d'oxydes plus petits. Nous évitons ce genre d'interactions en répliquant la surface de manière à considérer le phospholipide comme une véritable molécule isolée qui se traduit par un système d'adsorption plus stabilisé. Nous avons encore optimisé la structure complète du phospholipide en ajoutant les longues chaînes alkyle que nous avons considérées comme un modèle pour décrire l'enveloppe du virus. Nous avons étudié les réactions des phospholipides fixant les sites d'adsorption les plus stables avec ou sans forces de van der Waals, qui peuvent être particulièrement importantes lorsque de si longues chaînes sont impliquées. Nous avons remarqué l'augmentation de la stabilité des réactions d'adsorption par des chaînes alkyles plus longues. De même, les résultats obtenus à partir de la prise en compte de ces forces sont bien plus favorisés que les systèmes n'incluant pas de telles interactions, considérant la même structure d'adsorption. Ceci indique la contribution importante de ces forces sur l'adsorption des phospholipides à la surface. Ces résultats préliminaires mettent en évidence que les molécules de phospholipides peuvent être fortement adsorbées à la surface de TiO_2, ce qui suggère que ce matériau, compte tenu de ses propriétés photocatalytiques bien connues, pourrait être un candidat important pour la purification de l'air des virus. Suivant la même stratégie appliquée au TiO_2, nous avons étudié l'adsorption du phospholipide sur la surface de ZnO pour étudier sa stabilité sur cette surface. La configuration optimisée la plus stable est obtenue en coordonnant deux atomes d'oxygène du groupe phosphate et deux du groupe carboxylate adsorbés sur deux centres Zn adjacents par une coordination bidentée pontée, en accord avec les résultats de TiO_2. L'énergétique associée aux réactions d'adsorption pour ZnO montre une tendance similaire à celle trouvée pour TiO_2, cependant ZnO montre une plus grande capacité à adsorber les phospholipides. ZnO est un meilleur candidat pour adsorber les phospholipides et pourrait donc être un bon matériau également pour dégrader le virus de l'enveloppe phospholipidique.

Riepilogo

Nella geochimica ambientale, si prevede che l'aumento della produzione e delle applicazioni di nanoparticelle di ZnO si tradurrà in un suo maggiore rilascio nell'ambiente. Nonostante la consapevolezza che le nanoparticelle sono sempre più utilizzate in diversi campi dell'attività umana, la quantificazione del loro rilascio nell'ambiente è piuttosto impegnativa a causa dei dati limitati sulla loro prevalenza attuale e prevista nei prodotti commerciali. Le difficoltà tecniche associate alla quantificazione dei livelli di nanoparticelle di ZnO nell'ambiente hanno portato alla necessità di prevedere le concentrazioni ambientali in base alla penetrazione nel mercato dei nanomateriali, all'uso noto dei prodotti e al destino/comportamento. Una volta rilasciate nell'ambiente, le nanoparticelle di ZnO possono mostrare comportamenti diversi. In questo lavoro, abbiamo concentrato il nostro studio teorico sulla valutazione dell'effetto di superficie sulla firma isotopica per identificare se le nanoparticelle di ZnO hanno una composizione isotopica di Zn diversa dai cristalli di ZnO sfusi in condizioni di equilibrio. La struttura in massa di ZnO, la superficie della lastra e la nanoparticella sono i tre tipi di modelli strutturali considerati per discutere l'effetto superficiale e le proprietà isotopiche delle nanoparticelle di ZnO. Le proprietà isotopiche sono determinate dalle frequenze vibrazionali attraverso la determinazione dei rapporti di funzione di partizione ridotti (fattori β). Abbiamo ottimizzato la struttura di massa ZnO e calcoliamo le frequenze vibrazionali su questa struttura al fine di determinare il fattore di frazionamento di equilibrio per Zn. Il valore del fattore β per la massa di ZnO in cui gli atomi

di Zn sono quattro volte coordinati con gli atomi di O è 3,96 ‰ a 273 K. La rigidità dei legami interatomici che controlla il fattore β è stata valutata dalla costante di forza interatomica (190 Ry/ bohr²). Abbiamo ulteriormente studiato le superfici $(1\,0\,\bar{1}\,0)$ e $(2\,\bar{1}\,\bar{1}\,0)$ utilizzando modelli periodici di lastre. Per entrambi i modelli, i fattori β Zn mostrano risultati molto simili a quelli della massa, tuttavia, gli atomi di Zn di superficie segnano fattori β più elevati. Questo frazionamento è spiegato dal cambiamento di coordinazione da quattro volte nella struttura di massa a tre volte in superficie. Questa sottocoordinazione degli atomi di Zn sulla superficie provoca l'accorciamento dei legami Zn-O e l'aumento dei fattori β. I fattori β aumentano proporzionalmente con la costante di forza interatomica. Questa relazione riflette la forte dipendenza del frazionamento isotopico con costanti di forza interatomiche. Le superfici delle lastre ZnO studiate $(1\,0\,\bar{1}\,0)$ e $(2\,\bar{1}\,\bar{1}\,0)$ sono state utilizzate per esplorare l'interazione e l'adsorbimento dell'acqua su queste superfici. Questo adsorbimento consente il coordinamento completo degli atomi di Zn di superficie e quindi il numero di coordinazione è 4 lungo tutti gli atomi di Zn delle lastre. L'adsorbimento dell'acqua rimuove il triplice effetto di coordinazione in superficie e quindi si traduce in una firma di fattori β simile lungo tutti gli atomi di Zn delle lastre studiate. Inoltre, ispezioniamo il nanocluster ZnO costituito dalla superficie polare (0001) in alto e in basso e la superficie apolare $(1\,0\,\bar{1}\,0)$ ai lati laterali. Abbiamo adsorbito molecole d'acqua sulla superficie (0001), come abbiamo fatto per le superfici delle lastre per saturare gli atomi superficiali sottocoordinati e allo stesso tempo per minimizzare il dipolo lungo l'asse c. I risultati delle nanoparticelle qui sono coerenti con quelli derivati dai calcoli effettuati sulla struttura di massa e sui modelli delle lastre, con piccole variazioni dovute al rilassamento strutturale più importante nel calcolo delle nanoparticelle. La correlazione tra fattori β e costanti di forza per questa nanoparticella è la stessa dei precedenti modelli bulk e slab. Questo segue la regola generale dei legami brevi che concentrano isotopi pesanti.

Nel campo dei beni culturali, l'ossido di zinco è un pigmento bianco tipico delle pitture che si degrada in olio formando saponi metallici; si tratta in genere di complessi di ioni zinco con acidi grassi a catena lunga che provengono dal processo di invecchiamento del mezzo legante l'olio. È stato ipotizzato che la degradazione di ZnO sia inizializzata dall'interazione del pigmento ZnO con le funzionalità carbossiliche formate dalle reazioni di autossidazione. Considerando l'incertezza che ancora esiste nel meccanismo di degradazione atomistica di ZnO e la sua importanza per la conservazione delle opere d'arte, è importante chiarire le diverse fasi del processo di degradazione di ZnO per aiutare i restauratori a lavorare. In

questo lavoro abbiamo studiato alcuni dei potenziali passaggi chiave del processo di degradazione reattiva. Sulla base dei dati sperimentali disponibili sulle possibili vie di degradazione, viene calcolata una sequenza di intermedi plausibili e vie di reazione per stimare la termodinamica della reazione ed evidenziare possibili meccanismi legati alla stabilità dei diversi prodotti di degradazione. Ci siamo inizialmente concentrati sull'interazione tra ZnO e diversi acidi carbossilici dell'olio che sono prodotti di degradazione comuni e potrebbero adsorbirsi sulla superficie di ZnO. Associamo questa fase di adsorbimento all'inizializzazione del percorso di degradazione e quindi abbiamo caratterizzato possibili intermedi e prodotti finali. Partendo dal pigmento ZnO costruiamo un cluster che ha già dimostrato un buon modello per descrivere le proprietà elettroniche ed ottiche di ZnO. Abbiamo mirato a indagare (i) l'interazione tra ZnO e acidi carbossilici e acetati, che sono plausibili frammenti reattivi della degradazione dell'olio, e (ii) la formazione dei prodotti di degradazione dello ZnO, i carbossilati di Zn. Abbiamo studiato l'adsorbimento dell'acido acetico/acetato sulla superficie di ZnO, nel mezzo a bassa polarità, che può essere considerato l'inizializzazione della via di reazione che porta alla formazione di sapone metallico. Abbiamo ottimizzato l'adsorbimento di AcH esplorando diverse modalità di adsorbimento per studiarne la stabilità corrispondente. La configurazione ottimizzata più stabile mostra l'acido acetico adsorbito su due centri Zn adiacenti da una configurazione bidentata a ponte trasferendo il protone a un ossigeno della superficie ZnO, quindi in modalità di adsorbimento dissociativo. La configurazione più stabile dell'acetato adsorbato è quella con i due acetati coordinati si uniscono su diverse coppie di Zn. Ci concentriamo sull'energetica associata al legame dell'acido acetico/acetato alla superficie di ZnO, che fornisce indicazioni sul verificarsi di questi processi. Le reazioni di adsorbimento sono esotermiche dimostrando che l'acido acetico e l'acetato chimico si adsorbono sulla superficie di ZnO e che questi sistemi di adsorbimento potrebbero essere plausibili intermedi delle vie di reazione globali della degradazione. Inoltre, confrontando il ΔE delle reazioni abbiamo riscontrato che i sistemi di adsorbimento associati all'acido acetico sono più favoriti rispetto a quelli adsorbenti all'acetato. Questa maggiore esotermia è il risultato tra l'energia della dissociazione del protone (passo debolmente endotermico) e quella dell'adsorbimento del protone (passo altamente esotermico) per l'adsorbimento dell'acido acetico. Abbiamo ulteriormente convalidato il nostro approccio a cluster ottimizzando le specie coinvolte della reazione di adsorbimento più favorita ottenuta, utilizzando un approccio a lastra periodica. I risultati ottenuti sono compatibili con quelli dell'approccio a cluster, confermando così l'adeguatezza del modello nello studio di questo tipo di percorso di reattività. Seguendo il

meccanismo di degradazione ipotizzato, gli ioni di zinco migrano da ZnO durante l'essiccazione della vernice e si legano ai gruppi carbossilato. Ci siamo concentrati su questa fase di degradazione, vale a dire la formazione di $Zn(AcO)_2$ dallo ione Zn rilasciato dalla superficie di ZnO e le due unità di acetato, che rappresentano una fase intermedia durante l'essiccazione dell'olio e si traduce nell'aspetto finale del sapone metallico. Partendo dagli stessi reagenti, cluster ZnO e acido acetico/acetato, i prodotti sono: (i) il cluster ZnO con una vacanza di Zn sulla superficie lasciandolo protonato indicando il trasferimento di protoni dall'acido acetico o deprotonato in combinazione con l'acetato , e (ii) lo Zn-dicarbossilato. Abbiamo ottimizzato i due cluster ZnO con una vacanza di Zn, esplorando diverse posizioni dello ione rilasciato e dei protoni sulla superficie per le reazioni con gli acidi, mentre non sono stati aggiunti protoni per le reazioni con l'acetato. Abbiamo scoperto che le reazioni che coinvolgono l'acido acetico sono esotermiche, tuttavia sono endotermiche per il caso dell'acetato. Questi valori endotermici sono sovrastimati a causa della trascuratezza del bilancio di carica sulla superficie di ZnO che invece dovrebbe essere almeno parzialmente presente nel sistema realistico. Possiamo concludere che le reazioni che coinvolgono l'acido acetico sono favorite rispetto a quelle con acetato. Confrontando le due vie di reazione studiate, abbiamo scoperto che l'adsorbimento di acido acetico/acetato sulla superficie di ZnO è termodinamicamente favorito rispetto al rilascio di ioni Zn dalla superficie per formare complessi Zn. Questi risultati sono coerenti con l'ipotesi che la via di reazione che porta alla formazione di saponi metallici sia iniziata dall'adsorbimento di acido carbossilico/carbossilato sulla superficie del cluster ZnO. Questo adsorbimento presenta un percorso dalla reazione globale che porta alla formazione di sapone metallico. Per valutare come la lunghezza della catena acida influenzi l'interazione acido-ZnO e la complessazione, consideriamo anche l'acido esanoico per effettuare un'analisi comparativa. Seguendo la stessa strategia applicata sopra, partiamo dall'acido esanoico/esanoato e dal cluster ZnO come reagenti. Ci concentriamo sulle reazioni che portano all'acido esanoico@ZnO e all'esanoato@ZnO più stabili in un mezzo a bassa polarità. L'energetica associata a queste reazioni mostra una tendenza simile trovata per acido acetico/acetato. Tuttavia, le energie di reazione con acido esanoico/esanoato sono calcolate maggiori di quelle analoghe che coinvolgono l'acido acetico. L'aumento dell'esotermia di questi passaggi reattivi con gli acidi esanoici è correlato all'aumento della capacità di donare elettroni della catena più lunga. Pertanto, potremmo concludere che la degradazione è favorita da acidi carbossilici a catena più lunga. L'acido acetico rimane comunque un buon modello per individuare le principali fasi reattive della formazione dei complessi di Zn. Secondo i sistemi ottimizzati più stabili

studiati nella parte precedente, abbiamo studiato le reazioni di formazione di complessi di esanoato Zn. Osserviamo che l'adsorbimento di acido esanoico/esanoato sulla superficie di ZnO è favorito rispetto al rilascio di ione Zn dalla superficie per formare complessi Zn in accordo con i risultati ottenuti per l'acido acetico. Queste due reazioni studiate rappresentano un modello semplificato dei passaggi chiave delle più complesse vie di degradazione dello ZnO.

Nella fotocatalisi, le reazioni possono avvenire utilizzando la luce e un semiconduttore: in questo meccanismo, viene generata una coppia elettrone-lacuna dall'esposizione di un materiale semiconduttore alla luce, quindi l'elettrone eccitato viene utilizzato per ridurre una specie accettore mentre la lacuna può contemporaneamente ossidare una specie donatrice. Le proprietà fotocatalitiche del TiO_2 lo rendono vicino a un fotocatalizzatore ideale. Mostra un'elevata energia a band gap ed è noto per rendere il processo di degradazione fotocatalitica poco costoso e facile sotto la luce solare. ZnO ha anche mostrato un immenso potenziale come fotocatalizzatori e mostra proprietà simili al TiO_2. Questo lavoro fornisce informazioni sugli effetti della fotocatalisi per degradare il coronavirus utilizzando semiconduttori di ossido di metallo TiO_2 e ZnO. In questo studio preliminare, ci siamo concentrati sull'interazione tra modelli TiO_2/ZnO e fosfolipidi che assemblano l'ambiente del coronavirus e potrebbero adsorbirsi in superficie. Abbiamo ottimizzato un modello semplificato di fosfolipidi in modo tale che i gruppi metilici sostituiscano le lunghe catene alchiliche degli acidi grassi. Abbiamo studiato diverse modalità di adsorbimento del fosfolopide sulla superficie di TiO_2. La configurazione ottimizzata più stabile mostra quattro atomi di ossigeno coordinanti, due del gruppo fosfato (adsorbito su due centri Ti adiacenti da una coordinazione bidentata a ponte) e gli altri due del gruppo carbossilato, dove l'interazione più importante è correlata all'ossigeno adsorbito di il gruppo fosfato e dando così il contributo maggiore per stabilizzare il sistema. L'energetica associata al legame della molecola fosfolipidica alla superficie del TiO_2 fornisce indicazioni sul verificarsi di questi processi. Duplichiamo la superficie di TiO_2 e confrontando il ΔE delle reazioni di adsorbimento abbiamo scoperto che il sistema di adsorbimento associato a una superficie più grande è più favorito rispetto a quello di una superficie più piccola che presenta la stessa geometria di adsorbimento. Questa differenza di energia può essere spiegata dalle interazioni tra le molecole di fosfolipidi di diverse copie che destabilizzano il sistema nei modelli di ossido più piccoli. Evitiamo questo tipo di interazioni replicando la superficie in modo da considerare il fosfolipide come una vera molecola isolata che si traduce in un sistema di adsorbimento più stabilizzato. Abbiamo

ulteriormente ottimizzato l'intera struttura del fosfolipide aggiungendo le lunghe catene alchiliche che abbiamo considerato come un modello per descrivere l'involucro del virus. Abbiamo studiato le reazioni del fosfolipide che attacca i siti di adsorbimento più stabili con o senza includere le forze di van der Waals, che possono essere particolarmente importanti quando sono coinvolte catene così lunghe. Abbiamo notato l'aumento della stabilità per le reazioni di adsorbimento da parte di catene alchiliche più lunghe. Inoltre, i risultati ottenuti dall'inclusione di queste forze sono molto più favoriti rispetto ai sistemi che non includono tali interazioni, considerando la stessa struttura di adsorbimento. Ciò indica l'importante contributo di queste forze sull'adsorbimento dei fosfolipidi in superficie. Questi risultati preliminari evidenziano che le molecole di fosfolipidi possono essere fortemente adsorbite sulla superficie di TiO_2, il che suggerisce che questo materiale, date le sue ben note proprietà fotocatalitiche, potrebbe essere un candidato importante per la purificazione dell'aria dai virus. Seguendo la stessa strategia applicata al TiO_2, abbiamo studiato l'adsorbimento del fosfolipide sulla superficie di ZnO per studiarne la stabilità su questa superficie. La configurazione ottimizzata più stabile si ottiene coordinando due atomi di ossigeno del gruppo fosfato e due del gruppo carbossilato adsorbiti su due centri Zn adiacenti mediante una coordinazione bidentata a ponte, in accordo con i risultati di TiO2. L'energetica associata alle reazioni di adsorbimento per ZnO mostra una tendenza simile trovata per TiO_2, tuttavia ZnO mostra una maggiore capacità di adsorbire fosfolipidi. ZnO è un candidato migliore per adsorbire fosfolipidi e quindi potrebbe essere un buon materiale anche per degradare il virus dell'involucro fosfolipidico.

Abstract

The present thesis studies metal oxides and their engagement in the different domains. We focused our work on environmental geochemistry, cultural heritage, and photocatalysis fields based on metal oxides interactions.

Environmental geochemistry. ZnO are very common systems present in various contexts and also model systems widely studied. ZnO nanoparticles are found in soil and water, it is therefore important to study the fate and behavior of this material in the environment, and isotopes are efficient tools for achieving this goal. Computer simulations can complement the direct materials analysis of these systems. In particular, we focused our theoretical study on the assessment of the surface effect on the isotopic signature. Do ZnO nanoparticles have different Zn isotope composition from bulk ZnO crystals in equilibrium conditions? In order to address this question, we performed structure and frequency calculations based on DFT on various structural models. Isotopic properties are then determined from the vibrational frequencies. Three kinds of structural models were considered: ZnO bulk structure, the slab surfaces $(1\ 0\ \bar{1}\ 0)$ and $(2\ \bar{1}\ \bar{1}\ 0)$, and a model nanoparticle. The results obtained allow us to discuss the surface effect and the isotopic properties of ZnO nanoparticles.

Cultural heritage. Advanced computational modelling strategies have been applied to cultural heritage to assist the characterization of painting materials and to understand their intrinsic and external degradation processes. The degradation of the widely employed zinc oxide (ZnO) - a white pigment mostly used in oil paints- leads to the formation of metal soaps, complexes of Zn ions and long chain fatty acids coming from the degradation of the

oil binder. Being a serious problem affecting the appearance and the structural integrity of many oil paintings, it is relevant to characterize the structure of these complexes and to understand the reaction pathways associated to this degradation process. Density functional theory (DFT) calculations have been performed to investigate the adsorption of the acetate and acetic acid on relatively large ZnO clusters and the formation of Zn-acetate complexes. Carboxylic acids with longer alkyl chains have then been investigated as more realistic models of the fatty acids present in the oil medium. In addition DFT calculations using a periodic ZnO slab have been performed in order to compare the obtained results at different levels of theory. Optimization calculations as well as formation energies of the ZnO@carboxylate coupled systems and the thermodynamics leading to possible degradation products have been computed. Our results highlight the potential of DFT calculations for a better understanding of oil paint degradation with the aim to contribute to the development of strengthening and conservation strategies of paintings.

In photocatalysis, reactions can take place using light and a semiconductor: in this mechanism, an electron-hole pair is generated upon exposure of a semiconductor material to light, then the excited electron is used to reduce an acceptor species while the hole can simultaneously oxidize a donor species. The photocatalytic properties of TiO_2 make it an ideal photocatalyst. It displays high bandgap energy and is known to make photocatalytic degradation process inexpensive and easy under sunlight. ZnO has also shown immense potential as photocatalysts and exhibits similar properties to TiO_2. This work provides insight into the effects of photocatalysis to degrade coronavirus using TiO_2 and ZnO metal oxide semiconductors. In this preliminary study, we focused on the interaction between TiO_2 / ZnO and phospholipid models which assemble the environment of the coronavirus and could adsorb on the surface, employing different models and methods to calculate the energy associated to the adsorption of phospholipid at the metal oxide surface.

Table of Contents

Introduction (en Français)

La chimie quantique est devenue un outil important et puissant pour étudier un grand nombre de phénomènes chimiques et physiques. De nos jours, la croissance rapide de la puissance de calcul ainsi que le développement de méthodologies adéquates spécifiquement adaptées à l'approche de systèmes de grande échelle, permettent aux chercheurs de traiter des problèmes de taille et de complexité croissantes. Dans cette thèse est présentée une série de simulations de mécanique quantique focalisées sur les oxydes métalliques dans trois domaines différents; i) la géochimie environnementale; ii) la restauration et la conservation du patrimoine culturel; et iii) la dégradation photocatalytique. Ces domaines apparemment éloignés de la chimie ont en commun la modélisation des oxydes métalliques, nécessitant des méthodes de calcul spécifiquement adaptées pour être opérationnelles de manière intégrée. D'un point de vue général, nos investigations théoriques soulignent le rôle crucial de la modélisation numérique dans la recherche chimique moderne, offrant la possibilité d'effectuer des simulations atomistiques prédictives, dans lesquelles les propriétés d'un système donné sont simulées avant même la synthèse et la caractérisation en laboratoire des matériaux.

Les oxydes métalliques sont des matériaux bien connus pour diverses applications en raison de leur rapport surface/volume élevé, de leur réactivité élevée et de leur bonne distribution granulométrique. Ces propriétés présentent un facteur clé pour une interaction efficace des oxydes métalliques avec les molécules cibles. Au cours des dernières décennies, l'intérêt pour les interactions chimiques se produisant au niveau des surfaces d'oxydes métalliques a considérablement augmenté en raison de leur importance dans divers domaines, notamment la science des matériaux, la chimie et la géochimie. Actuellement, la taille de nombreux dispositifs et matériaux technologiques diminue rapidement vers l'échelle nanométrique. À mesure que nous approchons de la limite « nano », la densité des interfaces augmente considérablement de sorte que l'effet des interactions métal-oxyde devient de plus en plus important.

Les oxydes métalliques dans l'environnement

Les oxydes métalliques jouent un rôle clé dans la remédiation de l'environnement et la détection des polluants et sont également stratégiques dans plusieurs autres applications, notamment la production, la conversion et le stockage d'énergie. Les oxydes métalliques présentent une grande variété de propriétés fonctionnelles, fortement dépendantes de leur structure cristalline, morphologie, composition, défauts intrinsèques, dopage, etc., qui déterminent leurs propriétés optiques, électriques, chimiques et catalytiques. Les méthodes de synthèse chimique et physique et de croissance régissent fortement les caractéristiques morpho-structurelles et donc les propriétés physico-chimiques des oxydes métalliques.[1,2] La bande interdite et la structure électronique des oxydes peuvent être contrôlées et adaptées par la taille et la dimension, ce qui procure aux matériaux à base d'oxydes métalliques des possibilités multifonctionnelles. La modulation de la bande interdite et des propriétés d'adsorption de surface est essentielle pour une application comme photocatalyseurs hétérogènes.

L'augmentation de la production et des applications des nanoparticules d'oxydes métalliques entraîne une augmentation de leur libération dans l'environnement. Les écosystèmes aquatiques sont les principaux récepteurs, principalement du fait des eaux usées industrielles et domestiques.[3] Le rejet dans l'environnement des nanoparticules d'oxydes métalliques peut intervenir dès leur production, fabrication de produits contenant des nanoparticules, lors de leur utilisation et de la fin de vie de ces produits. Bien que l'on sache que les nanoparticules sont de plus en plus utilisées dans différents domaines de l'activité humaine, la quantification de leur libération dans l'environnement, à un moment donné, est assez difficile en raison des données limitées sur leur prévalence actuelle et prévue dans les produits commerciaux.[4,5] Les difficultés techniques associées à la quantification des niveaux de nanoparticules d'oxydes métalliques dans l'environnement ont conduit à la nécessité de prédire les concentrations environnementales en fonction de la pénétration du marché des nanomatériaux, de leur utilisation ainsi que leur comportement biogéochimique et leur devenir. Une fois rejetées dans l'environnement, les nanoparticules d'oxydes métalliques peuvent afficher différents comportements (dissolution, stabilisation, transformation, croissance, …) devant être étudiés.

Relation entre patrimoine culturel et oxydes métalliques

Le lien entre l'art et la science a toujours été fort puisque les artistes ont toujours eu une connaissance approfondie des propriétés des matériaux employés et ont souvent expérimenté des recettes mélangeant des ingrédients naturels pour obtenir de nouvelles nuances de couleurs de matériaux. Néanmoins, l'art et la chimie ont souvent été considérés comme très éloignés et ce n'est que récemment que la chimie a acquis un rôle conscient dans l'art.

La connaissance des matériaux constitutifs et des techniques utilisées dans les œuvres d'art est un élément crucial pour les historiens de l'art, les restaurateurs et les conservateurs des musées. En particulier, l'apport des sciences chimiques et physiques sur la caractérisation des matériaux peut être très important pour démêler la riche information contenue dans une œuvre d'art. Ces informations peuvent révéler des aspects d'importance historique et artistique et peuvent également être utilisées à des fins de restauration et de conservation. Le développement de méthodes spectroscopiques non invasives et la portabilité des instruments actuels ont fait de la chimie physique et analytique une clé de voûte de l'étude du patrimoine culturel, et le nombre d'articles publiés impliquant les deux domaines a augmenté de façon exponentielle au cours des dernières décennies.

Le rôle de la chimie dans le patrimoine culturel va de l'étude des matériaux et des techniques à la compréhension de l'origine et des mécanismes de détérioration des œuvres d'art, en passant par le développement de nouvelles méthodologies analytiques et la conception de nouveaux équipements de surveillance.

Parallèlement aux développements expérimentaux en instrumentation spectroscopique, la chimie computationnelle a acquis ces dernières années une grande importance dans des domaines aussi variés que l'industrie pharmaceutique, le développement de matériaux fonctionnels ou les énergies renouvelables. De plus, la précision atteinte dans la modélisation des propriétés de systèmes complexes, grâce au développement d'algorithmes plus efficaces et d'ordinateurs performants, en fait un outil prédictif précieux. Le rôle de la chimie computationnelle va de la compréhension et rationalisation des données expérimentales à la modélisation de nouveaux matériaux.

Bien que l'expérience de telles collaborations multidisciplinaires souligne la grande contribution que la chimie computationnelle peut apporter, ce n'est que récemment qu'elle a été appliquée au domaine du patrimoine culturel. Les calculs peuvent cependant fournir une

quantité importante d'informations nouvelles complétant les données expérimentales et donnant une compréhension plus profonde des matériaux constitutifs d'une œuvre d'art.

Les pigments d'oxydes métalliques sont utilisés depuis l'Antiquité en raison de leurs couleurs vives et de leur pouvoir couvrant élevé. Avec le liant à l'huile et une variété d'additifs, ces pigments constituent les principaux composants des peintures à l'huile. Les oxydes métalliques ont été considérés par les historiens de l'art comme les premiers pigments artificiels et ont été largement utilisés dans les œuvres d'art. Il est donc important d'étudier les interactions des oxydes métalliques dans ce domaine.

Les oxydes m étalliques comme catalyseurs dans la dégradation photocatalytique

La photocatalyse est une science qui utilise un catalyseur pour accélérer les réactions chimiques nécessitant de la lumière. Un photocatalyseur est défini comme un matériau capable d'absorber la lumière, de produire des paires électron-trou permettant des transformations chimiques des composés participant à la réaction et enfin de régénérer sa composition chimique.[6-11]

Les caractéristiques importantes du système photocatalytique sont la bande interdite souhaitée, la morphologie appropriée, la surface élevée, la stabilité et la réutilisabilité.[8-11] Les oxydes métalliques tels que les oxydes de zinc, de titane, de vanadium, de chrome, d'étain et de cérium possédant ces caractéristiques suivent des processus photocatalytiques primaires tels que l'absorption de la lumière, qui induit un processus de séparation de charge avec la formation de trous positifs capables d'oxyder les substrats organiques.[9-11] Dans ce processus, un oxyde métallique est activé avec de la lumière UV, de la lumière visible ou une combinaison des deux, et les électrons photoexcités sont promus de la bande de valence à la bande de conduction, formant une paire électron/trou (e-/h+). Le couple photogénéré (e-/h+) est capable de réduire et/ou d'oxyder un composé adsorbé sur la surface du photocatalyseur. L'activité photocatalytique de l'oxyde métallique provient de deux sources : (i) génération de radicaux •OH par oxydation des anions OH^-, (ii) génération de radicaux O_2^- par réduction de O_2. Les radicaux et les anions peuvent réagir avec les polluants pour les dégrader ou les transformer autrement en sous-produits moins nocifs.[10,11]

Il existe de nombreux catalyseurs rapportés dans la littérature pour ce processus passionnant. Parmi ces oxydes métalliques, TiO_2, ZnO, SnO_2 et CeO_2 qui sont abondants dans la nature, ont également été largement utilisés comme photocatalyseurs, notamment comme photocatalyseur hétérogène depuis plusieurs décennies.[10-12] Ceci est lié à leur biocompatibilité, stabilité exceptionnelle dans un variété de conditions et capacité à générer des porteurs de charge lorsqu'ils sont stimulés avec la quantité requise d'énergie lumineuse. La combinaison favorable de la structure électronique, des propriétés d'absorption de la lumière, des caractéristiques de transport de charge et des durées de vie excitées des oxydes métalliques a rendu possible leur application en tant que photocatalyseur.[7-11,13] La photocatalyse hétérogène utilisant des oxydes métalliques tels que TiO_2, ZnO, SnO_2 et CeO_2 a prouvé son efficacité à dégrader un large éventail de polluants distincts en composés biodégradables et finalement à les minéraliser en dioxyde de carbone et en eau inoffensifs.[14-23]

Des recherches récentes ont également montré que les oxydes métalliques peuvent être utilisés comme photocatalyseur pour décomposer les composés organiques toxiques, pour une application photovoltaïque, pour empêcher la formation de buée sur le verre et même pour diviser l'eau en hydrogène et oxygène.[7-11] Par conséquent, ils sont d'une grande importance technologique dans les domaines de l'environnement, assainissement, stockage, production d'hydrogène et industries électroniques.[8-11] Les applications de ce procédé photocatalytique sont principalement nécessaires pour la purification des eaux usées, en éliminant les bactéries et autres polluants, car cela peut rendre l'eau réutilisable.

Lorsque la réaction d'oxydation photocatalytique est réalisée en présence d'O_2, le catalyseur joue non seulement un rôle de piégeage des électrons photogénérés mais produit également des espèces actives d'oxygène. Outre le photocatalyseur activé par la lumière UV, il a été récemment signalé que les oxydes métalliques défectueux pouvaient également réagir à la lumière visible, un processus appelé photocatalyse induite par la lumière visible largement utilisé pour l'assainissement de l'environnement.[16-18,22,23] Il s'agit d'une nouvelle étape importante dans le domaine de la photocatalyse.

Les propriétés physicochimiques des oxydes métalliques sont cruciales pour les performances photocatalytiques vertueuses, qui dépendent généralement de la taille, de la forme, de la morphologie et de la composition.[7-10,19,21] La procédure de synthèse utilisée peut contrôler la taille, la forme et la morphologie des matériaux préparés, ce qui peut contribuer au

développement de certaines propriétés des matériaux photoactifs. Cela peut faciliter la formation de poudres ou de films minces avec les caractéristiques requises qui améliorent les performances du catalyseur.[11,19,21,24-26] La source et le type de lumière utilisée peuvent également affecter les performances du matériau comme photocatalyseur.[13-15]

Par conséquent, la recherche de nouveaux photocatalyseurs ayant les caractéristiques souhaitées pour induire l'oxydation de substrats organiques ou de polluants sous irradiation de lumière visible est à encourager. Les oxydes métalliques doivent être écologiquement respectueux et la préparation par des voies peu coûteuses doit être la principale attention.

Organisation de la thèse

L'ensemble de la thèse est divisé en six chapitres qui sont organisés comme suit : Le chapitre **Chapitre 1** fournit une introduction générale sur les oxydes métalliques et leur implication dans les différents domaines. Nous avons concentré notre étude sur les domaines du patrimoine culturel, de la géochimie environnementale et de la dégradation photocatalytique.

Le **chapitre 2** décrit les méthodes théoriques utilisées dans ce travail de thèse. Ces méthodes sont basées sur des théories de chimie quantique centrées sur la résolution de l'équation de Schrödinger. Différentes approximations sont décrites. Puis, une procédure générale de modélisation de l'interaction avec les surfaces d'oxyde métallique est illustrée.

Le **chapitre 3** traite des outils isotopiques pour étudier le comportement des nanoparticules de ZnO dans l'environnement. Nous avons concentré notre étude théorique sur l'évaluation de l'effet de surface sur la signature isotopique afin d'identifier si les nanoparticules de ZnO ont une composition isotopique de Zn différente de celle des cristaux plus massifs de ZnO conditions d'équilibre thermodynamique. La structure cristalline de ZnO, les surfaces et les nanoparticules sont les trois types de modèles structuraux que nous avons considérés.

Le **chapitre 4** présente l'utilisation de stratégies de modélisation nulérique pour le patrimoine culturel afin d'aider à la caractérisation des matériaux de peinture. La dégradation de l'oxyde de zinc - un pigment blanc principalement utilisé dans les peintures à l'huile - conduit à la formation de complexes de savons métalliques affectant l'apparence et l'intégrité structurelle de nombreuses peintures. Ainsi, il est pertinent de caractériser la structure de ces complexes et de comprendre les voies réactionnelles associées à ce processus de dégradation.

Le **chapitre 5** rapporte une étude préliminaire pour la photocatalyse des oxydes métalliques et leur capacité à dégrader un virus à enveloppe phospholipidique. Nous nous sommes concentrés sur l'adsorption du phospholipide à la surface d'oxydes métalliques en utilisant différents modèles.

Le **chapitre 6** résume les résultats principaux obtenus dans les différents domaines étudiés et donne également des orientations pour les travaux futurs.

Chapter 1

Introduction

Quantum Chemistry has become an important and powerful tool to investigate a great deal of chemical and physical phenomena. Nowadays, the rapid growth of computational power along with the corresponding development of adequate methodologies specifically tailored to approach large scale systems, allows researchers in the field to treat problems of increasing size and complexity. In this thesis is presented a series of quantum mechanical computer simulations focused metal oxides in three different fields: i) environmental geochemistry; ii) cultural heritage restoration and conservation; and iii) photocatalytic degradation. These fields apparently distant fields of chemistry share the common background of being representative of the modelling of metal oxide, requiring specifically tailored computational methods to be operative in an integrated fashion. The overall picture of our theoretical investigations underlines a crucial role of computational modelling in modern chemical research, casting the possibility of performing predictive modelling simulations, in which the properties of a given system are simulated even before the materials laboratory synthesis and characterization.

Metal oxides are well-known materials for various applications due to their high surface area-to-volume ratio, high reactivity, and good size distribution. These properties present a key factor for effective interaction of metal oxides with target molecules. During the past decades, interest in chemical interactions occurring at metal oxide surfaces has increased significantly because of their importance in a variety of fields, including materials science, chemical applications and geochemistry. Presently, the sizes of many devices and technological materials are rapidly decreasing to the nanoregime. As we approach the nano limit, the density of interfaces increases substantially such that the effect of metal–oxide interactions becomes more and more significant.

1.1 Metal oxides applications in the environment

Metal oxides play a key role in environmental remediation and pollutant sensing and are strategic also in several other applications including energy production, conversion and storage. Metal oxides exhibit a great variety of functional properties, strongly depending on their crystal structure, morphology, composition, intrinsic defects, doping, etc., which determine their optical, electrical, chemical and catalytic properties. Growth methods and process parameters strongly govern the morpho-structural characteristics and therefore the physico-chemical properties of metal oxides.[1,2] The band gap and electronic structure of oxides can be controlled and tailored by the size and dimension and this is the key to multifunctional possibilities presented by metal oxide-based materials. Modulating the bandgap and surface adsorption properties is essential for application in heterogeneous photocatalysts. The structural diversity of metal oxides is provided by both chemical and physical methods of synthesis, and by the process parameters.

The increase in production and applications of metal oxide nanoparticles results in its increased release into the environment. The aquatic ecosystems will probably be the main recipients, mainly as a result of industrial and domestic wastewaters.[3] Metal oxide nanoparticles environmental release may occur as early as their production, production of products containing nanoparticles, during their use and end of life of those products. Despite the knowledge that nanoparticles are increasingly being used in different fields of human activity, the quantification of their release in the environment, at any given time, is quite challenging due to the limited data on their current and expected prevalence in commercial products.[4,5] The technical difficulties associated with quantification of metal oxide nanoparticles levels in the environment led to the need to predict environmental concentrations based on market penetration of nanomaterials, known usage of the products as well as fate and behaviour. Once released into the environment, metal oxide nanoparticles may display different behaviours that should be investigated significantly.

1.2 Cultural heritage relation with metal oxides

The link between art and science has always been strong since artists have always had a deep knowledge of the employed materials properties and had often experimented with recipes that mixed natural ingredients to obtain new material colours nuances. Nevertheless, art and

chemistry have been often considered very distant and only recently chemistry has achieved a conscious role in art.

The knowledge of the constitutive materials and of the techniques used in artworks is a crucial element for art historians, restorers and museum carers. In particular, the contribution of chemical and physical sciences on the characterization of the materials can be very important in unravelling the rich information enclosed in a work of art. This information may reveal aspects of historical and artistic significance, and can be also used for restoration and conservation purposes. The development of non-invasive spectroscopic methods and the portability of the current instruments have made of physical and analytical chemistry a keystone for cultural heritage, and the number of papers published involving both fields have increased exponentially in the last decades.

The role of chemistry in cultural heritage goes from the study of the materials and techniques to the comprehension of the origin and mechanisms of artwork deterioration, passing from the development of new analytical methodologies and the design of new monitoring equipment.

In parallel with the experimental developments in the spectroscopic instrumentation, computational chemistry has gained in the last years a great consideration in a variety of fields as pharmaceutical industry, development of functional materials or renewable energy. Moreover, the accuracy reached in simulating the properties of complex extended systems, thanks to the development of more efficient algorithms and high performance computers, makes it a valuable predictive tool. The role of computational chemistry goes from the comprehension and rationalization of experimental data to the modelling of new materials.

Although the experience of such multidisciplinary collaborations points out the great contribution that computational chemistry can give, only recently it has been applied to the cultural heritage field. Calculations can provide, however, an important amount of new information complementing experimental data and giving a deeper comprehension of the constituting materials of an artwork.

Metal oxide pigments have been used since antiquity due to their bright colors and high covering power. Together with oil binder and a variety of additives, these pigments constitute the main components of oil paints. Metal oxides have been considered by art historians to be

the earliest artificial pigments and have been widely used in artwork. Thus it is important to study of metal oxide interactions in this area.

1.3 Metal oxides as catalysts in photcatalytic degradation

Photocatalysis is a science of employing catalyst that is utilized for speeding up chemical reactions that requires light. A photocatalyst is defined as a material that is capable of absorbing light, producing electron–hole pairs that enable chemical transformations of the reaction participants and regenerate its chemical composition.[6-11]

The significant features of the photocatalytic system are the desired band gap, suitable morphology, high surface area, stability and reusability.[8-11] Metal oxides such as oxides of zinc, titanium, vanadium, chromium, tin, and cerium having these characteristics follow similar primary photocatalytic processes such as light absorption, which induces a charge separation process with the formation of positive holes that are able to oxidize organic substrates.[9-11] In this process, a metal oxide is activated with either UV light, visible light or a combination of both, and photoexcited electrons are promoted from the valence band to the conduction band, forming an electron/hole pair (e-/h+). The photogenerated pair (e-/h+) is able to reduce and/or oxidize a compound adsorbed on the photocatalyst surface. The photocatalytic activity of metal oxide comes from two sources: (i) generation of ·OH radicals by oxidation of OH^- anions, (ii) generation of O_2^- radicals by reduction of O_2. Both the radicals and anions can react with pollutants to degrade or otherwise transform them to lesser harmful by-products.[10,11]

There are many catalysts reported in the literature for this exciting process. Among these metal oxides (TiO_2, ZnO, SnO_2 and CeO_2), which are abundant in nature, have also been extensively used as photocatalysts, particularly as heterogeneous photocatalyst since several decades.[10-12] This is because of their biocompatibility, exceptional stability in a variety of conditions and capability to generate charge carriers when stimulated with required amount of light energy. The favourable combination of electronic structure, light absorption properties, charge transport characteristics and excited lifetimes of metal oxides has made it possible for their application as photocatalyst.[7-11,13] Heterogeneous photocatalysis employing metal oxides such as TiO_2, ZnO, SnO_2 and CeO_2 has proved its efficiency in degrading a wide range of distinct pollutants into biodegradable compounds and eventually mineralizing them to harmless carbon dioxide and water.[14-23]

Recent research has also shown that metal oxides can be used as a photocatalyst to decompose toxic organic compounds, photovoltaics, prevent fogging of glass and even split water into hydrogen and oxygen.[7-11] Hence, they are of great technological importance in areas of environmental remediation, storage, hydrogen production and electronic industries.[8-11] The applications of such photocatalytic process are mostly needed for the purification of waste water, by removal of bacteria and other pollutants, as this can render water reusable.

The properties of metal oxides make them effective photocatalysts for degradation of environment pollutants. When the photocatalytic oxidation reaction is carried out in the presence of O2, the catalyst not only plays a role in scavenging the photogenerated electrons but also produces active oxygen species. Apart from the UV-light activated photocatalyst, it was recently reported that the defected metal oxides could also respond to visible light, a process which is termed as visible light-induced photocatalysis widely employed for environmental remediation.[16-18,22,23] This is another milestone in the field of photocatalysis.

The physicochemical properties of the metal oxides are crucial for the virtuous photocatalytic performance, which are typically size, shape, morphology, and composition dependent.[7-10,19,21] The synthetic procedure employed can control the size, shape and morphology of the materials prepared, which can contribute towards the development of certain properties of the photoactive materials. This can facilitate the formation of powders or thin films with the required characteristics that improve the performance of the catalyst.[11,19,21,24-26] It is also the source and type of the light used that can affect the performance of the material as a photocatalyst.[13-15]

Hence, the search for new photocatalysts having desired characteristics to induce the oxidation of organic substrates or pollutants under visible light irradiation is encouraging. The metal oxides should be ecologically affable and preparation via inexpensive routes should be the main attention.

1.4 Thesis organization

The whole thesis is divided into six chapters which are organized as follows: The present chapter (**Chapter 1**) provides a general introduction about metal oxides and their engagement in the different domains. We focused our study on the cultural heritage, environmental geochemistry and photocatalytic degradation fields based on metal oxides interactions.

Chapter 2 describes the theoretical background methods employed in this thesis work. The computational methods used here are based on quantum chemical theories striving to solve the famous Schrodinger equation. Different approximations techniques are outlined in this Chapter. Then, a general procedure for modeling the interaction for metal oxide surfaces is illustrated.

Chapter 3 deals with isotopic tools to study the behaviour of ZnO nanoparticles in the environment. We focused our theoretical study on the assessment of the surface effect on the isotopic signature to identify if ZnO nanoparticles have different Zn isotope composition from bulk ZnO crystals in equilibrium conditions. ZnO bulk structure, slab surface, and nanoparticle are the three kinds of structural models which are considered to discuss the surface effect and the isotopic properties of ZnO nanoparticles.

Chapter 4 presents the employment of advanced computational modelling strategies to cultural heritage to assist the characterization of painting materials. The degradation of zinc oxide - a white pigment mostly used in oil paints- leads to the formation of metal soaps complexes affecting the appearance and the structural integrity of many oil paintings. Thus, it is relevant to characterize the structure of these complexes and to understand the reaction pathways associated to this degradation process.

Chapter 5 reports a preliminary study for the photocatalysis of metal oxides and their ability to degrade a virus from its phospholipid envelop, which is supposed to be susceptible of degradation by the investigated metal oxides. We focused on the adsoption of the phospholipid on top of the considered metal oxide surface by employing different models.

Chapter 6 summarizes the obtained results from the metal oxide applications in the different studied domains and also gives future directions for further work.

References

[1] M. L. Grilli, Metal Oxides, Metals, **2020**, 10, 820.

[2] D. Nunes, A. Pimentel, L. Santos, P. Barquinha, L. Pereira, E. Fortunato, R. Martins, Structural, optical, and electronic properties of metal oxide nanostructures, Met. Oxide Nanostruct., **2019**, 59–102.

[3] G. Bystrzejewska-Piotrowska, J. Golimowski, P. L. Urban, Nanoparticles: their potential toxicity, waste and environmental management, Waste Management, **2009**, 29, 2587– 2595.

[4] G. E. Batley, J. K. Kirby, M. J. McLaughlin, Fate and risks of nanomaterials in aquatic and terrestrial environments, Accounts of Chemical Research, **2013**, 46, 854–862.

[5] M. A. Maurer-Jones, I. L. Gunsolus, C. J. Murphy, C. L. Haynes, Toxicity of engineered nanoparticles in the environment, Analytical Chemistry, **2013**, 85, 3036–3049.

[1] S. H. S. Chan, T.Y. Wu, J. C. Juan, C. Y. The, Recent developments of metal oxide semiconductors as photocatalysts in advanced oxidation processes (AOPs) for treatment of dye waste-water, J. Chem. Technol. Biotechnol., **2011**, 86, 1130-1158.

[2] A. B. Djurišić, Y. H. Leung, A. M. C. Ng, Strategies for improving the efficiency of semiconductor metal oxide photocatalysis, Mater. Horiz., **2014**, 1, 400-410.

[3] E. Pelizzetti, C. Minero, Metal oxides as photocatalysts for environmental detoxification, Comments Inorg. Chem., **1994**, 15, 297-337

[4] T. Hisatomi, J. Kubota, K. Domen, Recent advances in semiconductors for photocatalytic and photoelectrochemical water splitting, Chem. Soc. Rev., **2014**, 43, 7520-7535.

[5] M. R. Hoffmann, S. T. Martin, W. Choi, D.W. Bahnemann, Environmental applications of semiconductor photocatalysis, Chem. Rev., **1995**, 95, 69-96

[6] A. Hernández-Ramírez, I. Medina-Ramírez, Photocatalytic Semiconductors, Springer, **2015**, ISBN 978-3-319-10998-5.

[7] A. Fujishima, K. Honda, Electrochemical photolysis of water at a semiconductor electrode, Nature, 1972, 238, 37-38.

[8] H. Wang, L. Zhang, Z. Chen, J. Hu, S. Li, Z. Wang, J. Liu, X. Wang, Semiconductor heterojunction photocatalysts: design, construction, and photocatalytic performances, Chem. Soc. Rev., **2014**, 43, 5234-5244.

[9] H. Chen, C.E. Nanayakkara, V.H. Grassian, Titanium dioxide photocatalysis in atmospheric chemistry, Chem. Rev., **2012**, 112, 5919-5948.

[10] M. Pelaez, N. T. Nolan, S. C. Pillai, M. K. Seery, P. Falaras, A. G. Kontos, P. S. M. Dunlop, J. W. J. Hamilton, J. A. Byrne, K. O'Sheaf, M. H. Entezari, D.D. Dionysiou, A review on the visible light active titanium dioxide photocatalysts for environmental applications, Appl. Catal. B, **2012**, 125, 331-349.

[11] S. Kalathil, M. M. Khan, S. A. Ansari, J. Lee, M. H. Cho, Band gap narrowing of titanium dioxide (TiO2) nanocrystals by electrochemically active biofilm and their visible light activity, Nanoscale, **2013**, 5, 6323-6326.

[12] M. M. Khan, S. A. Ansari, D. Pradhan, M. O. Ansari, D. H. Han, J. Lee, M. H. Cho, Band gap engineered TiO2 nanoparticles for visible light induced photoelectrochemical and photocatalytic studies, J. Mater. Chem. A, **2014**, 2, 637-644.

[13] S. A. Ansari, M. M. Khan, S. Kalathil, A. Nisar, J. Lee, M. H. Cho, Oxygen vacancy induced band gap narrowing of ZnO nanostructure by electrochemically active biofilm, Nanoscale, **2013**, 5, 9238-9246.

[14] H. Wang, A. L. Rogach, Hierarchical SnO2 nanostructures: recent advances in design, synthesis, and applications, Chem. Mater., **2014**, 26, 123-133.

[15] S. A. Ansari, M. Mansoob Khan, M. O. Ansari, J. Lee, M. H. Cho, Highly photoactive SnO2 nanostructures engineered by electrochemically active biofilm, New J. Chem., **2014**, 38, 2462-2469.

[16] C. Sun, H. Liab, L. Chen, Nanostructured ceria-based materials: synthesis, properties, and applications, Energy Environ. Sci., **2012**, 5, 8475-8505

[17] M. M. Khan, S. A. Ansari, D. Pradhan, D. H. Han, J. Lee, M. H. Cho, Defect-induced band gap narrowed CeO2 nanostructures for visible light activities, Ind. Eng. Chem. Res., **2014**, 53, 9754-9763.

[18] S.A. Ansari, M. M. Khan, M. O. Ansari, J. Lee, M. H. Cho, Band gap engineering of CeO2 nanostructure by electrochemically active biofilm for visible light applications, RSC Adv., **2014**, 4, 16782-16791.

[19] J. Yu, J. Low, W. Xiao, P. Zhou, M. Jaroniec, Enhanced photocatalytic CO_2-reduction activity of anatase TiO2 by coexposed {0 0 1} and {1 0 1} facets, J. Am. Chem. Soc., **2014**, 136, 8839-8842.

[20] P. Zhou, J. Yu, M. Jaroniec, All-solid-state Z-scheme photocatalytic systems, Adv. Mater., **2014**, 26, 4920-4935.

[21] B. Wang, G. Zhang, X. Leng, Z. Sun, S. Zheng, Characterization and improved solar light activity of vanadium doped TiO2/diatomite hybrid catalysts, J. Hazard. Mater., **2015**, 285, 212-220.

Chapter 2

Theoretical Background

Properties and energies of molecules can be analysed quantum mechanically by employing different methods. In this chapter the basis of the methods used in this thesis will be introduced. First, traditional ab initio methods, Hatree-Fock (HF) and subsequent post Hartree-Fock methods (post-HF), based on the solution of the Schrödinger equation by the application of several approximations are briefly described. In an alternative approach, the molecular properties are determined through the electronic density instead of the wavefunction. The methodologies employing such approach namely the density functional theory (DFT) which allows accurately describing the ground- stating properties is presented in this chapter. Finally, the plane-wave approach where the traditional localized basis set are replaced by plane waves basis set and pseudopotentials, allowing to extend calculations to the cases of extended bulk systems.

2.1 Ab initio Methods

2.1.1 The Schrödinger equation

The stationary properties of a many body system are determined by the solution of the time independent Schrödinger equation:[1]

$$\hat{H}\Psi = E\Psi \tag{2.1}$$

where E is the energy of the system and Ψ represents its wavefunction. The wavefunction includes all the information that can be obtained from the system and is such that $|\Psi|^2$ corresponds to the probability distribution in the space defined by the spatial and the spin coordinates. The Hamiltonian Ĥ, which stands for the energy operator, is composed by a kinetic and a potential part:

$$\hat{H}_{mol} = \hat{T}_{el} + \hat{V}_{el-el} + \hat{T}_{nuc} + \hat{V}_{nuc-nun} + \hat{V}_{nuc-el} \quad (2.2)$$

where, for a system of N electrons and M nuclei, in atomic units (a.u.), the single terms for the kinetic energy of the electrons and nuclei can be written as:

$$\hat{T}_{el} = -\frac{1}{2}\sum_{i=1}^{N} \nabla_i^2 \quad ; \quad \hat{T}_{nuc} = -\frac{1}{2}\sum_{\alpha}^{M} \frac{1}{2M\alpha} \nabla_i^2 \quad (2.3)$$

and the interaction between particles via the Coulomb forces result in three potential terms, electron-electron, nucleus-nucleus and electron-nucleus interactions, that can be written as:

$$\hat{V}_{el-el} = \sum_{i=1}^{N}\sum_{j>i}^{N} \frac{1}{r_{ij}} \quad ; \quad \hat{V}_{nuc-nuc} = \sum_{\alpha=1}^{M}\sum_{\beta>\alpha}^{M} \frac{Z_\alpha Z_\beta}{R_{\alpha\beta}} \quad ;$$

$$\hat{V}_{el-nuc} = -\sum_{i=1}^{N}\sum_{\alpha=1}^{M} \frac{Z_\alpha}{r_{i\alpha}} \quad (2.4)$$

Due to the potential contributions in the form of two-particle interactions, $\hat{H}$ can not be separated in N+M mono-particle hamiltonians and an analytical solution of 2.1 is only possible in very simple cases, e.g. the harmonic oscillator or the hydrogen atom. Therefore some approximations have to be undertaken to solve the Schrödinger equation.

2.1.2 The Born-Oppenheimer Approximation

The Born-Oppenheimer approximation[2] is used to separate the motion of the heavy nuclei from that of the lighter electrons by making the assumption that the electrons move in an electro-static field generated by a fixed geometry of the nuclei. This is motivated by the fact that, due to the large mass difference between electrons and nuclei, the former will respond instantaneously to any change of the nuclear configuration. Therefore it is possible to represent the electronic Hamiltonian in a form which depends only parametrically on the nuclear coordinates **R**.

$$\hat{H}_{el} = -\frac{1}{2}\sum_{i=1}^{N} \nabla_i^2 + \sum_{i=1}^{N}\sum_{j>i}^{N} \frac{1}{r_{ij}} - \sum_{i=1}^{N}\sum_{\alpha=1}^{M} \frac{Z_\alpha}{r_{i\alpha}} \quad (2.5)$$

The solution of the stationary Schrödinger equation with this electronic Hamiltonian is the objective of quantum chemistry methods. It results in electronic energies Eel(R) and wavefunctions $\Psi_{el}(r;\mathbf{R})$ which will depend parametrically on the nuclear geometry:

$$\hat{H}_{el}\Psi_{el}(r_i; R_\alpha) = E_{el}(R_\alpha)\Psi_{el}(r_i; R_\alpha) \quad (2.6)$$

The solution of the electronic part of the Schrödinger equation for different nuclear coordinates **R** results in the potential hypersurface V (**R**) when the inter-nuclear repulsion is added. This part of the potential is constant with respect to the electronic coordinates and can be written as:

$$V_n(\boldsymbol{R}) = E_n^{el}(\boldsymbol{R}) + \hat{V}_{nuc-nuc} \tag{2.7}$$

where the adiabatic approximation has been applied leading to a Schrödinger equation for the nucleus:

$$\hat{H}_{nucl}|\Psi_n(R)\rangle = \left(\hat{T}_{nuc} + V_n(\boldsymbol{R})\right)\Big|\Psi_n(r)\rangle = E_n^{nuc}|\Psi_n(r)\rangle \tag{2.8}$$

The adiabatic approximation is justified if the electronic states of the system are separated enough from each other. The sum of the electronic energy plus the nuclear repulsion term constitutes the potential energy surface of the system and represents the central quantity to obtain information about roto-vibrational levels, equilibrium geometries and chemical reactivity. The elimination of the non-adiabatic electronic coupling is the core of the Born-Oppenheimer approximation. Eq. (2.8) describes the geometry of the nuclei in the average field generated by the fast moving electrons. It has to be noticed, that now there will be a different nuclear potential for each electronic state. The dynamics of the nuclei are described reasonably well with the nuclear potential V (**R**) within the Born-Oppenheimer approximation, as long as the potential surfaces belonging to different states stay well separated.

2.1.3 The Electronic Wavefunction

In the following, we will stay within the Born-Oppenheimer approximation and will only be concerned with the electronic Schrödinger equation. For simplicity, we will drop the subscript “el" and the nuclear coordinates **R** from $\Psi_{el}(r;\mathbf{R})$.

The electronic wavefunction has to satisfy following requirements:

- **Normalization.** The wavefunction has to be normalized to unity.
- **Antisymmetry** Since electrons are fermions the wavefunction has to be antisymmetric with respect to the permutation of two electrons.

- **Electronic spin.** Since the electronic Hamiltonian does not contain any spin operators, it does commute with the operators S_z and S^2

$$[H\,,\,S_z] = 0 \qquad ; \qquad [H\,,\,S^2] = 0 \qquad (2.9)$$

where S_z and S^2 are the N-electron spin operators.

The mono-electronic wave functions including the spatial and the spin coordinates are called *spin orbital's* and for each spatial orbital ψ(r) two different spin-orbitals χ can be formed -in correspondence with the spin up and spin down values.

$$\chi(x) = \begin{cases} \psi(r)\alpha(\xi) \\ or \\ \psi(r)\beta(\xi) \end{cases} \qquad (2.10)$$

2.1.4 Slater Determinants

Being stated that the spin-orbitals are the appropriate wavefunctions describing a single electron system, the N-electronic problem has to be considered. A closer inspection of the electronic Hamiltonian 2.5 shows that it contains one- and two-electron terms plus the nuclear repulsion which is independent of the electron coordinates.

$$\hat{H} = \sum_{i=1}^{N} \hat{h}(i) + \sum_{i<j}^{N} g(i,j) + V_{nn} \qquad (2.11)$$

$$\hat{h}(i) = -\frac{1}{2}\nabla_i^2 - \sum_{\alpha=1}^{M} \frac{Z_\alpha}{r_{i\alpha}} \qquad ; \qquad g(i.j) = \frac{1}{r_{ij}} \qquad (2.12)$$

If the two-electron terms were absent, $\hat{\boldsymbol{H}}_{\text{el}}$ would be a sum of terms each one depending only on the coordinates of one electron and it would be separable. Unfortunately, contains the two-electron repulsion terms that are by no means small and cannot be simply neglected. Nevertheless, we start by constructing trial wave functions as products of one-electron wave functions, see Eq. (2.13) and substituting them in Eq. (2.11) and (2.12).

$$\hat{H} = \sum_{i=1}^{N} \hat{h}(i) \qquad (2.13)$$

where $\hat{h}_{(i)}$ can be considered as an elective one-electron Hamiltonian that includes the elects of electron-electron repulsion in some average way.

The eigenfunctions of $\hat{h}_{(i)}$ are defined by the mono-electronic equation

$$\hat{h}(i)_{Xj}(xi) = \epsilon_i X_j(x_i) \tag{2.14}$$

Because $\hat{H}$ is a sum of one-electron Hamiltonians, its eigenfunctions are simple products of mono-electronic spin orbitals (*Hartree product*[3]):

$$\Psi^P(x_1, x_2, \ldots, x_N) = \chi_i(x_1)\chi_j(x_2)\ldots\chi_k(x_N) \tag{2.15}$$

This product is an eigenfunction of $\hat{H}$:

$$\hat{H}\Psi^P = E\Psi^P \tag{2.16}$$

with eigenvalue *E*, which is just the sum of the spin orbital energies of each of the spin orbitals appearing in Ψ^P:

$$E = \epsilon_i + \epsilon_j + \cdots + \epsilon_k \tag{2.17}$$

Assuming independent electrons and a Hamiltonian of the form of Eq. (2.13) the Hartree product does not satisfy the antisymmetry principle and the indistinguishability of electrons is not obeyed. However we can obtain correctly antisymmetrized wave functions writing them in the determinantal form named *Slater determinant*:[4–6]

$$\Psi(x_1, x_2, \ldots, x_N) = (N!)^{-\frac{1}{2}} \begin{vmatrix} \chi_j(x_1) & \chi_j(x_1) \ldots \chi_k(x_1) \\ \chi_j(x_2) & \chi_j(x_2) \ldots \chi_k(x_2) \\ \vdots & \vdots \\ \chi_j(n) & \chi_j(x_n) \ldots \chi_k(x_n) \end{vmatrix} \tag{2.18}$$

Antisymmetrizing a Hartree product introduces exchange effects, so-called because they arise from the requirement that $|\Psi|^2$ be invariant to the exchange of the space and spin coordinates of any two electrons. In particular, a Slater determinant incorporates exchange correlation, which means that the motion of two electrons with parallel spin is correlated.

N-electron wave functions in the form of Slater determinants possess several important properties:

- By construction, they satisfy the antisymmetry property and the Pauli principle.
- They offer an easy interpretation, since it seems very intuitive that an electron is occupying a certain orbital possessing either the spin up or down.
- Whenever spin orbitals are used, Slater determinants are eigenfunctions of the N-electron spin operator S_z with an eigenvalue M_s equal to one-half

$$S_z\Psi = M_s\Psi \qquad ; \qquad M_s = \frac{1}{2}\left(N_\alpha - N_\beta\right) \tag{2.19}$$

of the difference between the number of and electrons.

2.1.5 The Hartree-Fock Method

The Hartree-Fock method seeks to approximately solve the electronic Schrödinger equation, and it assumes that the wavefunction can be approximated by a single Slater determinant made up of one spin orbital per electron. The Hartree-Fock method determines the set of spin orbitals which minimize the energy and give us this best single determinant.

The formulation of the method may be summarized as follows:

- An independent-particle Schrödinger equation neglecting the electronelectron repulsive terms that can be separated in N independent mono-electronic equations is initially formulated.
- The approximated wavefunction, Ψ_{HF} is then obtained as a single determinant built up from the ψ_i.

The repulsive terms previously neglected are inserted in the Hamiltonian and trial energy with the Ψ_{HF} obtained previously is computed.

$$E' = \frac{\int \Psi_{HF}^* \hat{H} \Psi_{HF} d\tau}{\int \Psi_{HF}^* \Psi_{HF} d\tau} \tag{2.20}$$

- The variational principle is the applied to the expression of E' to obtain a set of mono-electronic eigenvalue equations describing the motion of one electron in the mean

field of the other N – 1 electrons. Such equation are known as the Hartree-Fock equations, and for the i-th electron they take the form:

$$\hat{f}(i)\psi(i) = \epsilon_i\psi(i) \tag{2.21}$$

where $\hat{f}_i$ is the mono-electronic Fock operator:

$$\hat{f}(i) = -\frac{1}{2}\nabla_i^2 - \sum_{\alpha=1}^{M}\frac{Z_\alpha}{r_{i\alpha}} + v^{HF}(i) \tag{2.22}$$

$v^{HF}(i)$ is the averaged potential acting on the electron generated by the other electrons.

- Equations (2.21) are coupled integral-differential equations because the Fock operator contains the spin orbitals. Therefore they have to be solved iteratively, through a *consistent field* (SCF) procedure, in which the iteration is driven until the field of the N – 1 electrons is self consistent within a given threshold.

Since the HF method does not take into account electronic correlation by definition, it represents a good approximation only in few cases, such as the ground states of a molecule at its equilibrium geometry. When a more accurate description of electron correlation effects is required, one has to move beyond the HF method. In this sense, it can be seen as the starting point of a number of more accurated *ab-initio* methods. The correlation energy is indeed defined as the difference between the exact energy eigenvalue of the N-electron Hamiltonian and the HF energy. Various ways of including electron correlation gave birth to lot of different theories, some of which are listed below:

- Configuration Interaction (CI)
- Perturbation theories (*e.g.* Rayleigh-Schrödinger, Møller-Plesset)
- Coupled Cluster (CC)
- Multi-Configurational (MC) SCF (*e.g.* Complete Active Space SCF)
- DFT

Here, only the DFT approach will be discussed, which has been extensively used for this thesis work.

2.2 Density Functional Theory

2.2.1 Early Density Functional Theories

The Density Functional Theory (DFT) offers a completely different approach to the resolution of the Schrödinger equation. Its predecessor was the Slater's Xα method[10] formulated in 1951 that was at its time inspired by the Thomas-Fermi model[11] who proposed to express the total energy of a system of interacting electrons as a function of the associated charge density.

The Thomas-Fermi model

The Thomas-Fermi model comes from Fermi-Dirac considerations[11,12] upon the free electron gas in which interactions are given by a Coulombian potential $v(r)$ due to the nucleus. The spatial distribution of the electrons is defined through the electron density $\rho(r)$.

The energy of the system is expressed in terms of the electron density as follows:

$$E[\rho] = T[\rho] + \frac{1}{2}\int\int \frac{\rho(r)\rho(r')}{|r-r'|} dr\, dr' + \int \rho(r)v(r)dr \qquad (2.23)$$

where $T[\rho]$ is the kinetic energy of a non interacting electronic gas of density ρ and ρ(r) determines uniquely $v(r)$. From this idea Hohenberg and Kohn theorem, and modern DFT, have been developed.

The Slater's Xα method

Slater's Xα method was developed as an approximate solution to the HF equations. In this method, the HF exchange was approximated by:

$$E_{X\alpha}[\rho\uparrow, \rho\downarrow] = -\frac{9}{4}\alpha\left(\frac{3}{4\pi}\right)^{\frac{1}{3}}\int\left[\rho_{\uparrow}^{\frac{4}{3}}(r) + \rho_{\downarrow}^{\frac{4}{3}}(r)\right]dr \qquad (2.24)$$

The exchange energy $E_{X\alpha}$ is given here as a functional of densities for spin up (↑) and spin down (↓) electrons and contains an adjustable parameter α.This parameter, was empirically

optimized for each atom of the periodic table[13,14] and its value is between 0.7-0.8 for most atoms.

2.2.2 Hohenberg and Kohn Theorems

The field of rigorous DFT was born in 1964 with the publication of the Hohenberg and Kohn paper[15] where they proved the following:

I. Every observable quantity of a stationary quantum mechanical system is determined by the ground-state density alone.

$$\langle \Psi[\rho] | \hat{O} | \Psi[\rho] \rangle = O[\rho] \tag{2.25}$$

II. The exact ground-state density of a system in a particular external potential can be found by minimization of the energy functional.

$$E_{v0}[\rho] = \langle \Psi[\rho] | \hat{H} | \Psi[\rho] \rangle = O_{[\rho]} \quad ; \quad E_0 = \min_\rho E_{v0}[\rho] \tag{2.26}$$

Therefore, the aim of DFT is not to obtain a good approximation to the ground state wave-function of the system, but rather to find the energy of the system as a functional of the density, without any reference to the wavefunction. The advantage in using the electronic density instead of the wave function is clear: the electronic density is function only of three Cartesian coordinates and one spin coordinate, irrespective of the number of particles, whereas the number of coordinates in the wave function depends linearly from the number of particles.

The Hamiltonian of any molecular system can be written as:

$$\hat{H} = \hat{T} + \hat{V}_{ee} + \hat{V}_{ne} \tag{2.27}$$

where $\hat{T}$ is the kinetic energy operator, $\hat{V}_{ee}$ is the electron-electron interaction operator and $\hat{V}_{ne}$ is the external potential, describing the electronnucleus interactions.

According to the first Hohenberg-Kohn theorem, also the energy of the ground state depends from the electronic density. The electronic energy functional can be separated in different components, depending from the electronic density, and it can be written as follows:

$$E_v[\rho] = F[\rho] + \int \rho(r)v(r)dr \tag{2.28}$$

The latter term represents the electron-nucleus attraction term and is given by:

$$V_{ne}[\rho] = \int \rho(r)v(r)dr \tag{2.29}$$

where $v(r)$ it is the potential generated by the nuclei, given by:

$$v(r) = \sum_\alpha \frac{-Z_\alpha}{|\boldsymbol{R}_\alpha - r|} \tag{2.30}$$

We can write

$$V_{ee}[\rho] = J[\rho] + non - classical\ term \tag{2.31}$$

where $J[\rho]$ is the purely classical repulsion term, called Coulomb potential:

$$J[\rho] = \frac{1}{2}\int\int \frac{1}{r_{12}}\rho(r_1)\,\rho(r_2)\,dr_1 dr_2 \tag{2.32}$$

The nonclassical term is a central quantity in DFT; it contains nonclassical contributions to the total energy, like electronic correlation and exchange terms.

The electronic functional can be written as:

$$E_v[\rho] = F_{HK}[\rho] + \int \rho(r)v(r)dr \tag{2.33}$$

Where

$$F_{HK}[\rho] = T[\rho] + V_{ee}[\rho] \tag{2.34}$$

FHK[p], not containing the external potential $\hat{V}_{\text{ne}}$, is know as the universal functional of the electronic density because is the same for every system of N electrons.

Unfortunately the Hohenberg-Kohn theorem does not provide us with a practical scheme for doing calculations. It does not tell us how to perform the $\rho \rightarrow \Psi$ in practice, and only defines formally what FHK is.

However, the second HK theorem provides a variational principle that can be used to find an solution to the electron density representation ρ(r). For a trial density $\tilde{\rho}$(r) such that $\tilde{\rho}$(r) ≥ 0 and$\int \hat{\rho}(r)dr = N$,

$$E_0 \leq E[\widetilde{\rho}] \tag{2.35}$$

where $[\widetilde{\rho}]$ is the energy functional. In other words, if some density represents the correct number of electrons N, the total energy calculated from this density cannot be lower than the true energy of the ground state.

2.2.3 The Kohn-Sham Equations

The Kohn-Sham equations represent the DFT analogous to the Roothan- Hall equations within the HF theory. The equations are based on the statement that the ground state density of the interacting particle system can be calculated as the ground state density of an auxiliary non-interacting system where the total energy functional is divided into following parts:

$$E[\rho] = T_s[\rho] + J[\rho] + \int v(r)\rho(r)dr + E_{xc}[\rho] \tag{2.36}$$

where $T_s[\rho]$ is the kinetic energy of electrons in a system which has the same density ρ as the real system, but in which there is no electronelectron interactions.

$$\widehat{U}_{cl}(r) = \int \frac{\rho(r')}{|r'-r|} dr' \tag{2.37}$$

is a pure Coulomb ("classical") interaction between electrons. It includes electron self-interaction explicitly, since the corresponding energy is

$$E_{cl}[\rho] = \int \int \frac{\rho(r')\rho(r)}{|r'-r|} drdr' \tag{2.38}$$

and it represents interaction of ρ with itself. $\hat{V}_{ne}$(r) is the potential coming from nuclei:

$$\hat{V}_{ne} = \sum_{\alpha} \frac{-Z_\alpha}{|\boldsymbol{R}_\alpha - r|} \tag{2.39}$$

The last functional, $E_{xc}[\rho]$ is called exchange-correlation energy and includes all the energy contributions which were not accounted for by previous terms, i.e.:

- Electron exchange
- Electron correlation, since non-interacting electrons do need to correlate their movements.
- A portion of the kinetic energy which is needed to correct $T_s[\rho]$ (non-interacting electrons) to obtain true kinetic energy of a real system $T_e[\rho]$.
- Correction for self-interaction introduced by the classical coulomb potential.

All the diffculties in the DFT method arise from the functional, whose exact form can not be known.

The problem consists in the search for a minimum for the energy E_v. The optimal density which minimizes the total energy can be obtained solving the set of mono-electronic equations:

$$\left[-\frac{1}{2}\nabla^2 + v_{eff}(r)\right]\psi_i = \epsilon_i\psi_i \tag{2.40}$$

This set of mono-electronic equations is known as Kohn-Sham equations. They would determine the exact electronic density if it was possible to know the exact dependence of the exchange-correlation functional from but given the dependence of v_{eff} from ρ, the KS equations have to be solved with a SCF iterative procedure. Similarly to HF equations, the KS equations can be solved introducing an expansion of the mono-electronic functions with a suitable basis set:

$$\psi_i = \sum_{q=1}^{N} c_{qi}\chi_q \tag{2.41}$$

where N is the number of basis functions. The set of equations it completely analogous to the set of equations coming from the HF method, the only di erence lying on the fact that the v_{xc}(r) term should be substituted with:

$$\int \sum_j \frac{\psi_j(r)\psi_j(r')}{|r-r'|} dr' P_{rr'} \tag{2.42}$$

A programming code for the computation of molecular properties according to DFT is similar to the HF analogous, substituting the exchange integrals term with the exchange-correlation potential.

2.2.4 Approximations to the Exchange-Correlation (XC) Energy

Clearly, the information about exchange-correlation (XC) energy provided by DFT is not helpful for practical calculations and one needs to use an approximation for this quantity. Some of these approximations will be reviewed in the following. While DFT itself does not give any hint on how to construct approximate XC functionals, it holds both the promise and the challenge that the true E_{xc} is a universal functional of the density, *i.e.*, it has the same functional form for all systems. We will take a short overview on the various models adopted for the XC functional.

Local Density Approximation (LDA)

A first approximate expression for E_{xc} can be obtained according to the local density approximation (LDA), proposed by Kohn and Sham, based on the uniform electron gas model. The LDA, according to the model of the uniform electron gas, consists in expressing the XC term of the energy functional using the XC energy per particle for a uniform electron gas.

$$E_{xc}^{LDA}[\rho] = \int \rho(r)\epsilon_{xc}(\rho)dr \tag{2.43}$$

where $\epsilon_{xc}(\rho)$ is the XC energy per particle for a uniform electron gas[16] of electronic density ρ. Its spin-polarized analogue is the local spin density approximation (LSDA):

$$E_{xc}^{LSDA}[\rho_\alpha, \rho_\beta] = \int \rho(r)\epsilon_{xc}(\rho_\alpha, \rho_\beta)dr \tag{2.44}$$

The term $\epsilon_{xc}(\rho)$ can be splitted in the two separate exchange and correlation contributes, $E_x[\rho]$ and $E_c[\rho]$. The corresponding XC potential is:

$$v_{xc}^{LDA}(r) = \frac{\partial E_{xc}^{LDA}}{\partial \rho(r)} = \epsilon_{xc}[\rho(r)] + \rho(r)\frac{\partial \epsilon_{xc}(\rho)}{\partial \rho} \tag{2.45}$$

and the KS equations (2.36) become:

$$\left[-\frac{1}{2}\nabla^2 + v(r) + \int \frac{\rho(r')}{|r-r'|}dr' + v_{xc}^{LDA}(r)\right]\Psi_i = \epsilon_i \Psi_i \tag{2.46}$$

These equations, known as KS-LDA or simply LDA, can be solved iteratively with a SCF procedure. It can be said that LDA theory derives the XC energy of a non-uniform system applying locally the model of the uniform electron gas to infinitesimal portions of the non-uniform electronic distribution and then summing over all the contributions.

Non local approximations

The previous approximations usually result in an error of about 10% on the exchange energy and even more for the correlation term. The evolution of DFT methods is thus based on the research of accurate XC functionals beyond the LDA approximation. The search of such functionals consists in hypothesizing non local models for the expression of the XC functional and inserting gradient corrections to the uniform electron gas description, in order to take into account not only the density, but also its first and superior derivatives. A more accurate expression for the XC energy can then be written as:

$$E_{xc} = E_{xc}^{LDA} + E_{xc}^{NL} \tag{2.47}$$

where the exchange and the correlation contributions to E_{xc}^{NL} are normally studied separately. In this way, the LDA formulation described in the former section can be corrected in a first approximation by including the gradient of the density in the definition of the exchange functional. The lowest gradient correction (LGC)[17,18] results in considering a functional of the form:

$$E_x^{LGC} = E_X^{LDA} - \beta \sum_\sigma \int \frac{(\nabla \rho_\sigma)^2}{\rho_\sigma^{\frac{4}{3}}} dr \tag{2.48}$$

where β is a constant. A functional of this form suffers severe limitations, giving an exchange potential which diverges asymptotically for atoms and molecules whereas a functional which reproduces the asymptotic limit has been proposed in the form:

$$E_x = E_c^{LDA} - \beta \sum_{\sigma} \rho_{\sigma}^{\frac{4}{3}} \frac{x_{\sigma}^2}{(1 + 6\beta x_{\sigma} \sin h^{-1} x_{\sigma})} \tag{2.49}$$

This functional was proposed by Becke in 1988.[19]

The major problem encountered in the development of modern DFT was largely due to the correct description of electron correlation. Local models result in an overestimation of the correlation energy, which leads to inaccuracy in the treatment of inhomogeneous systems. The development of an adequate theory for electron correlation plays a fundamental role for the practical use of DFT based methods. The definition of correlation functionals results generally more difficult than the correspondent formulation for an exchange functional. A general description of the various correlation functionals is presented below.

- Perdew 86 (P86).[20] It has been obtained by following the so-called wave vector analysis, in which the correlation energy is decomposed in its different wave length components. The P86 functional was derived from the Langreth and Mehl[21-24] and can be written as:

$$E_c^{P86}[\rho^{\alpha}, \rho^{\beta}] = \int \rho\,(r) \epsilon_c(\rho^{\alpha}, \rho^{\beta}) dr + \int \frac{d^{-1} e^{-\phi} C(\rho) |\nabla \rho|^2}{\rho^{4/3}} dr \tag{2.50}$$

  This functional has been widely used and has proved to give better results for atoms and molecules than the functionals from which it was derived.

- Lee-Yang-Parr (LYP).[25] The original idea for this correlation functional is embedded in the Colle-Salvetti formula,[26] in which the correlation energy is expressed as a function of the electron density and of the Laplacian of the second order HF density matrix. The LYP correlation energy corrections are written as:

$$E_C^{LYP} = -a \int \frac{1}{1 + d\rho^{-1/3}} \Big\{ \rho_b \rho^{-2/3} \Big[C_F \rho^{5/3} - 2t_W + \Big(\frac{1}{9} t_W + \frac{1}{18} \nabla^2 \rho \Big) \Big] \exp(-c\rho^{-1/3}) \Big\} dr \tag{2.51}$$

The constants a, b, c, d where determined from a fitting procedure on the He atom and it was demonstrated that such a formula reproduces accurately the correlation energies for atoms and molecules.

- Perdew-Wang 91 (PW91).[27] The *Perdew-Wang 91* functional was proposed as a modification of the P86 functional, based on a new formulation for the expression of the correlation energy of the uniform electron gas. An analytic representation for the correlation energy is indeed necessary for the construction of energy functional, which results to be accurate both in the local and non local approximation[28,29] and is particularly appropriate in the description of magnetic effects.[30] The correlation energy per electron, $\epsilon_c(r_s, X)$ in the limit of small values of r_s, *i.e.* for high densities, is given by:[31-33]

$$\epsilon_c(r_s, X) = c_0(X) ln\, r_s - c_1(X) + c_2(X) r_s ln\, r_s - c_3(X) r_s + \ ... \qquad (2.52)$$

The correspondent expression for high values of r_s, i.e. in the limit of small densities, is instead given by:[34]

$$\epsilon_c(r_s, X) = \frac{-d_0(X)}{r_s^p} + \frac{d_1(X)}{r_s^{2p-1/2}} + \ ... \qquad (2.53)$$

Perdew and Wang demonstrated instead that the exponent p has a value of 3/4.[35] The procedure, by which the correspondent functional has been obtained, consists of elaborate mathematical interpolation tools on data obtained by quantum Monte Carlo methods,[32-35] and will not be presented in the following.

Hybrid functionals

The functionals presented previously are the ones rigorously established by DFT, being composed by pure parts of exchange and correlation. A different approach to the definition of XC functionals is the one diffused by Becke,[36,37] leading to the definition of the so-called hybrid functionals, in which terms from the HF theory and from DFT are used together. The underlying idea of the derivation proposed by Becke is to mix HF theory and DFT in a general theory including the aspects which demonstrated to be more accurate for each method. Indeed, it is well known that HF theory gives an exact description of exchange

interactions, while suffering of severe limitations in the description of the correlation term; on the other hand, DFT offers a much easier way to introduce electron correlation effects, compared to post HF methods. It is to be underlined that the definition of "HF theory" is not rigorously correct in the framework of DFT, therefore the term "exact exchange" is generally used. The exchange contribution results are the largest in the formulation of an XC functional; one can therefore, in a first approximation, treat the correlation term inserting the correspondent result taken from the LSDA approximation. In this case the exchange energy can be expressed as:

$$E_{xc} = E_x + E_C^{LSDA} \tag{2.54}$$

where E_x is the exchange energy obtained from the Slater determinant built with the molecular orbitals, which are solution of the exact KS equations. Notably, E_x does not represent strictly the HF exchange energy, because the HF molecular orbitals do not correspond to the KS ones.

On the basis of the previous considerations, Becke has proposed a novel partition of the XC term, based on a formula known as adiabatic connection,[38] which gives in principle a rigorous definition for the XC energy. According to the adiabatic connection we can express the exchange correlation energy as:

$$E_{xc} = \int_0^1 U_{xc}^{\lambda}\, d\lambda \tag{2.55}$$

where λ is an interelectronic coupling parameter, and U_{xc}^{λ} is the exchange correlation potential energy for intermediate values of the parameter λ. Adopting this definition, the KS non-interacting system (λ = 0) can be connected with the fully interacting one (λ = 1) through a continuum of partially interacting systems, which share the same density function ρ, defined as the density of the fully interacting system.

Even if the explicit calculation of the terms appearing in equation (2.56) through *ab initio* methods cannot be performed directly, the previous equation can be used to build accurate XC functionals. A first approximation that can be conceived is to consider a linear dependence from λ:

$$E_{xc} = \frac{1}{2}U_{xc}^{0} + \frac{1}{2}U_{xc}^{1} \tag{2.56}$$

where U_{xc}^{0} represents the XC potential energy for the non-interacting system, and U_{xc}^{1} the correspondent quantity for the fully interacting one.

In this case U_{xc}^{0} represents the pure exchange energy, referred to the Slater determinant built up from the KS orbitals and can be computed exactly, while for λ = 1 one can approximate U_{xc}^{1} through the LSDA approximation:

$$U_{xc}^{1} \cong U_{xc}^{LSDA} = \int u_{xc}\left[\rho_{\alpha}(r), \rho_{\beta}(r)\right]dr \tag{2.57}$$

where u_{xc} represents the interaction XC potential. Considering the changing in E_{xc}, we can re-write Eq. (2.55) as:

$$E_{xc} \cong \frac{1}{2}E_{x} + \frac{1}{2}U_{x}^{LSDA} \tag{2.58}$$

A generalization of Eq. (2.59) has been proposed, in which two adjustable parameters, c_0 and c_1, replace 1/2, obtaining:

$$E_{xc} = c_0 E_x + c_1 U_{xc}^{LSDA} \tag{2.59}$$

The coefficients have been determined with a best-fit procedure considering the G1[39,40] data base, and resulted in the following two values: c_0 = 0:332 and c_1 = 0:575. The results obtained lead to accurate thermochemical data, even if they result less accurate when computing absolute energies and ionization potentials.

The last development of the theory proposed by Becke, consists in relaxing the linear dependence from λ, and considering gradient corrections both for the exchange and correlation terms. Following this line, a three adjustable parameters hybrid functional has been devised, which constitutes the model on which all the others hybrid functional have been built up. The three-parameters functional takes the form:

$$E_{xc} = E_{xc}^{LSDA} + a_0(E_x^{exact} - E_x^{LSDA}) + a_x \Delta E_x^{B88} + a_c \Delta E_c^{PW91} \tag{2.60}$$

where a_0, ax, and a_c are best-fit adjustable parameters and E_c^{exact} represents the exact exchange term. ΔE_x^{B88} is the gradient correction to exchange coming from the *Becke88* functional, and ΔE_c^{PW91} is the gradient correction to correlation due to the PW91 functional. Of course, the three-parameters functional is open to the insertion of different XC functionals leading for example to the B3PW91 or B3LYP functionals, where PW91 and LYP correlation functionals are used, respectively.

2.3 Plane-waves DFT approach

Although the complicated many-body problem of interacting electrons in the Coulomb potentials of fixed nuclei has been simplified to a set of single-particle equations, the calculation of the one-electron wave functions for an extended (or even infinite) system is still a formidable task if we use localized basis set functions. On the contrary, plane waves are a particular well-suited set of basis functions for extended systems. In the plane wave approaches the Coulomb potential of the electron-nucleus interaction is replaced by pseudopotentials.

The procedure has several advantages:[41]

- Plane waves are the exact eigenfunctions of the homogeneous electron gas: therefore, they are the natural choice for a basis expansion of the electron wave functions for simple metals where the ionic cores can be viewed as rather small perturbations to the homogeneous electron gas;

- Plane waves are orthonormal and energy-independent and they are not biased to any particular atom. Any region in space is treated on an equal footing so that calculations do not have to be corrected for a basis set superposition error;

- Plane waves approach guarantees to converge to the target wave function, while there is no such guarantee for Gaussian type basis sets;

- The basis set is constructed in such a way that only plane waves up to a certain cutoff wave vector are included;

- Relativistic effects can be incorporated into the pseudopotential, while further treating the valence electrons non-relativistically;

- Even if the number of basis functions needed for an accurate calculation is an order of magnitude larger than for methods that rely on localized orbitals, the possibility to evaluate many expressions with the help of the Fast Fourier Transform (FFT) algorithm largely compensates in terms of time-consuming calculations.

2.3.1 Independent Electrons in a Periodic Potential: Bloch's Theorem

Bloch's theorem states that all eigenfunctions of a single-particle Schrödinger equation with a periodic potential can be written as a periodic function modulated by a plane wave with wave vector *k*:

$$\psi_{k_j}(r) = e^{ikr} u_{k_j}(r) \tag{2.61}$$

Thus, the calculation of the eigenfunctions can be restricted within one-unit cell. Assuming that the wave-functions are normalized within a single unit cell and since the functions $u_{k_j}(r)$ are periodic, they can be expanded in a set of plane waves:

$$\psi_{k_j}(r) = \sum_G c_G^{k_j} e^{i(k+G)r} \tag{2.62}$$

2.3.2 KS equations in the plane-waves framework

Following Block-states notation the KS equations can be written as:

$$\left(-\frac{\hbar^2}{2m}\nabla^2 - V_{eff}(r)\right)\psi_{k_j}(r) = \varepsilon_{k_j}\psi_{k_j}(r) \tag{2.63}$$

where:

$$V_{eff}(r) = V_{ext}(r) + V_H[\rho(r)] + V_{xc}[\rho(r)] \tag{2.64}$$

and:

$$\rho(r) = 2\frac{\Omega_c}{(2\pi)^3}\sum_j \int \psi_{k_j}(r)^2 \Theta\left(E_F - \varepsilon_{k_j}\right) d^3k \tag{2.65}$$

V_{ext}, V_H and V_{xc} are the external potential of the nuclei, the Hartree and the XC potential, respectively. By the factor of 2 in Eq. (2.66) we take the electron spin into account. Θ is a step function which is 1 for positive and 0 for negative arguments. E_F is the Fermi energy up to which single-particle states have to be occupied. If we insert Eq. (2.66) into Eq. (2.64), multiply from left with $e^{i(k+G')r}$ and integrate over *r*, we get the matrix eigenvalue equation that is the Fourier representation of the KS equations:

$$\sum_G \left(-\frac{\hbar^2}{2m} \|G + k\|^2 \delta_{G'G} + V_{eff}(G' - G) c_G^{k_j} = \varepsilon_{k_j} c_{G'}^{k_j} \right) \tag{2.66}$$

In practical calculations, the Fourier expansion of the wave functions is truncated by keeping only those plane wave vectors with a kinetic energy lower than a given cutoff value, E_{pw}. The convergence of all calculations with respect to the basis set size can be tested simply by increasing step by step the plane wave cutoff energy.

The problem of calculating an infinite number of electronic states extended infinitely in space has been transformed to one of calculating a finite number of eigenstates at an infinite number of *k*-points which are extended over a single unit cell, which seems to be only a minor improvement, since still an infinite number of calculations are needed for the different *k*-points. However, since the electronic wave functions at *k*-points, which are close together, are very similar, it is possible to represent the wave functions of a region of *k*-space by the wave function at a single *k*-point. We thus define a regular mesh of *k*-points and replace the integral over the Brillouin zone by a discrete sum over the chosen *k*-point mesh:

$$\frac{\Omega_c}{(2\pi)^3} \int \dots \Theta(E_F - \varepsilon_{k_i}) d^3k \;\rightarrow\; \frac{1}{N_{kpt}} \sum_k f_{k_j} \dots \tag{2.67}$$

The f_{k_j} are occupation numbers which are either 1 or 0. Within this approximation, only the electronic states at a finite number of *k*-points are needed to calculate the charge density and hence the total energy of the solid. The error induced by this approximation can be reduced systematically by increasing the density of the *k*-point mesh. For increasing size of the supercell, the volume of the Brillouin zone becomes smaller and smaller and less *k*-points are needed. From a certain supercell size on, it is often justified to use the Γ-point approximation where a single *k*-point is used, usually $k = 0$.

2.3.3 Pseudopotentials

Most physical and chemical properties of crystals depend on a very good approximation only on the distribution of the valence electrons. The core electrons do not participate in the chemical bond. They are strongly localized around the nucleus, and their wave functions overlap only very little with the core electron wave functions from neighboring atoms. Therefore, the distribution of the core electrons basically does not change when the atoms are placed in a different chemical environment. It is thus justified to assume the core electrons to be *frozen* and to keep the core electron distribution of the isolated atom in the crystal environment. The ionic core potential is replaced by a pseudopotential which leads to nodeless valence wave functions. In the pioneering work of Haman, Schlüter and Chiang (HSC),[42] a scheme to construct a pseudopotential within the LDA framework was proposed.

Norm-conserving Pseudopotentials

Present day pseudopotentials are constructed from *ab initio* calculations for isolated atoms. Let us assume we have solved the KS equations for each atom of the chemical species for which we would like to generate a pseudopotential. This can be done easily since, due to the spherical symmetry of atoms, the wave functions can be written as a product of a radial function and a spherical harmonic. The Schrödinger equation then reduces to onedimensional differential equations for the radial functions, which can be integrated numerically.

The main goal is to replace the effective all-electron potential within a given sphere with radius, R_{cut}, by a much weaker new potential with a nodeless ground state wave function to the same energy eigenvalue, as the original all-electron state, which matches exactly the all-electron wave function outside. Being ε_l^{AE} the construction of such a pseudopotential, can be done as following:

- The all-electron wave function (ϕ_l^{AE}) inside the sphere is replaced by an arbitrary smooth nodeless function (ϕ_l^{PS}) with the same logarithmic derivative at R_{cut} as the original all-electron function;

- Since the ϕ_l^{PS} is nodeless, we can simply invert the radial Schrödinger equation with this new function and with the eigenvalue ε_l^{AE} of the all-electron calculation to get the potential;

- The all-electron and the pseudo-wave function inside the atomic sphere are forced to have the same norm to guarantee that both wave functions generate identical electron densities in the outside region (Norm Conserving Condition);

- The additional degrees of freedom in generating a suitable pseudopotential can be employed to make the pseudo wave functions as smooth as possible to fasten calculations.[43]

There is a quite large extend of freedom to setup the new pseudo-wave function and over the last decades many different recipes have been published.[43-50]

Vanderbilt *"Ultra-soft" Pseudopotentials*

Elements with nodeless valence states (in particular those with 2*p* and 3*d* valence electrons) are very difficult to treat within a pseudopotential scheme. For such elements, the pseudo and the all-electron wave functions are almost identical. Since these valence electrons are strongly localized in the ionic core region, many plane waves are required for a good representation of their wave function, which often makes calculations for such elements prohibitively expensive.

To circumvent this problem, Vanderbilt has introduced a new type of pseudopotentials, the so-called ultrasoft pseudopotentials, in which the normconserving requirement has been relaxed.[51,52] Instead of representing the full valence wave function by plane waves, only a small portion of the wave function is calculated within the Vanderbilt ultrasoft pseudopotential scheme. This allows to reduce substantially the plane wave cutoff energy in the calculations. The price to pay, however, is that the Fourier representation of the KS equation becomes more complicated.

- Once the electron density is calculated, we have to add back the part of the electron distribution, the so-called augmentation charges;

- Due to the relaxation of the norm-conserving condition, the Bloch eigenstates will be not orthonormal anymore. An overlap matrix has to be introduced;

- The nonlocal part of the pseudopotential becomes density-dependent;

- As a consequence to these modifications, additional terms in the force calculation have to be evaluated.

Despite the drawback mentioned above, the gain in computational cost by lowering the plane wave cutoff energy outweighs in many cases the additional computational effort, which is required by these modifications.

References

[1] Schrödinger, E. *Phys. Rev.* **1926**, *28*, 1049-1070.

[2] Born, M.; Oppenheimer, J. R. *Annalen der Physik* **1927**, *84*, 467.

[3] Hartree, D. R. *Proc. of the Cambridge Philos. Soc.* **1928**, *24*, 426.

[4] Slater, J. C. *Phys. Rev.* **1929**, *34*, 1293.

[5] Slater, J. C. *Phys. Rev.* **1930**, *35*, 509.

[6] Fock, V. *Zeitschrift für Physik* **1930**, *61*, 126.

[7] Roothaan, C. *Review in Modern Physics* **1951**, *23*, 161.

[8] Hall, G. *Proc. of the Royal Soc.* **1951**, *A205*, 541.

[9] Møller, C.; Plesset, M. S. *Phys. Rev.* **1934**, *46*, 622.

[10] Slater, J. C. *Phys. Rev.* **1951**, *81*, 385-390.

[11] Fermi, E. Zeitschrift fur Physik 1926, 36, 902.

[12] Dirac, P. A. M. *Proc. of the Royal Soc.* **1926**, *A112*, 661.

[13] Slater, J. C. *The Self-Consistent Field for Molecules and Solids*; McGraw-Hill, 1974.

[14] Schwarz, K. *Phys. Rev. B* **1972**, *5*, 2466-2468.

[15] Hohenberg, P.; Kohn, W. *Phys. Rev.* **1964**, *136*, B864-B871.

[16] Ziegler, T. *Chem. Rev.* **1991**, *91*, 651-667.

[17] Herman, F.; Dyke, J. P. V.; Ortenburger, I. B. *Phys. Rev. Lett.* **1969**, *22*, 807-811.

[18] Herman, F.; Dyke, J. P. V.; Ortenburger, I. B. *Int. J. Quant. Chem.* **1970**, *3*, 827.

[19] Becke, A. D. *Phys. Rev. A* **1988**, *38*, 3098-3100.

[20] Perdew, J. P. *Phys. Rev. B* **1986**, *33*, 8822-8824.

[21] Langreth, D. C.; Perdew, J. P. *Phys. Rev. B* **1980**, *21*, 5469-5493.

[22] Langreth, D. C.; Mehl, M. J. *Phys. Rev. B* **1983**, *28*, 1809-1834.

[23] Hu, C. D.; Langreth, D. C. *Physica Scripta* **1985**, *32*, 391.

[24] Hu, C. D.; Langreth, D. C. *Phys. Rev. B* **1986**, *33*, 943-959.

[25] Lee, C.; Yang, W.; Parr, R. G. *Phys. Rev. B* **1988**, *37*, 785-789.

[26] Colle, R.; Salvetti, D. *Theor. Chim. Acta* **1975**, *37*, 407.

[27] Perdew, J. P.; Wang, Y. *Phys. Rev. B* **1992**, *45*, 13244-13249.

[28] Kohn, W.; Sham, L. J. *Phys. Rev.* **1965**, *140*, A1133-A1138.

[29] von Barth, U.; Hedin, L. *J. Phys.: Condens. Matter* **1972**, *5*, 1629.

[30] Singh, D.; Clougherty, D. P.; MacLaren, J. M.; Albers, R. C.; Wang, C. S. *Phys. Rev. B* **1991**, *44*, 7701-7703.

[31] Gell-Mann, M.; Brueckner, K. A. *Phys. Rev.* **1957**, *106*, 364-368.

[32] Perdew, J. P.; Zunger, A. *Phys. Rev. B* **1981**, *23*, 5048-5079.

[33] Aguilera-Navarro, V. C.; Baker, G. A.; de Llano, M. *Phys. Rev. B* **1985**, *32*, 4502-4506.

[34] Ceperley, D. M.; Alder, B. J. *Phys. Rev. Lett.* **1980**, *45*, 566-569.

[35] Wang, Y.; Perdew, J. P. *Phys. Rev. B* **1991**, *44*, 13298-13307.

[36] Becke, A. D. *J. Chem. Phys.* **1993**, *98*, 1372-1377.

[37] Becke, A. D. *J. Chem. Phys.* **1993**, *98*, 5648-5652.

[38] Harris, J.; Jones, R. O. *J. Phys.: Condens. Matter* **1974**, *4*, 1170.

[39] Pople, J. A.; Head-Gordon, M.; Fox, D. J.; Raghavachari, K.; Curtiss, L. A. *J. Chem. Phys.* **1989**, *90*, 5622.

[40] Curtiss, L. A.; Jones, C.; Trucks, G. W.; Raghavachari, K.; Pople, J. A. *J. Chem. Phys.* **1990**, *93*, 2537.

[41] Meyer, B. *The Pseudopotential Plane Wave Approach. In Computational Nanoscience: Do It Yourself !, NIC Series Volume 31*; J. Grotendorst, S. Blügel, D. Marx, **2006**.

[42] Hamann, D. R.; Schlüter, M.; Chiang, C. *Phys. Rev. Lett.* **1979**, *43*, 1494-1497.

[43] Rappe, A. M.; Kaxiras, E.; Joannopoulos, J. D. *Phys. Rev. B* **1990**, *41*, 1227-1230.

[44] Bachelet, G. B.; Hamann, D. R.; Schl□ıter, M. *Phys. Rev. B* **1982**, *26*, 4199-4228.

[45] Kerker, G. *J. Phys. C: Sol. State Phys.* **1980**, *13*, L189.

[46] Troullier, N. *Sol. State Com.* **1990**, *74*, 613-616.

[47] Troullier, N.; Martins, J. L. *Phys. Rev. B* **1991**, *43*, 1993-2006.

[48] Vanderbilt, D. *Phys. Rev. B* **1985**, *32*, 8412-8415.

[49] Goedecker, S.; Hutter, J. *Phys. Rev. B* **1996**, *54*, 1703-1710.

[50] Hartwigsen, C.; Goedecker, S.; Hutter, J. *Phys. Rev. B* **1998**, *58*, 3641-3662.

[51] Vanderbilt, D. *Phys. Rev. B* **1990**, *41*, 7892-7895.

[52] Laasonen, K.; Car, R.; Lee, C.; Vanderbilt, D. *Phys. Rev. B* **1993**, *47*, 10142-10153.

Chapter 3

Density Functional Theory modelling of the structural and isotopic properties of ZnO nanoparticles

3.1 Introduction

Zinc oxide nanoparticles are commonly used in several domains of human activity due to their low cost and interesting properties. ZnO is an inorganic crystalline compound with a band-gap energy located in the UV region that widens as the size of the particles decreases below a threshold of a few nanometers. Both in the bulk form and as a nanoscale material, ZnO is an important material for several applications including in electronics and optical devices.[1] ZnO nanoparticles may be synthesized by a variety of methods, selected based on the desired application, morphology, and size. Chemical and physical parameters are of high relevance in the synthesis protocols. A variety of shapes (nanorods, nanosphere, nanotubes, nanowires, nanoneedles, nanorings, spirals, drums, polyhedrons, disks, flowers, stars, boxes, and plates) may be produced, each displaying morphological-dependent physicochemical properties[2] that allow the exploitation of a variety of applications.

Some preparative methods include chemical vapor deposition, precipitation in aqueous solution, hydrothermal synthesis, and synthesis using microemulsions and mechanochemical processes. These methods allow the production of particles differing in shape and size. Some available reviews present a thorough explanation of the principles and techniques involved in the different procedures.[3] The hydrothermal method is a simple and environmentally friendly technique that involves the thermal treatment of Zn(II) aqueous solutions under auto-generated pressure, by using an autoclave as the reaction vessel. ZnO nanoparticles have also been prepared using a Zn(II) precursor in the presence of plant extracts[4,5] as cost-effective approaches, with promising results in terms many applications.

The routine methodologies used to characterize ZnO nanoparticles include dynamic light scattering (DLS) techniques, UV-VIS absorption spectroscopy, and powder X-ray diffraction (XRD). The size and shape of the nanoparticles are directly analyzed by using microscopy (transmission electron microscopy–TEM, atomic force microscopy–AFM, or scanning electron–SEM). The crystalline phase can be identified by using XRD and the surface charge of the colloidal nanoparticles through zeta potential measurements. A number of processes involving nanoparticles are mediated by the surface. Although its characterization is not straightforward, important information can be acquired by using Fourier transform infrared spectroscopy (FT-IR), Raman spectroscopy, and X-ray photoelectron spectroscopy (XPS) among other techniques.

Increase in production and applications of ZnO nanoparticles is expected to result in its increased release into the environment. Ultimately, the aquatic ecosystems will probably be the main recipients, mainly as a result of industrial and domestic wastewaters.[6] ZnO nanoparticles environmental release may occur as early as their production, production of products containing nanoparticles, during their use and end of life of those products. Despite the knowledge that nanoparticles are increasingly being used in different fields of human activity, the quantification of their release in the environment, at any given time, is quite challenging due to the limited data on their current and expected prevalence in commercial products.[7,8] The technical difficulties associated with quantification of ZnO nanoparticles levels in the environment led to the need to predict environmental concentrations based on market penetration of nanomaterials, known usage of the products as well as fate/behavior. Once released into the environment, ZnO nanoparticles may display different behaviors. Nanoparticles in the environment may stay in suspensions as individual particles; dissolve; aggregate; form larger particles and ultimately sediment; adsorb onto water constituents (e.g., dissolved organic matter); transform chemically (e.g., due to redox reactions) or biologically (e.g., in the presence of microorganisms) in the marine environment.[9] Once in the environment, most ZnO nanoparticles are likely to precipitate due to its poor colloidal stability.[10] However, the presence of natural substances such as humic acids may help to steric and electrostatic stabilization of ZnO nanoparticles, aiding in their transport, mobility, and dispersion.[11] Other highly relevant alterations that may occur in the environment and lead to toxic effects of ZnO nanoparticles are the dissolution and redox transformations.

In this work, computer simulations complement the direct materials analysis of ZnO systems. In particular, we focused our theoretical study on the assessment of the surface effect on the isotopic signature. Do ZnO nanoparticles have different Zn isotope composition from bulk ZnO crystals in equilibrium conditions? In order to address this question, we performed structure and frequency calculations based on density functional theory (DFT) on various structural models. Isotopic properties are then determined from the vibrational frequencies. Three kinds of structural models were considered: ZnO bulk structure, the slab surfaces $(1\ 0\ \bar{1}\ 0)$ and $(2\ \bar{1}\ \bar{1}\ 0)$, and a model nanoparticle. The results obtained allow us to discuss the surface effect and the isotopic properties of ZnO nanoparticles.

3.2 Computational Methodologies

A DFT-based approach has been employed using Quantum espresso package.[12] The Perdew-Burke-Ernzerhof (PBE) parametrised generalised gradient approximation (GGA) functional has been used in the calculations.[13] Ultrasoft pseudopotentials from the GBRV library are used.[14]

A full geometry optimisation of the bulk zincite cell of ZnO is performed. We optimised the total energy and lattice parameters with respect to the plane wave cutoff energy and number of k-points. The cut-off energies for wave-functions (80 Ry) and charge-density (720 Ry) are determined such as the total energies are converged within 1 mRy/atom. The *k*-point grid which includes the Gamma point is 3×3×2 for the primitive unitcell.

The surface calculations for $(1\ 0\ \bar{1}\ 0)$ and $(2\ \bar{1}\ \bar{1}\ 0)$ surfaces were performed using a periodic slab model such that these surfaces were cleaved from the relaxed bulk structure obtained above. The number of *k* points was tested for both slabs to give converged results and the selected grid is 3×3×1. As explained in section 3.3, only the atomic positions of the surface layers were relaxed.

$(ZnO)_{48}$ nanoclusters of prismatic shape have been set up starting from the bulk structure. The polarity of the ZnO terminated (0001) surface establishes an unrealistic net dipole moment along the c axis, which diverges with increasing dimension along this axis, as well as the surface energy.[15-17] Proper saturation of unsaturated sites has shown to decrease the dipole along the c axis, and to stabilize the nanoparticle. Therefore, we saturate the polar surfaces by dissociating H_2O molecules, adsorbing H^+ and OH^- ions on the unsaturated O and Zn sites

respectively. The dissociative adsorption of water in the polar surfaces of ZnO has been found to be energetically favorable[15]. Thus, we follow the same approach for $(ZnO)_{111}$. The nanoparticle structures were fully optimized.

Following structural relaxations, frequency calculations were performed to study the change of isotopic properties associated with size and surface effects. Zn displays five stable isotopes with atomic masses 64, 66, 67, 68, and 70 and relative abundances of 48.6%, 27.9%, 4.1%, 18.8% and 0.6% respectively. The equilibrium isotopic fractionation factor $\alpha(a, b, Y)$ between two phases *a* and *b* of an element Y is defined as the ratio of isotope ratios and can also be written as the ratio of the reduced partition function ratios:

$$\alpha(a, b, Y) = \frac{\beta(a, Y)}{\beta(b, Y)}$$

where β(a,Y) is the reduced partition function ratio between phase *a* and a perfect gas of atoms Y.[18] Isotopic properties are determined from the vibrational frequencies of the system through the determination of reduced partition function ratios (β-factors) according to this equation:[18]

$$\beta(a, Y) = \left[\prod_{i=1}^{3N_{at}} \prod_{\{q\}} \frac{v_{\boldsymbol{q},i}}{v'_{\boldsymbol{q},i}} \frac{\exp(-hv_{\boldsymbol{q},i}/2k_BT)}{1-\exp(-hv_{\boldsymbol{q},i}/k_BT)} \frac{1-\exp(-hv'_{\boldsymbol{q},i}/k_BT)}{\exp(-hv'_{\boldsymbol{q},i}/2k_BT)} \right]^{1/(N_qN)}$$

$v'_{\mathbf{q},i}$ and $v_{\mathbf{q},i}$ are the vibrational frequencies with wave vector $\boldsymbol{q}$ and branch index i = 1,3N_{at} in two isotopologues. N_{at} is the number of atoms in the crystal unit-cell with N sites for the Y atoms. T is the temperature, h the Planck constant and k_B the Boltzmann constant. The second product is performed on a sufficiently large grid of N_q $\boldsymbol{q}$-vectors in the Brillouin zone. This equation takes advantage of the high-temperature product rule imposing the isotope fractionation to be nil at very high temperatures.

The harmonic approach has been used to compute the β-factor which has been fully presented by Blanchard et al.[19] To explain briefly, the harmonic quantum molecular partition function of a molecule can be written as a product of translational, rotational, vibrational and electronic partition functions. The electronic structure of a crystal is usually assumed to be isotope-independent, so the electronic term is neglected. The energy differences associated with translation motions cancel at equilibrium and the rotational term disappears in crystals. Therefore only the vibrational term plays an important role in the determination of the

isotopic properties. In crystals, a vibrational mode is defined by a frequency of vibration, the atomic displacement pattern in a given cell and a wave-vector q that describes the phase relation of the atomic displacements in the other cells of the crystal. The wave-vector is defined in the reciprocal space and belongs to the first Brillouin zone. The vibrational frequency thus depends on the wave-vector. It is possible to build dispersion curves by reporting the frequency along specific directions in the reciprocal space, and vibrational density of states by integration over the whole Brillouin zone. For the aim of computing the reduced partition function ratios in the harmonic approximation according to the above equation, the complete vibrational spectrum is needed. However, beyond a certain number of wave-vectors, results are converged. For each system, the dynamical matrix is calculated within density functional perturbation theory and then diagonalised for two different Zn atomic masses (64 and 66) in order to obtain the vibrational frequencies of the two isotopologues. We can either substitute all Zn atoms of the system at once in order to obtain the bulk β-factor, or substitute only one Zn atom in order to obtain the site-by-site β-factor.

3.3 Results and Discussion

3.3.1 ZnO bulk structure

We performed first a full geometry optimization for the bulk ZnO in its zincite crystal structure (hexagonal space group $P6_3mc$, Figure 3.1). Optimized structural parameters compare well with the experimental values (Table 3.1)[20], as well as other experimental and theoretical values obtained previously.[21-25] Vibrational frequencies were then calculated on the optimized structure in order to determine the equilibrium fractionation factor for Zn using the equation of section (2). The value of β-factor for ZnO bulk where Zn atoms are four-fold coordinated with O atoms is 3.96 ‰ at 273 K. The stiffness of the interatomic bonds that controls the β-factor can be evaluated by the interatomic force constants. Zn interatomic force constant was calculated from the dynamical matrix for 0.190 Ry/bohr² by averaging the force constants of each Zn atom in the three spatial dimensions x, y, z.

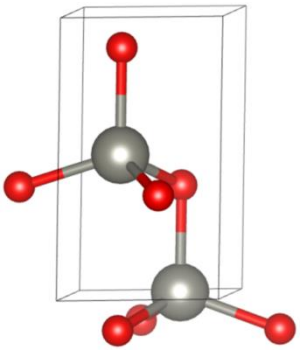

Figure 3.1 Relaxed structure for ZnO bulk (zincite)

	a (Å)	c (Å)	α_O	α_{Zn}	Zn–O (Å)
This study	3.277	5.308	108.8	108.8	2.01
Experiment[10]	3.249	5.204	108.0	108.0	2.0

Table 3.1 Comparison of calculated and experimental structural parameters of ZnO zincite. α_O and α_{Zn} correspond to Zn-O-Zn and O-Zn-O angles respectively (in °).

3.3.2 ZnO surfaces

3.3.2.1 (1 0 $\bar{1}$ 0) and (2 $\bar{1}$ $\bar{1}$ 0) ZnO surfaces

(1 0 $\bar{1}$ 0) and (2 $\bar{1}$ $\bar{1}$ 0) ZnO surfaces which are non-polar surfaces were investigated using periodic slab models. Slabs of 8 ZnO layers (32 atoms) corresponding to these two surfaces were cleaved from the bulk optimized ZnO zincite structure. A vacuum layer with a thickness of 10 Å was inserted in the z-direction. During the calculations, only the 4 top ZnO layers of the slabs were free to relax, while keeping fixed the dimensions of the simulation cells. The geometric parameters that have been calculated for the two surfaces are presented in Figure 3.2 and Table 3.2.

For the (1 0 $\bar{1}$ 0) surface, each surface atom is threefold coordinated, bonding to one surface atom and two next layer atoms, all of the same atom type (i.e., Zn surface atoms are bonded to 3 O atoms while O surface atoms are bonded to 3 Zn atoms). Our results indicate that the Zn surface atom relaxes inwards by −0.34 Å, while the O surface atom moves slightly outward by 0.01 Å, resulting in tilting of the Zn–O bond by 10.37◦. The ZnO bond length shortens by 0.14 Å to become 1.86 Å. The O–Zn–O angle (α_{Zn}) increases from 108.8° to

118.9°, while the Zn–O–Zn angle (α_O) decreases from 108.8° to 103.9°. The calculated values are in good agreement with previous theoretical and experimental studies.[21,26,27]

For the $(2\,\bar{1}\,\bar{1}\,0)$ surface, the surface atoms (Zn or O) are again threefold coordinated, however, each atom is bonded to two surface atoms and one next layer atom. The Zn surface atom is found to move inward by −0.22 Å, while the O atom moves outward by 0.03 Å, resulting in a tilting of the Zn–O bond by 7.82°, and shortening to 1.88 Å. The angle α_{Zn} increases from 108.8° to 110.7°, while the angle α_O decreases from 108.8° to 107.3°. Our results are generally in agreement with previous studies.[21,27,28]

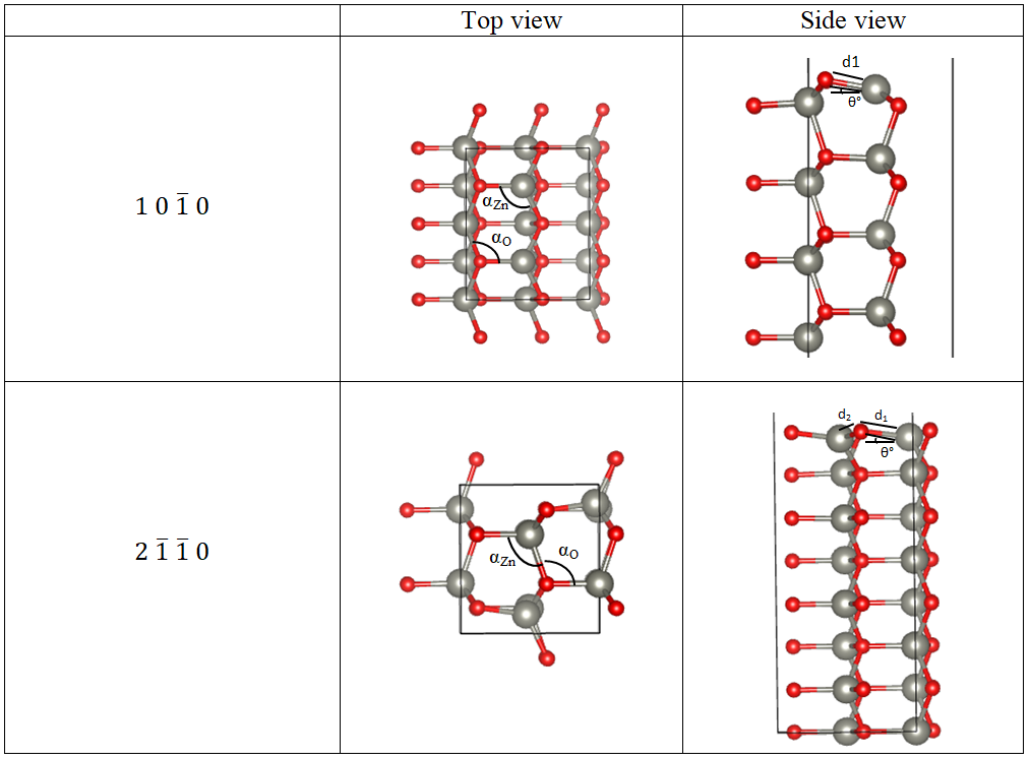

Figure 3.2 Parameters calculated for the relaxed ZnO $(1\,0\,\bar{1}\,0)$ and $(2\,\bar{1}\,\bar{1}\,0)$ surfaces showing top and side views.

	δ(Zn) Å	δ(O) Å	θ°	α_O	α_{Zn}	d_1 Å	d_2 Å
$1\,0\,\bar{1}\,0$	–0.34	0.01	10.4	103.9	118.9	1.86	–
$2\,\bar{1}\,\bar{1}\,0$	–0.22	0.03	7.8	107.3	110.7	1.88	1.89

Table 3.2 Calculated surface relaxation parameters for the ZnO (1 0 $\bar{1}$ 0) and (2 $\bar{1}$ $\bar{1}$ 0) surfaces. δ(Zn) is the vertical relaxation of surface Zn atom and δ(O) is the vertical relaxation of surface O atom.

Vibrational frequency calculations were performed to determine the Zn β-factors of (1 0 $\bar{1}$ 0) and (2 $\bar{1}$ $\bar{1}$ 0) slab surfaces (Figure 3.3). Zn β-factor is 3.99 ‰ for (1 0 $\bar{1}$ 0) and 3.94 ‰ for (2 $\bar{1}$ $\bar{1}$ 0) surface at 273 K which is very similar to the result of the bulk ZnO, except the first or two first surface layers of (2 $\bar{1}$ $\bar{1}$ 0) and (1 0 $\bar{1}$ 0) surfaces respectively. Even if the four top layers are free to move, the surface relaxation does not propagate far in the crystal structure but is restricted to the one or two topmost atomic layers. Surface Zn atoms reach a β-factor of 4.4 ‰, meaning that heavy Zn isotopes will concentrate in these topmost atomic layers. This fractionation is explained by the change of coordination from fourfold in the bulk structure to threefold at the surface. This undercoordination of Zn atoms at the surface causes the shortening of Zn-O bonds and the increase of β-factors. In figure 3.4, β-factors at 273 K are plotted as a function of the interatomic force constants for Zn atoms. β-factors increase proportionally with interatomic force constant. This relationship reflects the strong dependence of isotopic fractionation with interatomic force constants. Heavy isotopes concentrate in crystallographic sites characterized by large bond strengths (large force constants).

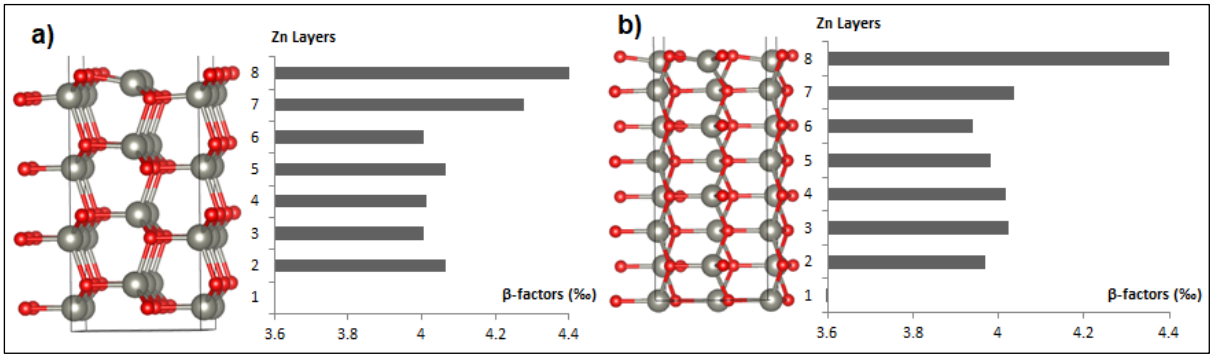

Figure 3.3 Calculated Zn β-factors (‰) at a temperature of 273 K for each atomic layer of the ZnO slabs of surface (1 0 $\bar{1}$ 0) (a), and (2 $\bar{1}$ $\bar{1}$ 0) (b). Only the 4 top Zn layers of the slabs are free to relax.

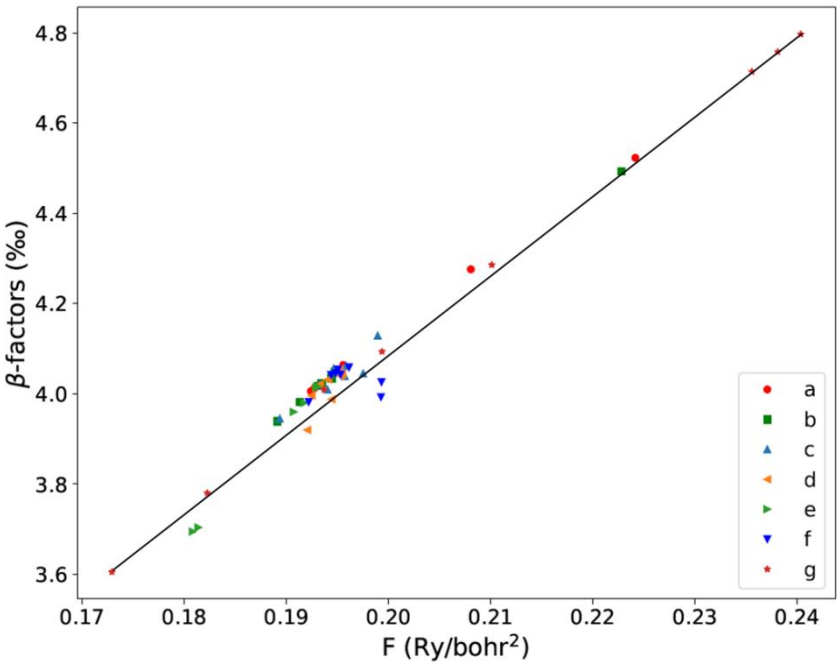

Figure 3.4 Studied β-factors (‰) at T=273 K as a function of force constants (Ry/bohr²) for ZnO slabs of surfaces (1 0 $\bar{1}$ 0) **(a)**, (2 $\bar{1}$ $\bar{1}$ 0) **(b)**, and with H_2O adsorbed on (1 0 $\bar{1}$ 0) surface in a mixed molecular and dissociative mode **(c)**, on (2 $\bar{1}$ $\bar{1}$ 0) surface: in a mixed molecular and dissociative mode **(d)**, in molecular mode **(e)**, in dissociative mode **(f)**, and for $(ZnO)_{48}$ nanoparticle **(g)**.

3.3.2.2 Adsorption of water on (1 0 $\bar{1}$ 0) and (2 $\bar{1}$ $\bar{1}$ 0) ZnO surfaces

The studied ZnO slab surfaces (1 0 $\bar{1}$ 0) and (2 $\bar{1}$ $\bar{1}$ 0) have been used to explore the interaction and the adsorption of water on these surfaces. Slabs of 12 layers (48 atoms) corresponding to the (1 0 $\bar{1}$ 0) surface and of 7-8 layers (28-32 atoms) corresponding to (2 $\bar{1}$ $\bar{1}$ 0) surface were constructed. During the calculations, the 4 central layers of the slabs were kept fixed to the bulk geometry and water was adsorbed on both sides of the slab (top and bottom). The adsorption of water on (1 0 $\bar{1}$ 0) surface has already been investigated theoretically[29,30], that's why we chose the mixed molecular and dissociated mode for this surface. Favorable results are obtained for the (1 0 $\bar{1}$ 0) surface after relaxation by employing this mixed adsorption mode. For the (2 $\bar{1}$ $\bar{1}$ 0) surface, we considered three possible modes of water adsorption (molecular, dissociative, and mixed). The mixed molecular and dissociative mode is also found to be more favorable than the molecular or the dissociative mode by 0.34 eV and 0.43 eV respectively.

The adsorption of water on the surfaces results in the decrease of the O–Zn–O angle (α_{Zn}) from to 118.9° to 109.9° and the increase of the Zn–O–Zn angle (α_O) from 103.9° to 108.3° for the surface (1 0 $\bar{1}$ 0). Through (2 $\bar{1}$ $\bar{1}$ 0) surface, the O–Zn–O angle (α_{Zn}) decreases by ~ 1.0° to become 109.9° for dissociative adsorption, and by ~ 3.0° to become 107.8° for both the molecular and the mixed adsorption. Whereas, the Zn–O–Zn angle (α_O) increases by 1.4° (108.7°) for the molecular dissociation and by 2.0° (109.3°) for both the molecular and the mixed adsorption. The Zn–O bond length elongates to become 2.01 Å for all the investigated slabs of both surfaces (1 0 $\bar{1}$ 0) and (2 $\bar{1}$ $\bar{1}$ 0).

Zn β-factors and force constant were obtained from vibrational frequency calculations, (Figure 3.5). The adsorption of water allows the complete coordination of surface Zn atoms and thus the coordination number is 4 along all the Zn atoms of the slabs. Zn surface atoms, which exhibited a large β-factor before water adsorption (Figure 3.3) now display a β-factor of around 4.0 ‰; similar to the signature of bulk Zn atoms. However we observe one exception for the molecular adsorption of water on (2 $\bar{1}$ $\bar{1}$ 0) surface (Figure 3.5) where surface Zn atoms show a smaller β-factor (i.e., ~3.7 ‰). This can be explained because the oxygen attached at the surface Zn belongs to a water molecule, whereas in the dissociative case the oxygen is attached in the hydroxyl form. The adsorption of water removes the three-fold coordination effect at the surface and thus results in a similar β-factors signature along all the Zn atoms of the studied slabs.

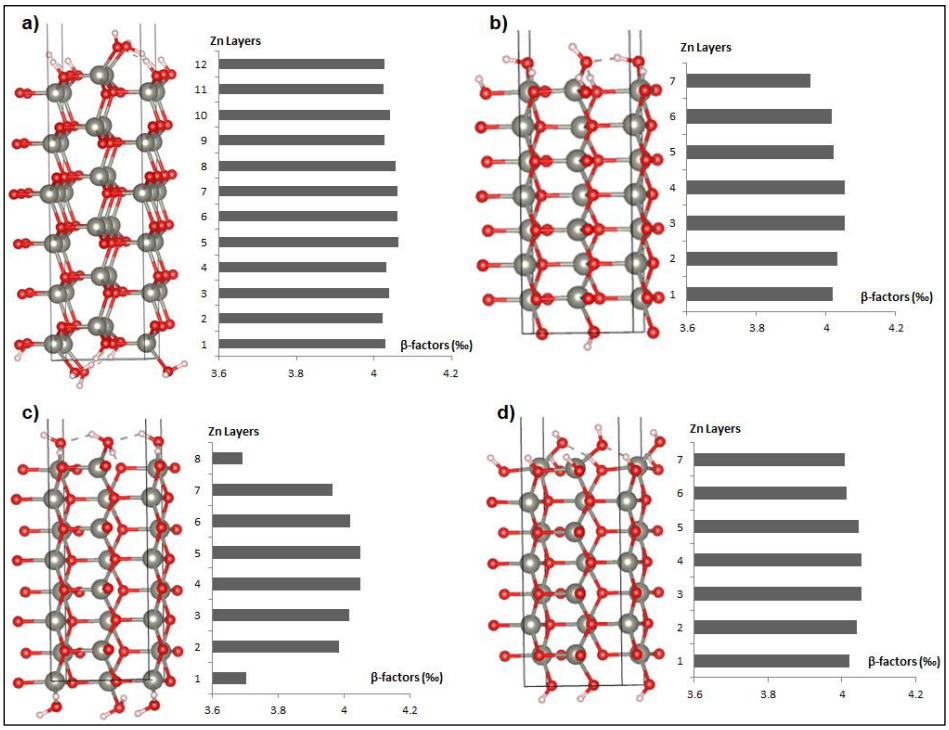

Figure 3.5 Calculated Zn β-factors (‰) for each atomic layer of ZnO slabs with H_2O adsorbed on (1 0 $\bar{1}$ 0) surface in a mixed molecular and dissociative mode (a), on (2 $\bar{1}$ $\bar{1}$ 0) surface: in a mixed molecular and dissociative mode (b), in molecular mode (c), and in dissociative mode (d).

3.3.3 ZnO nanoparticles

3.3.3.1 $(ZnO)_{48}$ nanoparticle

We start this analysis by investigating a $(ZnO)_{48}$ cluster consisting in the polar surface (0001) at the top and bottom and the apolar surface (1 0 $\bar{1}$ 0) at the latteral sides (Figure 3.6). By symmetry all the lateral surfaces are equivalent. The nanoparticle is put in an empty box such that the dimensions of the simulation cell have been defined by adding 7 Å of vacuum thickness around the $(ZnO)_{48}$ nanoparticle dimensions (15.89×15.53×17.07 $Å^3$) in each direction.

All Zn atoms in the (1 0 $\bar{1}$ 0) surfaces of the $(ZnO)_{48}$ structure are threefold coordinated except for three atoms that are fourfold coordinated. The majority of Zn atoms of the (0001) surface display in our model a twofold coordination. Thus, according to previous studies[12,31,32] and as explained in section 2., we adsorbed seven water molecules at the (0001) surface. This led to the saturation of two-coordinated surface atoms and at the same time to the minimization of the dipole along the c axis.

Zn β-factors and force constants were obtained from the vibrational frequency calculations. Figure 3.7 presents the results considering the coordination number of Zn atoms and their position in the nanoparticle (central part, edge, (0001) and $(10\bar{1}0)$ surfaces). These positions are explained in figure S3.1.

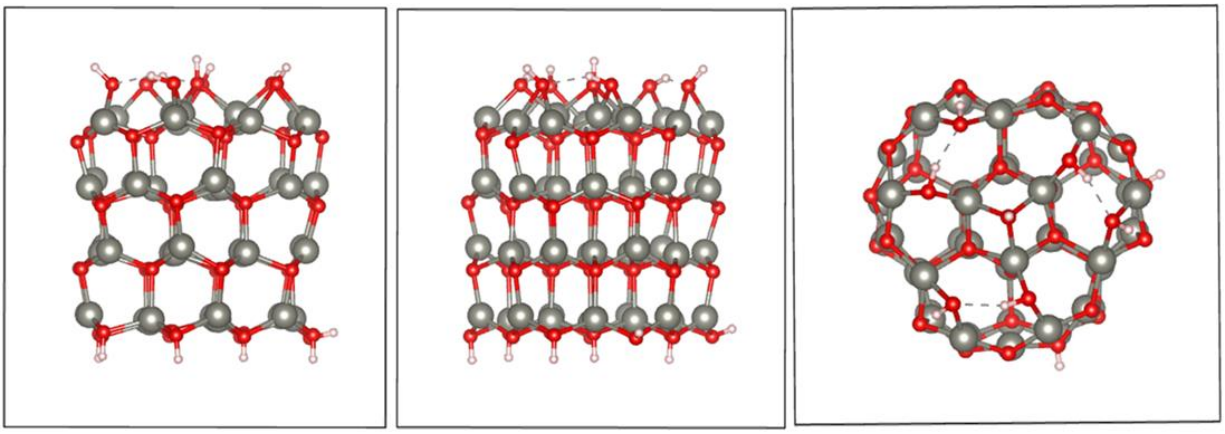

Figure 3.6. Relaxed structure of ZnO nanoparticle [$(ZnO)_{48}.7H_2O$]

The β-factors obtained for fourfold coordinated Zn atoms of the apolar surface are 4.0 ‰ and higher than the central Zn atoms by 0.3 ‰. This difference between these two values is due to some structural distortion upon optimizing this nanoparticle and could be revealed by attributing to the variation of Zn–O bond lengths depends on the position of the atom with respect to the nanoparticle. Zn atoms coordinated to three oxygen atoms and one hydroxyl of the edge has 4.0 ‰, This value increases by 0.3 ‰ when Zn coordinates more hydroxyls. β-factors for three-fold coordinated Zn are consistently higher than Zn four-fold coordinated. β-factors are 4.5 ‰ for apolar surfaces and 4.8 ‰ for edges, where Zn coordinates to 2O and 1OH for the latter part of the nanoparticle. Results of the nanoparticles here are consistent with the ones derived from the calculations done on the bulk structure and slab models, with small variations due to more important structural relaxation in the nanoparticle calculation. We have plotted the β-factors at 273 K as a function of force constants for Zn atoms of this $(ZnO)_{48}$ nanoparticle in Figure 3.4. The graph shows the same correlation between β-factors and force constants as for previous bulk and slab models. This follows the general rule of short bonds concentrating heavy isotopes.[6]

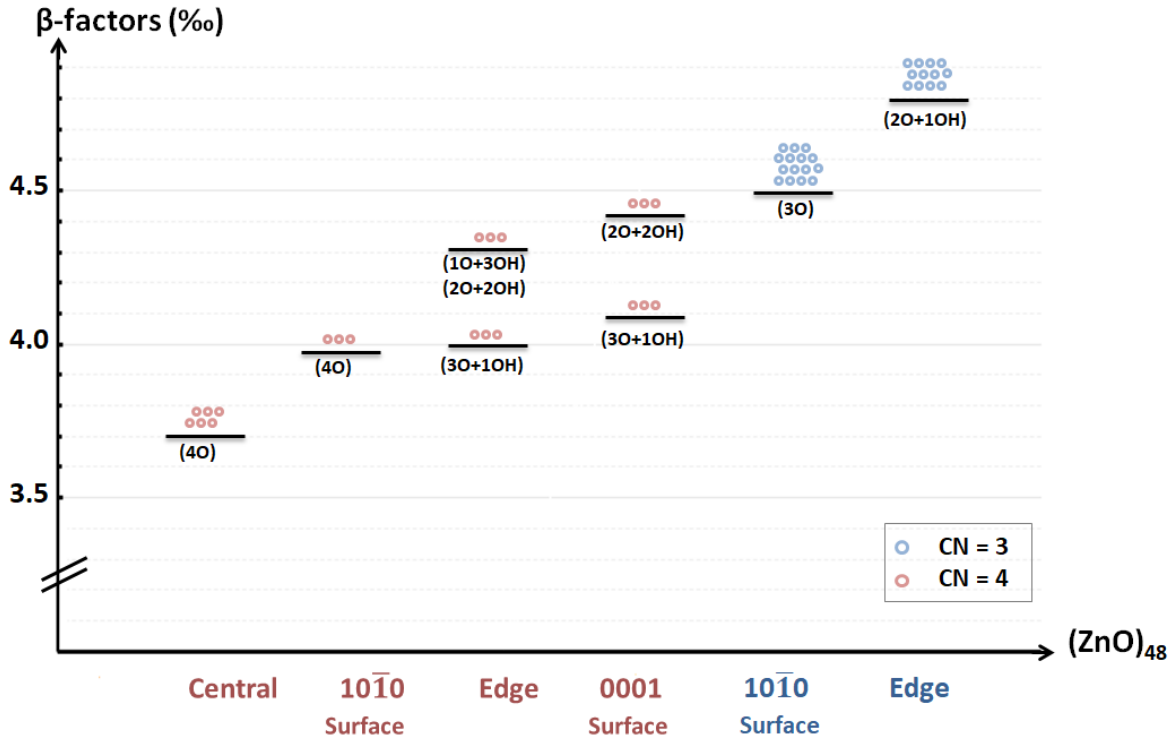

Figure 3.7. Calculated Zn β-factors (‰) for $(ZnO)_{48}$ nanoparticle as a function of the position of Zn atoms. Zn atoms are four-fold coordinated (red) and three-fold coordinated (blue). Small balls represent the number of Zn atoms in each category.

3.3.3.2 $(ZnO)_{111}$ nanoparticle

Keeping the same shape as for the $(ZnO)_{48}$ nanoparticle, we consdered a bigger $(ZnO)_{111}$ nanoparticle with water molecules adsorbed at the polar surfaces (Figure 3.8). The geometry optimization of this nanoparticle with the dimentions 21.92×20.45×24.62 $Å^3$ is performed by adding a vacuum thickness of 7 Å around the nanoparticle.

Following the same procedure as for the $(ZnO)_{48}$ nanoparticle, twelve water molecules have been adsorbed at the polar (0001) surface to saturate the Zn atoms of the $(ZnO)_{111}$ nanoparticle. After relaxation, we have six Zn atoms fourfold coordinated including one or more hydroxyls coordination. We notice for the top surface the five and six-fold coordination for seven Zn atoms. The Zn atoms in the $(1\,0\,\bar{1}\,0)$ surfaces of the $(ZnO)_{111}$ structure are distributed between thirty atoms threefold coordinated and eighteen atoms that are fourfold coordinated.

The full frequency calculation cannot be done due to the large number of atoms that makes the calculation impossible. Refering to the results of the smaller nanoparticle and following the same procedure used to explain the difference in the isotopic signatures we were able to assign a β-factor for each Zn site considering its characteristics: Zn coordination number, neighboring atoms (O or OH) and the position in the nanoparticle (central part, edge, (0001) and $(10\bar{1}0)$ surfaces). In figure 3.9, we present the β-factors of fourfold coordination for Zn atoms located at the central part by 3.7 ‰ and at the $(10\bar{1}0)$ by 4.0 ‰. The β-factors are 4.0 ‰ and 4.1 ‰ at the edge and the (0001) surface, respectively, when one hydroxyl is included in the adsorption, these two values increase by 0.3 ‰ when more hydroxyls are included. For the three coordinated Zn, β-factors mark 4.5 ‰ at apolar surfaces and 4.8 ‰ at edge. The missing β-factors for the 5- and 6-fold coordinated Zn atoms were obtained by calculating Zn force constant from finite displacement of Zn around its equilibrium position, and then using the β-factors versus force constant linear correlation of figure 3.4. We have checked this approach for several Zn sites and it gave correct results. For instance, for one Zn atom which is threefold coordinated at the $(10\bar{1}0)$ surface, the force constant is 0.230 Ry/au^2, while it is 0.237 Ry/au^2 for the smaller $(ZnO)_{48}$ nanoparticle. And for one central Zn atom four-fold

coordinated the force constant is 0.177 Ry/au^2, while it is 0.174 Ry/au^2 for the smaller nanoparticle. Thus, for the five- and six-fold coordinated Zn atoms that are not present in the small nanoparticle, the average force constant are found to be equal to 0.17 Ry/bohr^2 and 0.14 Ry/bohr^2 respectively. According to the linear correlation of figure 3.4, we get the β-factors of 3.6 ‰ and 3.0 ‰ for the 5- and 6-coordinated Zn respectively. The large coordination number of Zn atoms results in weaker Zn-O bonds leading to smaller β-factors. The global β-factors $(ZnO)_{111}$ nanoparticle is 4.16 ‰ smaller than the $(ZnO)_{48}$ nanoparticle by 0.2 ‰.

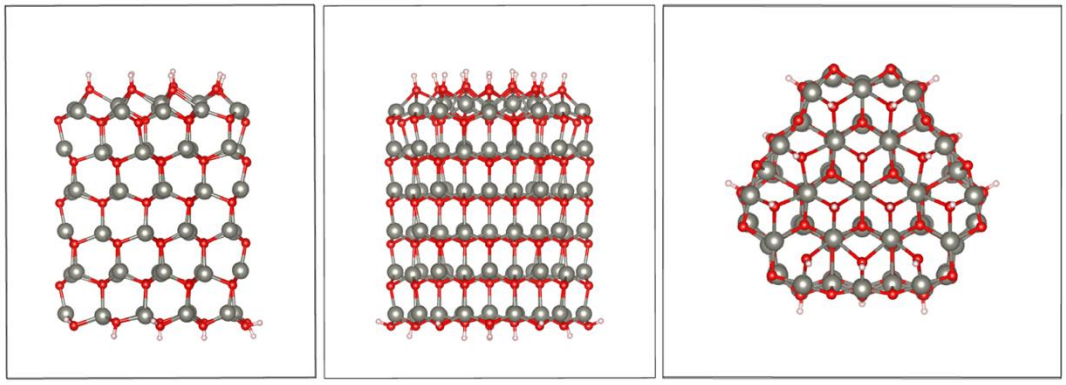

Figure 3.8. Relaxed structure of ZnO nanoparticle [$(ZnO)_{111}.12H_2O$].

Figure 3.9 Calculated Zn β-factors (‰) for $(ZnO)_{111}$ nanoparticle as a function of the position of Zn atoms. Zn atoms are six-fold coordinated (orange), five-fold coordinated

(green), four-fold coordinated (red), and three-fold coordinated (blue). Small balls represent the number of Zn atoms in each category.

3.4 Conclusion

Zn β-factors are mainly controlled by Zn coordination number, Zn-O bond lengths and the O charge. The structural relaxation occurring at the surface of ZnO nanoparticles and during the adsorption of water will thus lead to changes of the local atomic β-factors. The present study indeed shows significant variations in the β-factors of Zn atoms. The slab models under vacuum indicate that the first Zn layer of (1 0 $\bar{1}$ 0) and (2 $\bar{1}$ $\bar{1}$ 0) surfaces will be enriched in heavy Zn isotopes with a fractionation of +0.4 ‰ at 273 K relative to the bulk structure. However, the adsorption of water on the same surfaces will erase this effect by increasing Zn coordination number from 3 to 4. However, some cases of molecular water adsorption or increase of the coordination number above 4 will lead to 0.3-0.7 ‰ smaller β-factors. Our modeling of a ZnO nanoparticle suggests that this surface effect can impact the global isotopic signature of the smallest nanoparticle. In ZnO zincite structure, the surface relaxation affects only the first two atomic layers, does not propagate far in the structure, limiting the surface effect on the isotopic signature. We can expect to find stronger surface effects in materials displaying strong surface relaxation, with chemical elements associated with large isotopic variations, and with possibly redox processes mediated by the nanoparticle surfaces.

References

[1] A. S. Pereira, T. Trindade, Chapter 9 Nano dimensional ZnO: new chemical insights from an old material. PJ Thomas, P O´Brien (Eds.) Nanoscience, vol. 2. Royal Society of Chemistry; London, **2014**, 2, 255–285.

[2] A. Sirelkhatim, S. Mahmud, A. Seeni, N. H. M. Kau, L. C. Ann, S. K. M. Bakhori, et al., Review on zinc oxide nanoparticles: antibacterial activity and toxicity mechanism. Nano-Micro Letters, **2015**, 7, 219–242.

[3] A. Kołodziejczak-Radzimska , T. Jesionowski, Zinc oxide from synthesis to application: a review materials, **2014**, 7, 2833.

[4] N. Bala, S. Saha, M. Chakraborty, M, Maiti, S. Das, R. Basu, et al., Green synthesis of zinc oxide nanoparticles using Hibiscus subdariffa leaf extract: effect of temperature on

synthesis, anti-bacterial activity and anti-diabetic activity, RSC Advances. **2015**, 5, 4993–5003.

[5] G. Sangeetha, S. Rajeshwari, R. Venckatesh, Green synthesis of zinc oxide nanoparticles by Aloe barbadensis miller leaf extract: structure and optical properties, Materials Research Bulletin, **2011**, 46, 2560–2566.

[6] G. Bystrzejewska-Piotrowska, J. Golimowski, P. L. Urban, Nanoparticles: their potential toxicity, waste and environmental management, Waste Management, **2009**, 29, 2587– 2595.

[7] G. E. Batley, J. K. Kirby, M. J. McLaughlin, Fate and risks of nanomaterials in aquatic and terrestrial environments, Accounts of Chemical Research, **2013**, 46, 854–862.

[8] M. A. Maurer-Jones, I. L. Gunsolus, C. J. Murphy, C. L. Haynes, Toxicity of engineered nanoparticles in the environment, Analytical Chemistry, **2013**, 85, 3036–3049.

[9] M. M. N. Yung, C. Mouneyrac , K. M. Y. Leung, Ecotoxicity of zinc oxide nanoparticles in the marine environment. In: Bhushan B, editor, Encyclopedia of Nanotechnology, Dordrecht: Springer Netherlands, **2014**, 1–17.

[10] L. Liu, X. Wang, X. Yang, W. Fan, X. Wang, N. Wang, et al., Preparation, characterization, and biotoxicity of nanosized doped ZnO photocatalyst, International Journal of Photoenergy, **2014**, 2014, 8.

[11] K. Akhil, P. Chandran, S. Sudheer Khan, Influence of humic acid on the stability and bacterial toxicity of zinc oxide nanoparticles in water, Journal of Photochemistry and Photobiology B: Biology. **2015**, 153, 289–295.

[12] P. Giannozzi et al., 2009. Quantum Espresso: a modular and open-source software project for quantum simulations of materials, J. Phys. Condens. Matter 21, 395502.

[13] J. P. Perdew, K. Burke, M. Ernzerhof, 1996. Generalized gradient approximation made

simple. Phys. Rev. Lett. 77, 3865–3868.

[14] K. Garrity, J. Bennett, K. Rabe, D. Vanderbilt, Pseudopotentials for high-throughput DFT calculations, Comput. Mater. Sci., **2014**, 81, 446–452.

[15] B. Meyer, First-principles study of the polar O-terminated ZnO surface in thermodynamic equilibrium with oxygen and hydrogen, Phys. Rev, **2004**, 69, 045416.

[16] C. Li, W. Guo, Y. Kong, H. Gao, First-principles study on ZnO nanoclusters with hexagonal prism structures, Appl. Phys. Lett., **2007**, 90, 223102.

[17] A. Wander, N. M. J. Harrison, The stability of polar oxide surfaces: The interaction of H_2O with ZnO(0001) and ZnO(000$\bar{1}$), Chem. Phys., **2001**, 115, 2312.

[18] J. Bigeleisen, M.G. Mayer, Calculation of equilibrium constants for isotopic exchange reactions, J. Chem. Phys., 1947, 15 (5), 261–267.

[19] M. Blanchard, E. Balan, E. Schauble, Equilibrium fractionation of non traditional isotopes: a molecular modeling perspective. Rev., Mineral. Geochem., 2017, 82.

[20] U. Ozgur, Y. I. Alivov, C. Liu, A. Teke, M. A. Reshchikov, S. Dogan, V. Avrutin, S. J. Cho, H. Morkoc, A comprehensive review of ZnO materials and devices, Journal of Applied Physics, **2005**, 98, 041301.

[21] M. J.S. Spencer, K. W.J. Wong, I. Yarovsky, Density functional theory modelling of ZnO(10(1)over-bar0) and ZnO(2(1)over-bar(1)over-bar0) surfaces: Structure, properties and adsorption of N_2O, Materials Chemistry and Physics, **2010**, 119, 505–514.

[22] Kisi, E.H., Elcombe, M.M., 1989. U parameters for the wurtzite structure of ZnS and ZnO using powder neutron diffraction. Acta Crystallogr. C 45 (12), 1867–1870.

[23] M. Ducher, M. Blanchard, E. Balan, Equilibrium zinc isotope fractionation in Zn-bearing minerals from first-principles calculations, Chem. Geol., **2016**, 443, 87–96.

[24] Bachmann, M., Czerner, M., Edalati-Boostan, S., Heiliger, C., 2012. Ab initio calculations of phonon transport in ZnO and ZnS. Eur. Phys. J. B 85 (5).

[25] H. Karzel,W. Potzel, M. Kofferlein,W. Schiessl, M. Steiner, U. Hiller, G.M. Kalvius, D.W. Mitchell, T.P. Das, P. Blaha, K. Schwarz, M.P. Pasternak, Lattice dynamics and hyperfine interactions in ZnO and ZnSe at high external pressures, Physical Review, **1996**, 53, 11425–11438.

[26] E. Schauble, Applying Stable Isotope Fractionation Theory to New Systems, Rev.Mineral. Geochem., **2004**, 55 (1), 65-111.

[27] N.L. Marana, V.M. Longo, E. Longo, J.B.L. Martins, J.R. Sambrano, Electronic and structural properties of the (1010) and (1120) ZnO surfaces, Journal of Physical Chemistry A, **2008**, 112, 8958–8963.

[28] C.C. Wang, G. Zhou, J. Li, B.H. Yan, W.H. Duan, Hydrogen-induced metallization of zinc oxide ($2\bar{1}\bar{1}0$) surface and nanowires: The effect of curvature, Physical Review B, **2008**, 77, 245303.

[29] C. Wöll, 2007. The chemistry and physics of zinc oxide surfaces. Progress in Surface Science, 82, 55–120.

[30] B. Meyer, D. Marx, O. Dulub, U. Diebold, M. Kunat, D. Langenberg, C. Wöll, 2004. Partial dissociation of water leads to stable superstructures on the surface of zinc oxide. Angewandte Chemie-International Edition, 43, 6642–6645.

[31] B. Meyer, D. Marx, O. Dulub, U. Diebold, M. Kunat, D. Langenberg, D. Woll, Partial Dissociation of Water Leads to Stable Superstructures on the Surface of Zinc Oxide†, Angew. Chem., Int. Ed., **2004**, 43, 6641–6645.

[32] F. De Angelis, L. Armelao, Optical properties of ZnO nanostructures: a hybrid DFT/TDDFT investigation, Phys. Chem. Chem. Phys., **2011**, 13, 467–475.

Supplementary Information

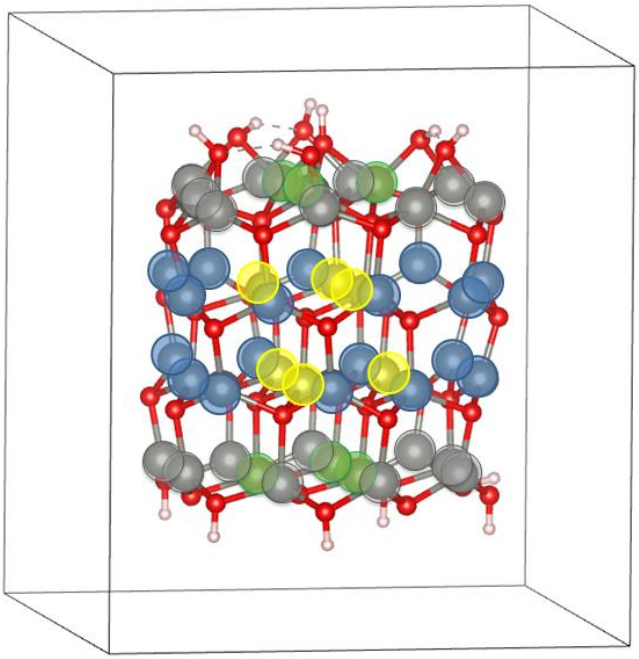

Figure S3.1 Relaxed structure of ZnO nanoparticle [$(ZnO)_{48}.7H_2O$] showing the different positions of Zn atoms in the nanoparticle: Zn at the central part (yellow), at the edge (grey), at the (0001) surface (green) and at the $(10\bar{1}0)$ surface (blue).

Chapter 4

Modelling the Interaction between Carboxylic Acids and Zinc Oxide: Insight into Degradation of ZnO Pigments

4.1 Introduction

Inorganic pigments have been used since antiquity due to their bright colors and high covering power. Together with oil binder and a variety of additives, inorganic pigments constitute the main components of oil paints. The stability of oil paints is influenced by several factors such as temperature, humidity,[1-3] exposure to light,[4] to pollutants and to solvents.[5-7] The oil binding medium, upon exposure to oxygen, first dries via radical polymerization reactions forming a cross-linked molecular network, then it ages through reactions of the autoxidation products with the pigment and eventually leads to paint degradation.[8-14] This is a serious problem for paints conservation since degradation can irreversibly change the stability and the appearance of the paint. As an example, zinc oxide (ZnO) is a typical white pigment that degrades in oil by forming metal soaps; these are in general zinc ion complexes with long-chain fatty acids which come from the aging process of the oil binding medium.[8] The consequence of the formation and aggregation of metal soaps are the appearance of small whitish lumps grown in underlying paint layer and broken through the top surface, textured surface marked with jarring spots and transparency of paint layers.[8] The entire ZnO pigment degradation process is a complex reaction pathway that has not been yet completely unravelled since its evolution is very difficult to follow and might be influenced also by external factors.[15] Recent extensive experimental studies on this topic have concluded that the degradation passes through the formation of ionomers and that the final degradation products are zinc soaps, *i.e.* zinc-carboxylate complexes.[16-19] It has been hypothesized that ZnO degradation is initialized by the interaction of ZnO pigment with the carboxylic functionalities formed by the autoxidation reactions associated to the oil

polymerization,[20] or with stearic acid, if in the paint tube formulation the jellifying agent $AlSt(OH)_2$ has been added, as experimenatlly observed in an study on the degradation of *Alchemy* by J. Pollock.[12] Zinc ions then diffuse from the pigment surface and migrate through the binding medium by 'hopping' from one carboxylate group to the neighboring one. These metal ions continue to bind many of the free carboxylic/carboxylate functionalities in the binding medium in spontaneous manner, thus giving rise to an ionomeric polymeric network.[16] This classification contributes to an understanding of the metal soap formation process. As metal ions are distributed through the binding medium in an ionomer, metal soaps could form where there are free saturated fatty acids available to form a complex.[21] Cosidering the uncertainty that still exists in the atomistic degradation mechanism of ZnO and its importance for artwork conservation it is important to clarify the different steps of ZnO degradation process to help the conservators work.

In this work we employ advanced computational modeling strategies, based on first principles electronic structure calculations, to investigate some of potential key steps of the reactive degradation process. Based on available experimental data on possible degradation pathways, a sequence of plausible intermediates and reaction pathways is calculated to estimate the reaction thermodynamics and to highlight possible mechanisms related to stability of different degradation products. We first focused on the interaction between ZnO and different oil carboxylic acids which are common degradation products and could adsorb on the ZnO surface. We associate this adsorption step to the initialization of the degradation pathway and then we characterized possible intermediates and final products. We benchmarked different models and methods to calculate the energy associated to selected reactive pathway steps, finding the adsorption of carboxylic acids to ZnO surface and the formation of Zn carboxylates to be thermodynamically favored. A role of surface acid-base chemistry in determining the energetics of ZnO degradation is finally proposed, which may be helpful to assist the pigment protection.

4.2 Models and Computational Methodologies

Starting from ZnO pigment in its wurtzite crystal structure, we build a cluster which has been already demonstrated a good model in describing the electronic and optical properties of ZnO and the adsorption of dyes through the carboxylate functionality.[22] The aim of the present chapter is to investigate (i) the interaction between ZnO and carboxylic acids and acetates,

which are plausible reactive fragments of the linseed oil degradation, and (ii) the formation of the ZnO degradation products, the Zn carboxylates. Based on the size of the investigated adsorbates and as a trade off between accuracy and computational efforts, we modelled these reactive processes by employing the acetic acid and a $(ZnO)_{42}$ cluster.[22] The $(ZnO)_{42}$ cluster model shows the wurtzite structure, and the Zn- and O- terminated surfaces have been saturated with 4 dissociated water molecules, which was previously shown to be an adequate model to study carboxylic anchoring dye groups adsorption.[22] We considered both protonated acetic acid and acetate anions to adsorb to ZnO on the apolar (1010) surface, see Figure 4.1, which are the majority surfaces exposed in ZnO, even though less reactive than the polar ones. We have chosen acetic acid and acetate since they are the smallest carboxylic acid/carboxylate models representative of longer chain acids. To evaluate how the acid chain length affects the acid-ZnO interaction and complexation we also consider hexanoic acid to carry out a comparative analysis. The calculations have been performed by Gaussian 09 program package.[24] The geometry of all the species involved in the considered reactive processes have been optimized by means of Density Functional Theory, using the B3LYP exchange–correlation functional,[24,25] a DGDZVP basis set[26,27] both in vacuo and in water solution. Solvation effects were included by means of the conductor-like polarizable continuum model (CPCM), as implemented in Gaussian09.[28] Furtherly, to simulate a low polarity environment embedding the model cluster, a CPCM model with a dielectric constant of 5 has been considered, a value included in the range of dielectric constant values measured for the linseed oil.[29] The energy associated to the investigated reactions have been computed in vacuum phase, in water and in the low polarity medium, described above. To benchmark our cluster calculations we carried out periodic ZnO slab simulations on two acetic acid adsorption modes using the CP2K-6.1 program package. The PBE exchange–correlation functional has been used in these calculations.[30,31]

4.3 Results and Discussion

4.3.1 Interaction between acetic acid/acetate and ZnO

To gain insigt in the ZnO degradation we started by investigating the adsorbtion of the acetic acid (AcH) / acetate (Ac) to the ZnO surface. The coordination of acetic acid/acetate to undercoordinated surface Zn atoms through the carboxylic oxygen atoms can be considered

as the initialization of the reaction pathway that leads to the metal soap formation.[32] The optimized structures for single and double AcH adsorption are reported in figure 4.1.

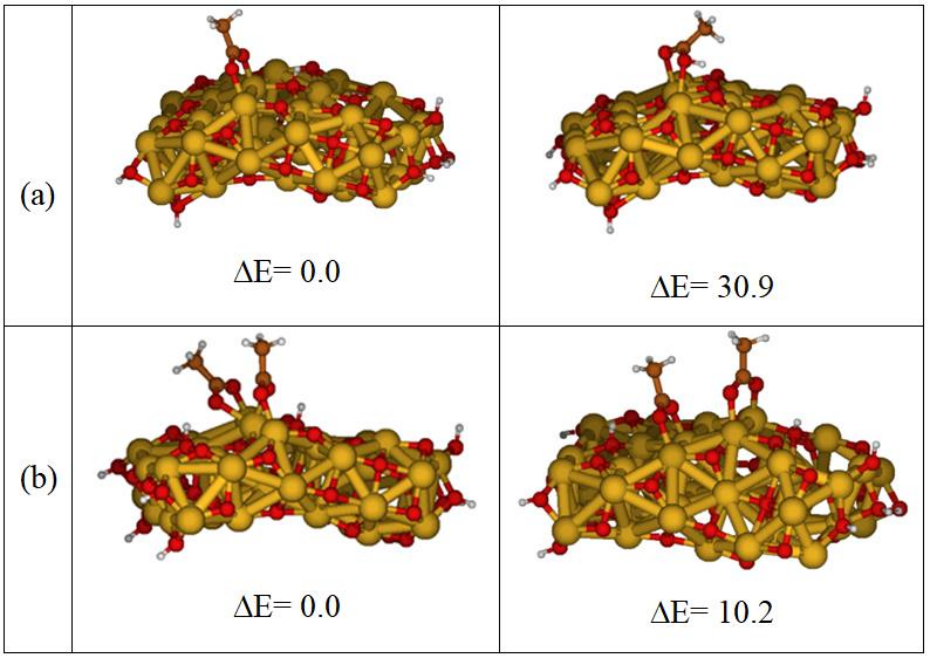

Figure 4.1 Optimized geometries of possible adsorption systems in low polarity medium, considering one acetic acid (a) or two molecules of acetic acid (b) on the surface, and the relative energy difference between the configurations in kcal/mol.

For single AcH adsorption we have explored different adsorption modes (monodentate, bidentate with the proton on the acid or transferred to the surface, dissociative bidentate) to study their corresponding stability. We focused on the geometries optimized in the low polarity medium, discussing the geometries optimized in vacuo and in water solvent when marked differences are presented. Water solvent represents a high polarity medium and stable results for the adsorption geometries optimized in it, in agreement with previous studies,[33,34] and is interesting since the humidity is one of the factors that may trigger pigment reactivity in paintings. The most stable optimized configuration shows the acetic acid adsorbed on two adjacent Zn centres by a bridged bidentate configuration transferring the proton to an oxygen of the ZnO surface, therefore in a dissociative adsorption mode, consistently with previous experimental and theoretical studies using different methodological approaches.[35-46] The monodentate and bidentate AcH adsorption modes involving the same Zn centre were found to relax to the dissociative bridged bidentate configuration. The non-dissociative bidentate adsorption is 30.9 kcal/mol higher in energy than the global dissociative minimum, figure 4.1a, indicative of the basic nature of ZnO which is prone to receive protons from carboxylic

acids. The Zn–O bond distances have been optimized ca. 2.00 and 2.02 Å for the dissociative configuration and longer, ca. 2.34 and 2.38 Å, for the not dissociative one. We optimized also another less stable bridged bidentate adsorption configuration which differs for the position of the two Zn centers involved in the adsorption, (see Figure S4.1). For the most stable adsorption configuration, the two Zn atoms bound to the carboxylic group are displaced by 18.7º and 25.1º from their initial position and are pulled out of the plane.

We further considered the adsorption of two AcH units on the ZnO surface; Figure 4.1(b) shows two optimized geometries of $(AcH)_2$@ZnO dissociative bridged bidentate modes differing for the position of the Zn centers involved in the adsorption of carboxylic acids. In the most stable configuration (Figure 4.1b, to the left) the central Zn coordinates oxygen atoms of both acids. For the most stable configuration, the Zn–O bond distances are 2.24 and 2.17 Å when the two oxygen atoms are bound to the same Zn, and 2.09 and 2.04 Å when the oxygen atoms are coordinated to different Zn atoms, while for the other configuration the ZnO distances are 2.09, 2.08, 2.05 Å. The higher stability of adsorption mode suggests that the adsorption of two carboxylic acids on the same Zn ion is favored, a fact which could have implications for the subsequent reactivity of adsorbed species, as discussed below.

We repeated the geometry optimizations for the acetate species (Ac^-), considering the following adsorption systems: $[Ac@ZnO]^-$ and $[Ac_2@ZnO]^{2-}$ in both configurations. $[Ac@ZnO]^-$ shows the same bidentate configuration found for the acid, see Figure S4.2, while for $[Ac_2@ZnO]^{2-}$ system, in the geometry optimized in solution one Zn–O bond has been detached from the surface, see Supporting Information, Figure S4.2. The computed Zn–O bond distances are 2.02, 2.8, 2.09 Å for this configuration and 2.08, 2.09, 2.10 Å for the other configuration. We therefore observe that for the charged $[Ac_2@ZnO]^{2-}$ embedded in both solvents of different polarity the most stable configuration is that with the two coordinated acetate unites on different Zn couples.

We focus on the energetics associated to the binding of one and two molecules of acetic acid/acetate to the ZnO surface, which gives indications on the occurrence of these processes. They lead to the most stable AcH@ZnO and $[Ac@ZnO]^-$ (reactions 1 and 2), and $(Ac)_2$@ZnO and $[Ac_2@ZnO]^{2-}$ (reactions 3 and 4).

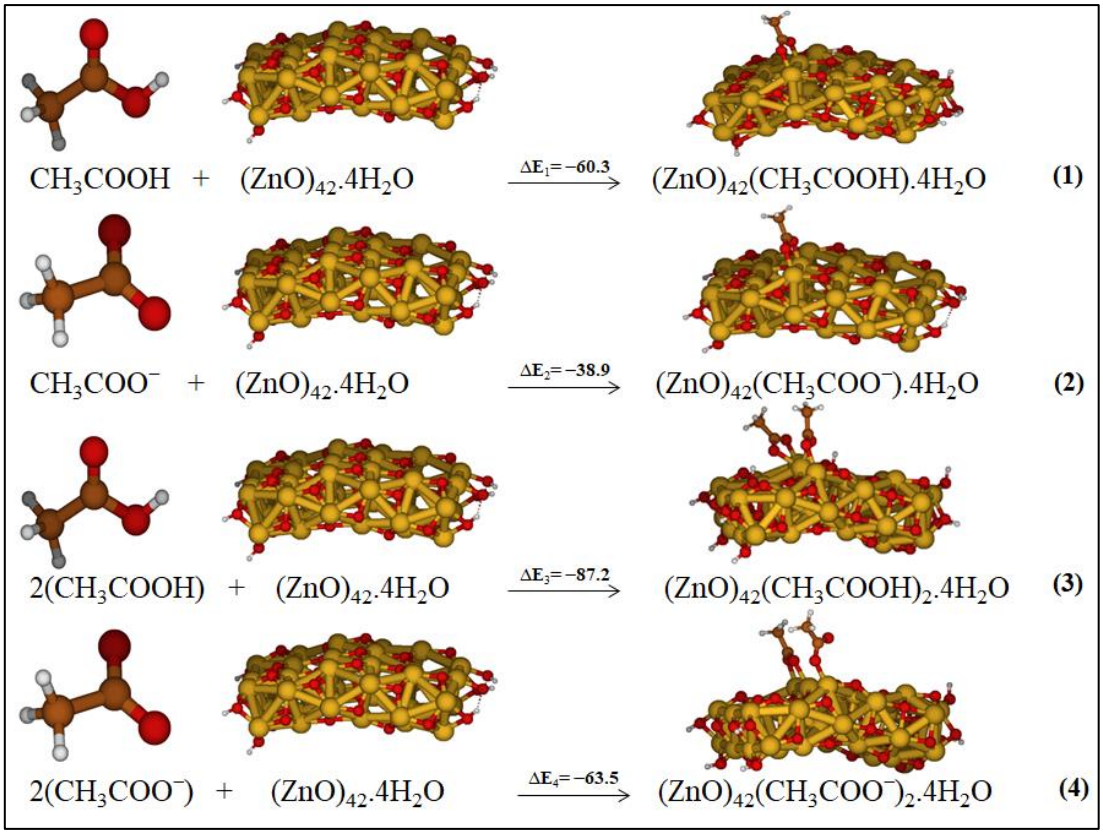

Figure 4.2 Investigated reactions considering the most stable adsorption systems as products in low polarity medium. The relative energies are reported in kcal/mol.

The reactions 1-4 are exothermic proving that the acetic acid and acetate, depending on the environmental conditions, chemical adsorb on the ZnO surface and that these adsorption systems might be plausible intermediate of the global reaction pathways of the degradation. We observe that by increasing the polarity of the medium the adsorption process is less exothermic (see SI, Table S4.1), the values in vacuo are overestimated not describing realistic conditions. Moreover, by comparing the ΔE of the reactions we found that the adsorption systems associated to acetic acid are more favoured than those adsorbing to acetate both in a low polarity medium and in water and present different adsorption geometry. The computed adsorption energy of acetic acid on ZnO surface accounts for both the proton dissociation from the acid and the adsorption of acetate and proton on the surface. The higher exothermicity of the adsorption involving acetic acid with respect to acetate is therefore the result between the energy of the proton dissociation (weakly endothermic step) and that of the proton adsorption (highly exothermic step). Moreover, the adsorption of the proton on ZnO surface might play a role in favouring the metal migration by stabilizing the generated metal vacancy.

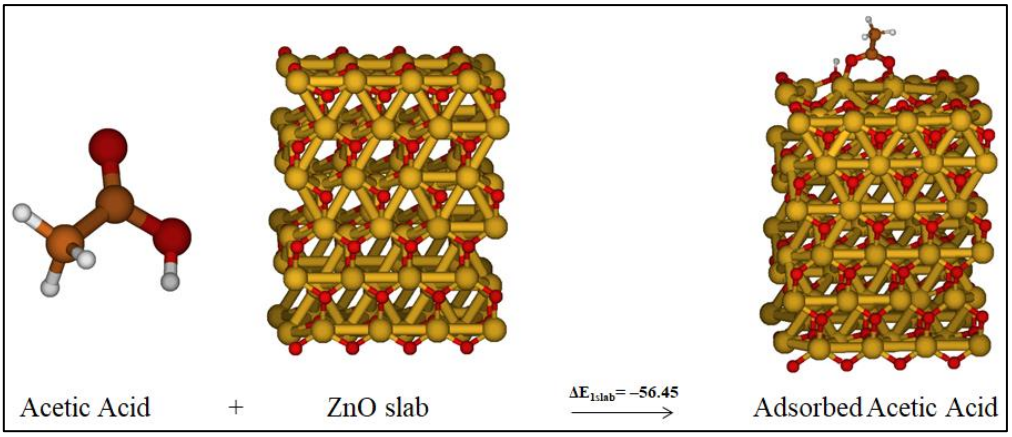

Figure 4.3. Reaction 1 considering periodic slab calculations.

To further validate our cluster approach, we consider Reaction 1, Figure 4.2, by optimizing the involved species by using a periodic slab approach, see Figure 4.3. The acetic acid is attached to ZnO surface through Zn–O bond with a distance range 1.96–2.028 Å. The obtained results are compatible with those of the cluster approach where ΔE_{1slab}= –56.5 kcal/mol thus confirming the adequacy of the model in studying this kind of reactivity pathway.

4.3.2 Zn carboxylation reactions

In explaining the degradation phenomena of ZnO pigment in oil paintings, it has been recently observed through FTIR spectroscopy that in aged oil paints the oil paint binding medium adopts an ionomer-like system when the metal ions bind to the carboxylate groups of the polymerized oil network.[6,16,47-50] A proposed degradation mechanism involves the releasing of metal ions from the pigment into the binding medium and subsequent association to carboxylate groups attached to polymer networks.[17,18] Following this hypothesis, zinc ions migrate from ZnO during paint drying and binds to the carboxylate groups,[19] the formation of zinc carboxylate complexes represent an intermediate phase during oil drying which results in the final appearance of metal soap.[13]

We focused on this degradation step, namely the formation of $Zn(AcO)_2$ from the released Zn ion from ZnO surface and the two acetate units. Starting from the same reactants, ZnO cluster and acetic acid/acetate, the products should be: (i) the ZnO cluster with a Zn-vacancy on the surface leaving it protonated indicating the transfer of protons from acetic acid or

deprotonated in combinations with the acetate or acetic acid depending in the formed Zn-complex (see Figure 4.4), and (ii) the Zn-dicarboxylate (see Figure 4.5, reactions 5 and 6).

We optimized the two ZnO clusters with a Zn vacancy and two protons on the surface, by exploring different positions of the released ion, which we indicated as Zn-1 and Zn-2, see Figure 4.4, panel (a). The corresponding optimized structures with no added protons on the surface, referring to the reaction with two acetates, are reported in Figure 4.4 panel (b). The ZnO cluster labelled Zn-1 is the most stable by 5.2 kcal/mol and 22.6 kcal/mol, respectively, see Figure 4.4.

When we consider the reaction between ZnO and four acetic acid/acetate $Zn_2(AcO)_4$ the reaction product is a ZnO cluster with two Zn-vacancies and with four protons/no protons on the ZnO surface. Following the same procedure used before, different geometries of the ZnO cluster with two Zn-vacancies on the surface have been optimized in vacuo changing the positions of Zn released atoms and the related protons (see SI, Figure S4.4). The most stable optimized structure in low polarity medium is reported in Figure 4.5 and it will be one of the products of reaction 7 (Figure 4.5). We repeated the geometry optimization of the ZnO cluster with two Zn-vacancies in different positions and no protons on the surface, to be associated to the reaction with acetate. The most stable optimized structure will be one of the products of reaction 8, see Figure 4.5.

All the investigated reaction pathways are summarized in Figure 4.5 along with the associated reaction energies, ΔE, computed in low polarity medium. The reaction energies computed in all the different considered media are reported in SI, Table S4.2.

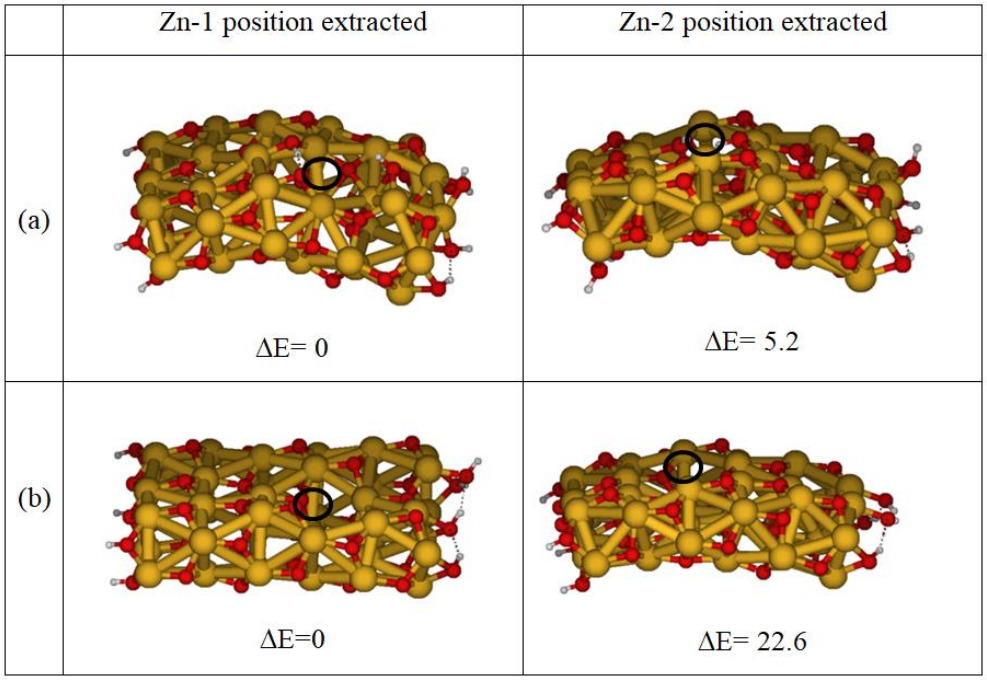

Figure 4.4 Optimized geometries of ZnO cluster by changing the position of Zn-hole on the surface leaving it protonated (a) or deprotonated (b), along with the relative energies between the configurations in kcal/mol.

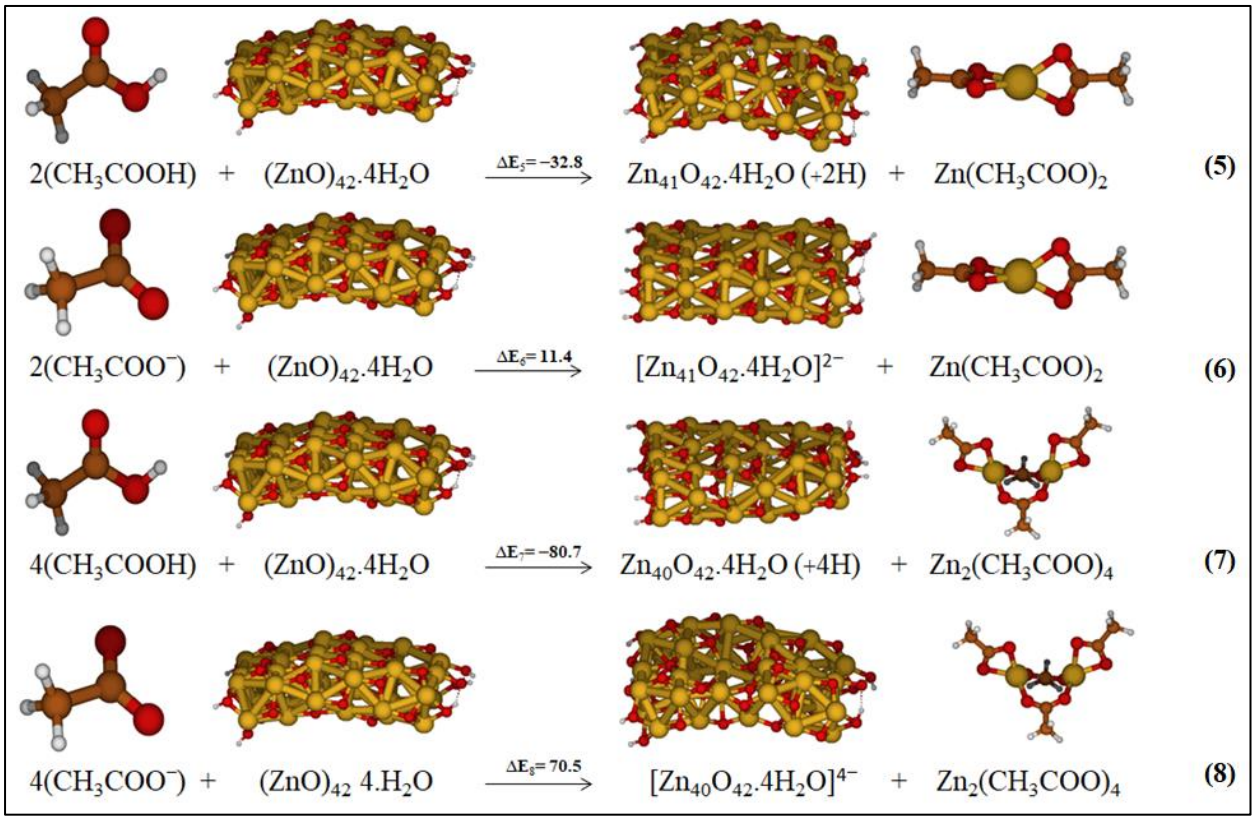

Figure 4.5 Investigated reactions considering the formation of Zn complexes as products in low polarity medium. The relative energies are reported in kcal/mol.

Reaction 5 and 7 involving acetic acids are exothermic in all the considered media, being ΔE_5= −32.8 kcal/mol and ΔE_7=−80.7 kcal/mol. On the other hand, reactive pathways 6 and 8 having the acetates as reactants are endothermic, ΔE_6=11.4 kcal/mol and ΔE_8=70.5 kcal/mol by referring to generic solution (ε=5). These values are probably overestimated due to the neglect of charge balance on the ZnO surface which on the other hand should be at least partially present in the realistic system. From our calculations, we can conclude that the reactions involving acetic acid are favoured with respect to those with acetate. In vacuo we also considered the formation of a Zn complex in which the two acetic acids coordinate to the metal not transferring the protons to the ZnO surface. This reaction in vacuo has been computed highly endothermic, essentially due to the instability of the Zn complex with respect to Zn-diacetate and further calculations in solution have not been performed (see SI. Figure S4.3).

By comparing the two studied reaction pathways, we found that the adsorption of acetic acid/acetate on the ZnO surface is thermodynamically favored over the release of Zn ions from the surface to form Zn complexes. These results are consistent with the hypothesis that the reaction pathway leading to the formation of metal soaps is initiated by the adsorption of carboxylic acid/carboxylate on the surface of ZnO cluster, see Figure 4.6. This adsorption presents a pathway from the global reaction that leads to the metal soap formation.

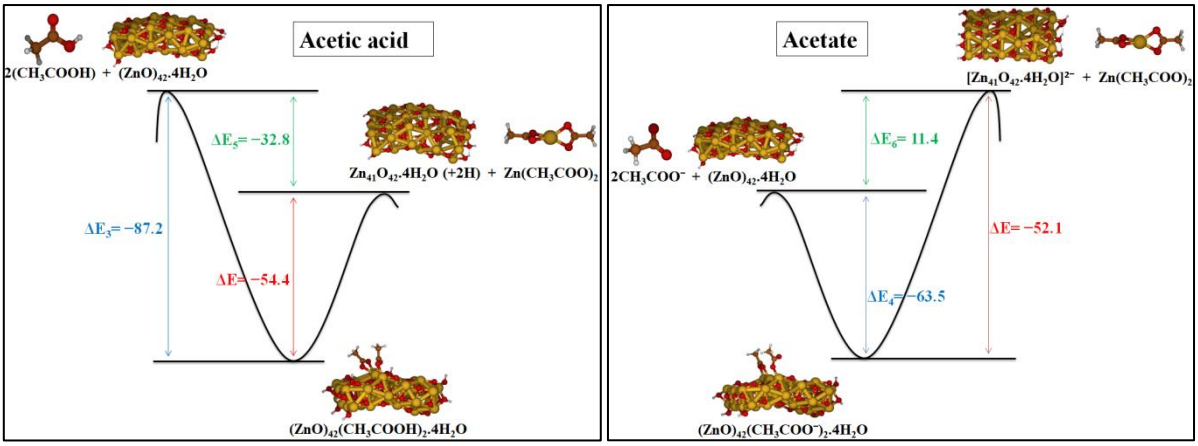

Figure 4.6 Reaction pathway of acetic acid/acetate and ZnO cluster forming metal soap and initiated by the adsorption of acetic acid/acetate on the surface of ZnO.

4.3.3 Acetic vs. hexanoic acid reactivity

Following the same strategy applied above, we have considered longer chains carboxylic acids to model the effect of the chain of the oil components in the pigment degradation. As an example, linseed oil, a widely employed medium in oil pigments, contains the α-linolenic acid, the oleic acid, the linoleic acid and small percentages of the saturated palmitic and stearic acids, of chemical formula $C_{16}H_{32}O_2$ and $C_{18}H_{36}O_2$, respectively. We limited our chains length to $C_6H_{12}O_2$ units that is a balance between a realistic saturated carboxylic acid and the size of our ZnO cluster. Starting from hexanoic acid/hexanoate and ZnO cluster as reactants, systems in which one or two molecules of hexanoate bind to the zinc of ZnO cluster through a bridged bidentate mode, with or without proton transfer, have been considered, as reported in Figure 4.7. The hexanoic acid adsorbs on two adjacent Zn centers by a bridged bidentate configuration and in a dissociative adsorption mode consistently to the acetic acid. Optimized geometry of one or two molecules of hexanoic acid chemisorbed to ZnO presents Zn–O bond distances ranging in between 2.0–2.02 Å, analogously to the adsorption of acetic acid/acetate on the ZnO cluster.

We repeat the geometry optimization also for the hexanoate species, considering one hexanoate and two molecules of hexanoate on ZnO. For the later system, the geometry has changed by going from vacuo to solution phases, in a similar way to the previous results with acetic acid, in the solvent geometries one Zn–O bond has been detached from the surface.

We focus on the reactions which lead to the most stable hexanoic acid@ZnO and hexanoate@ZnO in low polarity medium involving one molecule of hexanoic acid/ hexanoate (reactions 1’ and 2’) and two molecules of hexanoic acid/hexanoate (reactions 3’ and 4’); all these reactions are schematized in Figure 4.7 together with the related ΔE.

The reactions 1’-4’ are exothermic, we found that the adsorption systems associated to hexanoic acid are more favored than those adsorbing hexanoate which confirms the results obtained for the acetic acid. Furthermore, the energetics associated with hexanoic acid/hexanoate shows a similar trend found for acetic acid/acetate. However, the reaction energies $\Delta E_{5'}$ and $\Delta E_{7'}$ are computed larger by ca. 5 and 11 kcal/mol, respectively, than ΔE_5 and ΔE_7, the analogous ones involving the acetic acid. An appreciable increase in energy going from the acetic acid to the hexanoic one, 4.5 kcal/mol, is computed also for the coordination of two acids on the same Zn center, reactions 1’ and 3’. The increase of the

exothermicity of these reactive steps with hexanoic acids is related to the increase of the electron donating capability of the longer chain. Therefore, we might conclude that the degradation is favoured by longer chains carboxylic acids, as those composing the linseed oil which is one of the widely binder used in oil paintings. The acetic acid remains however a good model to individuate the main reactive steps of the formation of Zn complexes.

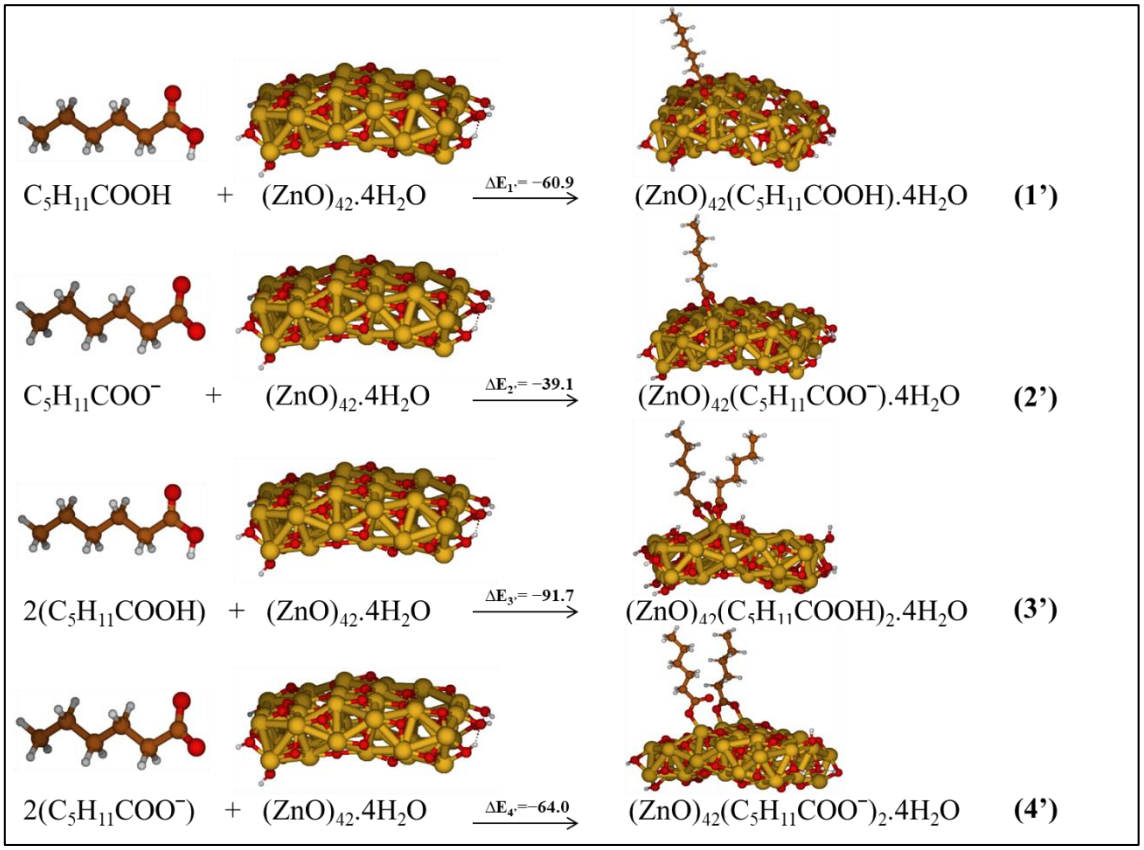

Figure 4.7 Investigated reactions considering adsorption systems as products in low polarity medium. The relative energies are reported in kcal/mol.

According to the most stable optimized systems studied in the previous part, we investigated the reactions of hexanoate Zn complexes formation which are schematized in Figure 4.8. The interaction of ZnO cluster and hexanoic acid/hexanoate, respectively reactions 5' and 6', produces: (i) the ZnO cluster with a Zn-hole on the surface leaving it protonated indicating the transfer of protons from hexanoic acid, or deprotonated in combinations with the hexanoate, and (ii) the Zn-dihexanoate. When we consider the complex of two zinc ions attached to four hexanoate as the final product of the reaction between ZnO and hexanoic acid/hexanoate, the other product of the reaction is a ZnO cluster with two Zn-holes and with four protons/no protons on the ZnO surface, reactions 7' and 8' in Figure 4.8.

The energy values are reported in the Figure 4.8 and refer to the solvent with ε=5. Reactions 5' and 7' involving two or four hexanoic acids are exothermic in all the considered media, $\Delta E_{5'}$= −38.1 kcal/mol and $\Delta E_{7'}$= −91.7 kcal/mol. On the other hand, reactive pathways 6' and 8' having the hexanoate as reactant are endothermic, $\Delta E_{7'}$=10.8 kcal/mol and $\Delta E_{8'}$= 68.8 kcal/mol by referring to generic solution. It is interesting to notice that Zn complexes involving two Zn centers are favoured with respect to Zn-dicarboxylates, consistently to the formation of Zn soaps in paintings where ZnO pigment is present.

We observe that the adsorption of hexanoic acid/hexanoate on the ZnO surface is favoured over the release of Zn ion from the surface to form Zn complexes, see Figure 4.8, in agreement with the results obtained for acetic acid. These two investigated reactions represent a simplified model of the key steps of the more complex ZnO degradation pathways.

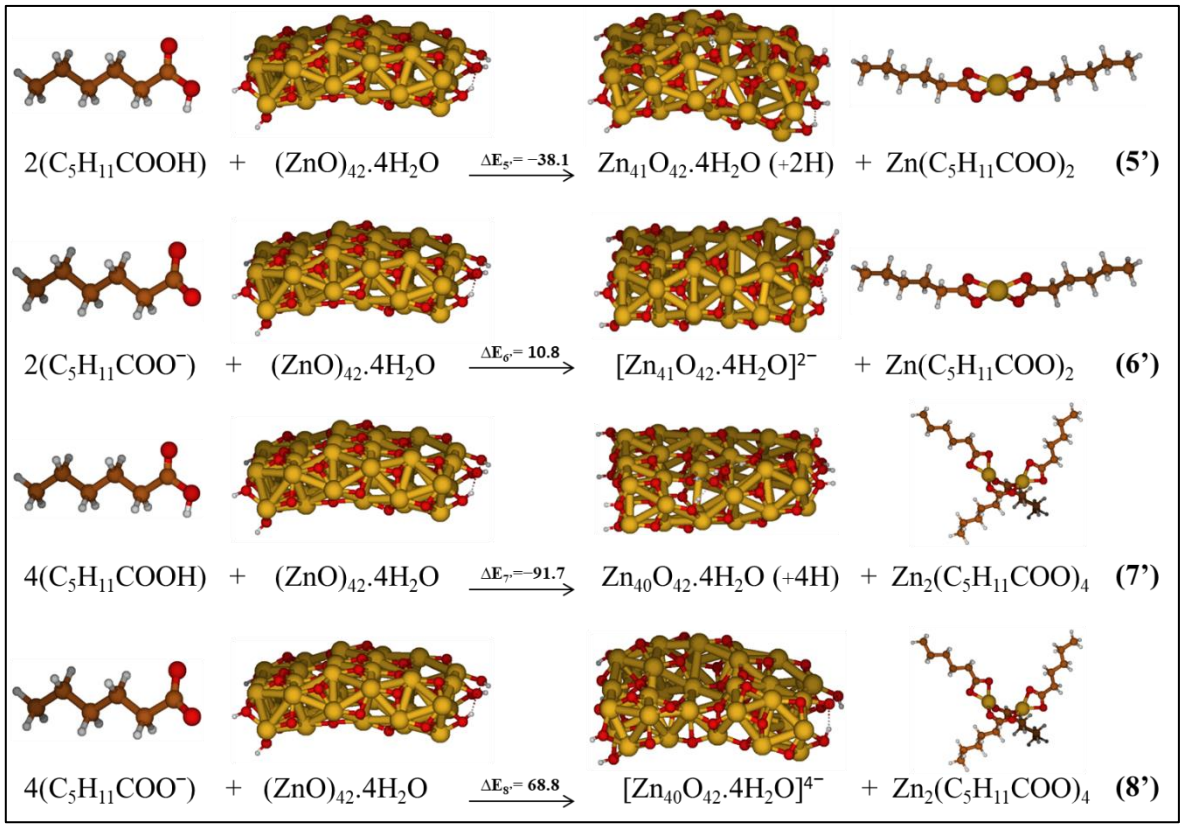

Figure 4.8 Investigated reactions considering the formation of Zn complexes as products in low polarity medium.

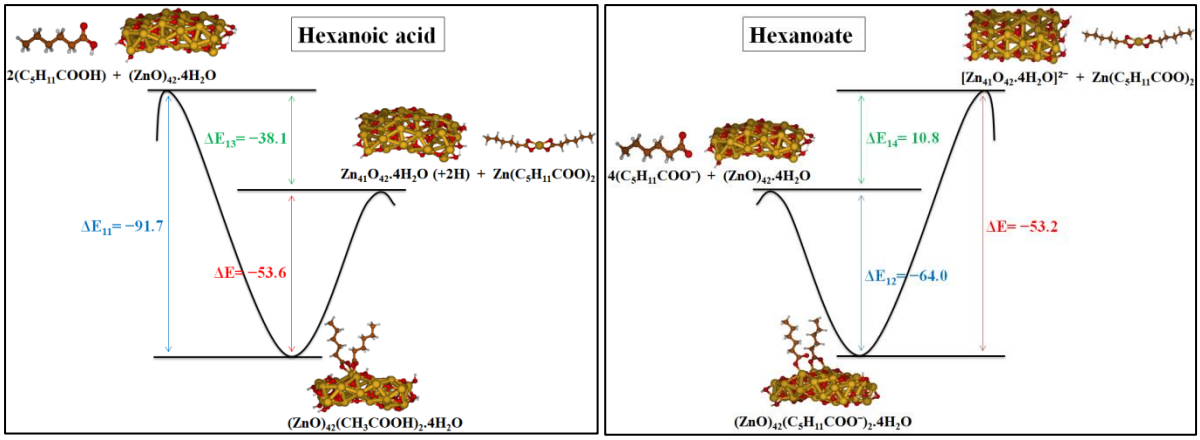

Figure 4.9 Reaction pathway of hexanoic acid/hexanoate and ZnO cluster forming metal soap and initiated by the adsorption of hexanoic acid/hexanoate on the surface of ZnO.

4.4 Conclusions

Starting from small models of ZnO clusters and carboxylic acid/carboxylate, interesting results have been obtained after the optimization of different geometries using DFT method. Reactions between the ZnO cluster and the acetic acid/acetate as well as adsorption of the acid/acetate on the cluster surface have been investigated. In addition, more realistic models with more extended ZnO clusters and longer chains of carboxylic acids/carboxylate have been considered.

Thermodynamically, it is effectively favourable to extract the zinc atom from the ZnO cluster to form metal soap. This reaction pathway is initiated by the adsorption of the carboxylic acid/carboxylate on the surface of the pigment which has been more favoured.

Longer alkyl chains of carboxylic acids do not have a significant effect on the cluster by comparing the results to those of acetic acids from structural and energetic point of view. Thus, even a small model of carboxylic acid is quite good in reproducing the properties of the studied systems in which reasonable results have been obtained.

The cluster approach has been double checked using slab approach. Thus, we can explore different models using slab and periodic calculations. Also, we can study defects that could catalyze these degradation reactions.

References

[1] G. M. Foster, S. Ritchie, C. Lowe, Controlled temperature and relative humidity dynamic mechanical analysis of paint films, J. Therm.Anal.Calorim., **2003**, 73,119–126.

[2] B. Ormsby, G. Foster, T. Learner, S. Ritchie, M. Schilling, Improved controlled relative humidity dynamic mechanical analysis of artists' acrylic emulsion paints - Part II. General properties and accelerated ageing, J. Therm. Anal. Calorim., **2007**, 90, 503–508.

[3] S. Garrappa, E. Kočí, S. Švarcová, P. Bezdička, D. Hradil, Initial stages of metal soaps' formation in model paints: The role of humidity, Microchemical Journal, **2020**, 156, 104842.

[4] C. Miliani, L. Monico, M. J. Melo, S. Fantacci, E. M. Angelin, A. Romani, K. Janssens, Photochemistry of ArtistsQ Dyes and Pigments: Towards Better Understanding and Prevention of Colour Change in Works of Art, Angewandte Chemie International Edition, **2018**, 57(25), 7324-7334.

[5] G. Hedley, M. Odlyha, A. Burnstock, J. Tillinghast, C. Husband, A study of the Mechanical and Surface Properties of Oil Paint Films Treated with Organic Solvents and Water, Stud. Conserv., **1990**, 35,98–105.

[6] A. Phenix, K. Sutherland, The cleaning of paintings: effects of organic solvents on oil paint films, Stud. Conserv., 2001, 46, 47–60.

[7] L. Baij, J. Hermans, B. Ormsby, P. Noble, P. Iedema, K. Keune, A review of solvent action on oil paint, Heritage Science., **2020**, 8, 1-23.

[8] F. Casadio, K. Keune, P. Noble, A. Van Loon, E. Hendriks, S. A. Centeno, G. Osmond, Metal Soaps in Art: Conservation and Research, Springer International Publishing, **2019.**

[9] A. Burnstock, K. J. Van den Berg, Twentieth Century Oil Paint. The Interface between Science and Conservation and the Challenges for Modern Oil Paint Research. New York: Springer **2014**.

[10] G. Osmond, Zinc white: a review of zinc oxide pigment properties and implications for stability in oil-based paintings, AICCM Bulletin, **2012**, 33, 20-29.

[11] G. Osmond, J.J. Boon, L. Puskar, Metal stearate distributions in modern artists' oil paints: surface and cross-sectional investigation of reference paint films using conventional and synchrotron infrared microspectroscopy, J. Drennan, Appl. Spectrosc., **2012**, 66, 10, 1136-44.

[12] L. Baij, J. J. Hermans, K. Keune, P. Iedema, Time-Dependent ATR-FTIR Spectroscopic Studies on Fatty Acid Diffusion and the Formation ofMetal Soaps in Oil Paint Model Systems, Angew. Chem., Int. Ed., **2018**, 57, 7351–7354.

[13] F. Gabrieli, F. Rosi, A. Vichi, L. Cartechini, L. P. Buemi, S. G. Kazarian, and C. Miliani, Revealing the Nature and Distribution of Metal Carboxylates in Jackson Pollock's Alchemy (1947) by Micro-Attenuated Total Reflection FT-IR Spectroscopic Imaging, Anal. Chem., **2017**, 89, 1283−1289.

[14] T. Poli 1, O. Chiantore, E. Diana, A. Piccirillo, Drying Oil and Natural Varnishes in Paintings: A Competition in the Metal Soap Formation, Coatings, **2021**, 11, 171.

[15] A. Artesani, Zinc oxide instability in drying oil paint, Materials Chemistry and Physics., **2020**, 255, 123640.

[16] J. J. Hermans, Ph.D. thesis, Matal Soaps in Oil Point Structure, mechanisms and dynamics, University of Amsterdam, **2017**.

[17] J. J. Hermans, K .Keune,A.van Loon, P. D. Iedema, An infrared spectroscopic study of the nature of zinc carboxylates in oil paintings, J. Anal. At. Spectrom., **2015**, 30,1600–1608.

[18] J. J. Hermans, K.Keune,A.van Loon, P. D. Iedema, The crystallization of metal soaps and fatty acids in oil paint model systems, RSC Adv., **2016**, 18, 10896 –0905.

[19] J. J. Hermans, K. Keune, A. van Loon, R. W. Corkery, P. D. Iedema, Ionomer-like structure in mature oil paint binding Media, RSC Adv., **2016**, 6, 93363–93369.

[20] L. Baij, L. Chassouant, J. J. Hermans, K. Keune, P. D. Iedema, The concentration and origins of carboxylic acid groups in oil paint, RSC advances, **2019**, 9, 35559-35564.

[21] M. Beerse, K. Keune, P. Iedema, S. Woutersen, J. Hermans, Evolution of Zinc Carboxylate Species in Oil Paint Ionomers, ACS Applied Polymer Materials, **2020**, 2, 5674−5685.

[22] A. Amat, F. De Angelis, Challenges in the simulation of dye-sensitized ZnO solar cells: quantum confinement, alignment of energy levels and excited state nature at the dye/semiconductor interface, Phys. Chem. Chem. Phys., **2012**, 14, 10662–10668.

[23] M. J. Frisch, G. W. Trucks, H. B. Schlegel, G. E. Scuseria, M. A. Robb, J. R. Cheeseman, G. Scalmani, V. Barone, B. Mennucci, G. A. Petersson, H. Nakatsuji, M. Caricato, X. Li, H. P. Hratchian, A. F. Izmaylov, J. Bloino, G. Zheng, J. L. Sonnenberg, M. Hada, M. Ehara, K. Toyota, R. Fukuda, J. Hasegawa, M. Ishida, T. Nakajima, Y. Honda, O. Kitao, H. Nakai, T. Vreven, J. A. Montgomery, Jr., J. E. Peralta, F. Ogliaro, M. Bearpark, J. J. Heyd, E. Brothers, K. N. Kudin, V. N. Staroverov, R. Kobayashi, J. Normand, K. Raghavachari, A. Rendell, J. C. Burant, S. S. Iyengar, J. Tomasi, M. Cossi, N. Rega, J. M. Millam, M. Klene, J. E. Knox, J. B. Cross, V. Bakken, C. Adamo, J. Jaramillo, R. Gomperts, R. E. Stratmann, O. Yazyev, A. J. Austin, R. Cammi, C. Pomelli, J. W. Ochterski, R. L. Martin, K. Morokuma, V. G. Zakrzewski, G. A. Voth, P. Salvador, J. J. Dannenberg, S. Dapprich, A. D. Daniels, Ö. Farkas, J. B. Foresman, J. V. Ortiz, J. Cioslowski, and D. J. Fox, Gaussian 09 (Gaussian, Inc., Wallingford CT, **2009**).

[24]A. D. Becke, Density-functional thermochemistry. III. The role of exact exchange, J. Chem. Phys., **1993**, 98, 5648–5652.

[25] C. Lee, W. Yang, R. G. Parr, Development of the Colle-Salvetti correlation-energy formula into a functional of the electron density, Phys. Rev. B, **1988**, 37, 785–789.

[26] N. Godbout, D. R. Salahub, J. Andzelm, and E. Wimmer, Optimization of Gaussian-type basis sets for local spin density functional calculations. Part I. Boron through neon, optimization technique and validation, Can. J. Chem., **1992**, 70, 560-71.

[27] C. Sosa, J. Andzelm, B. C. Elkin, E. Wimmer, K. D. Dobbs, and D. A. Dixon, A local density functional study of the structure and vibrational frequencies of molecular transition-metal compounds, J. Phys. Chem., **1992**, 96, 6630-36.

[28] G. Scalmani and M. J. Frisch, Continuous surface charge polarizable continuum models of solvation. I. General formalism, J. Chem. Phys., **2010**, 132, 114110.

[29] G.A. O'hare, P.S. Hess, A.F. Kopacki, Industrial Oil and Fat Products, J. Am. Oil. Chem. Soc. **1949**, 26, 484-488.

[30] T. D. Kühne, M. Iannuzzi, M. Del Ben et al., CP2K: An electronic structure and molecular dynamics software package - Quickstep: Efficient and accurate electronic structure calculations, J. Chem. Phys., **2020**, 152, 194103; doi: 10.1063/5.0007045.

[31] J. P. Perdew, K. Burke and M Ernzerhof, Generalized Gradient Approximation Made Simple, 77 3865, Phys. Rev. Lett. **1996.**

[32] J. J. Hermans, K. Keune, A. van Loon and P. D. Iedema, F. Casadio et al. (eds.), Towards a complete molecular model for the formation of metal soaps in oil paints, Springer, **2017**.

[33] J. Hedberg, J. Henriquez, S. Baldelli, C. M. Johnson, Ch. Leygraf, Initial Atmospheric Corrosion of Zinc Exposed to Formic Acid, Investigated by in Situ Vibrational Sum Frequency Spectroscopy and Density Functional Theory Calculations, J. Phys. Chem. C, **2009**, 113, 2088–2095.

[34] A. Dominguez, S. G. Holthaus, S. Koppen, T. Frauenheim, A. L. Da Rosa, The role of water co-adsorption on the modification of ZnO nanowires using acetic acid, Phys. Chem. Chem. Phys., **2014**, 16, 8509–8514.

[35] P. Persson, L. Ojamae, Periodic Hartree–Fock study of the adsorption of formic acid on ZnO(10–10), Chemical Physics Letters, **2000**, 321, 302–308.

[36] P. Persson, S. Lunell, L. Ojamae, Quantum chemical prediction of the adsorption conformations and dynamics at HCOOH-covered ZnO(1010) surfaces, International Journal of Quantum Chemistry, **2002**, 89, 172–180.

[37] M. Y. Sengul, C. A. Randall, A. C. T. van Duin, ReaxFF Molecular Dynamics Study on the Influence of Temperature on Adsorption, Desorption, and Decomposition at the Acetic Acid/Water/ZnO($10\bar{1}0$) Interface Enabling Cold Sintering, ACS Appl. Mater. Interfaces, **2018**, 10, 37717−37724.

[38] H. Nakatsuji, M. Yoshimoto, Y. Umemura, S. Takagi, M. Hada, Theoretical Study of the Chemisorption and Surface Reaction of HCOOH on a ZnO(101h0) Surface, J. Phys. Chem., **1996**, 100, 694-700.

[39] M. Buchholz, Q. Li, H. Noei, A. Nefedov, Y. Wang, M. Muhler, K. Fink, C. Woll, The Interaction of Formic Acid with Zinc Oxide: A Combined Experimental and Theoretical Study on Single Crystal and Powder Samples, Top Catal, **2015**, 58,174–183.

[40] H. Salimi, A. A. Peyghan, M. Noei, Adsorption of Formic Acid and Formate Anion on ZnO Nanocage: A DFT Study, J. Clust. Sci., **2015**, 26, 609–621.

[41] Z. Li, H. Yuan, Y. Sun, J. Zhang, Z. Li, X. Shao, Dissociative adsorption and linear organization of formic acid on ZnO (10-10) surface, Journal of Catalysis, **2020**, 390, 109–116.

[42] M. M. Islam, B. Diawara, P. Marcus, D. Costa, Synergy between iono-covalent bonds and van der Waals interactions in SAMs formation: A first-principles study of adsorption of carboxylic acids on the Zn-ZnO(0001) surface, Catalysis Today, **2011**, 177, 39–49.

[43] M. Buchholz, Q. Li, H. Noei, A. Nefedov, Y. Wang, M. Muhler, K. Fink, C. Woll, The Interaction of Formic Acid with Zinc Oxide: A Combined Experimental and Theoretical Study on Single Crystal and Powder Samples, Top Catal, **2015**, 58, 174–183.

[44] T. Zhang, P. Wojtal, O. Rubel, I. Zhitomirsky, Density functional theory and experimental studies of caffeic acid adsorption on zinc oxide and titanium dioxide nanoparticles, RSC Adv., **2015**, 5, 106877–106885.

[45] A. Lenz, L. Selegard, F. Soderlind, A. Larsson, P. O. Holtz, K. Uvdal, L. Ojamae, P. Kall, ZnO Nanoparticles Functionalized with Organic Acids: An Experimental and Quantum-Chemical Study, J. Phys. Chem. C, **2009**, 113, 17332–17341.

[46] Z. Guo, F. Ambrosio, W. Chen, P. Gono, A. Pasquarello, Alighment of Redox Levels at Semiconductor–Water Interfaces, Chem. Mater., **2018**, 30, 1, 94–111.

[47] J. J. Hermans, L. Baij, M. Koenis, K. Keune, P. D. Iedema, S. Woutersen, 2D-IR spectroscopy for oil paint conservation: Elucidating the water-sensitive structure of zinc carboxylate clusters in ionomers, Sci. Adv., **2019**, 5, eaaw3592.

[48] J. J. Hermans, K. Keune, A. van Loon, P. D. Iedema, Toward a complete molecular model for the formation of metal soaps in oil paints, In: Met. Soaps Art, **2019**. pp. 47–67.

[49] J. J. Hermans, K. Keune, A. van Loon, R. W. Corkery, P. D. Iedema, The molecular structure of three types of long-chain zinc(II) alkanoates for the study of oil paint degradation, Polyhedron 81, **2014**, 335–340.

[50] J. Hermans, G. Osmond, A. van Loon, P. Iedema, R. Chapman, J. Drennan, K. Jack, R. Rasch, G. Morgan G, Z. Zhang, M. Monteiro, K. Keune, Electron Microscopy Imaging of Zinc Soaps Nucleation in Oil Plant, Microscopy and Microanalysis, **2018**, 24, 318–22.

Supplementary information

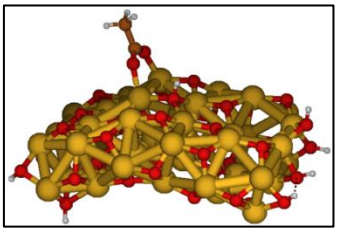

Figure S4.1 Optimized geometry of bridged bidentate adsorption configuration involving two different position of Zn centers in the adsorption.

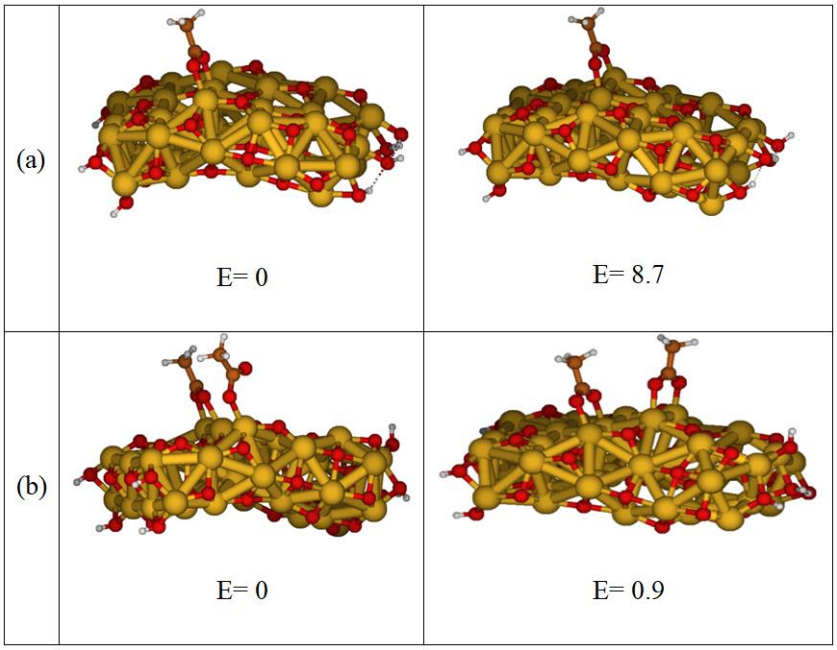

Figure S4.2 Optimized geometries of possible adsorption systems in low polarity medium, considering one acetate (a) or two acetates (b) on the surface, and the relative energy difference between the configurations in kcal/mol.

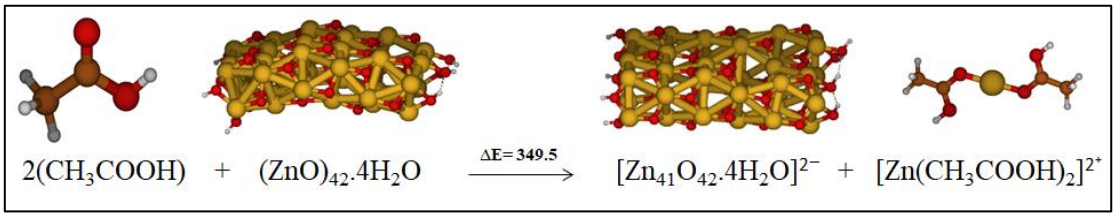

Figure S4.3 Investigated reactions in vauo considering the formation of a Zn complex with the two acetic acids coordinate to the metal and the ZnO surface deprotonated. The relative energy is reported in kcal/mol.

Zn(1-3)- extracted position	Zn(1-2)-extracted position	Zn(2-3)- extracted position
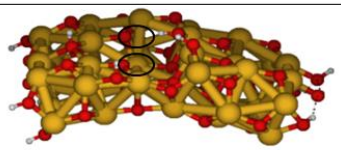	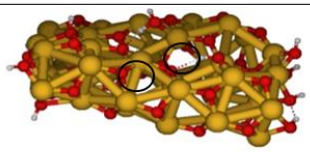	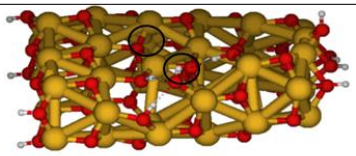
$E_{(vacuo)}$= 41.7	**$E_{(vacuo)}$=3.8**	**$E_{(vacuo)}$= 0**
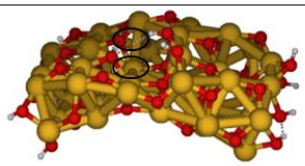	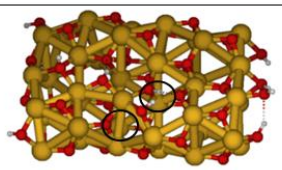	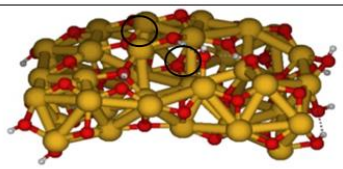
$E_{(vacuo)}$=7.5	**$E_{(vacuo)}$=34.1**	**$E_{(vacuo)}$=10.3**

Figure S4.4.a Optimized geometries of different positions for two released Zn ions from the surface of ZnO cluster leaving it protonated and the relative energy between these geometries in kcal/mol.

Zn(1-3)- extracted position	Zn(1-2)-extracted position	Zn(2-3)- extracted position
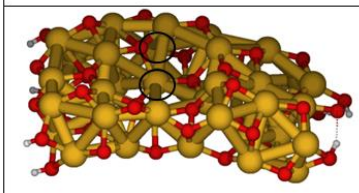	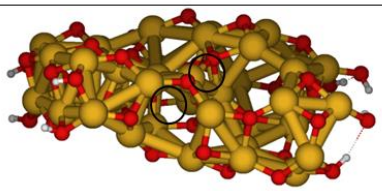	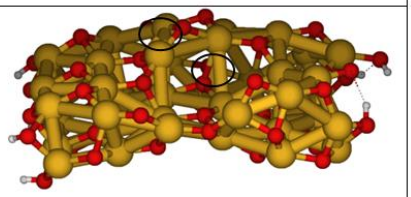
$E_{(vacuo)}= 0$	$E_{(vacuo)}=62$	$E_{(vacuo)}= 23$

Figure S4.4.b Optimized geometries of different positions for two released Zn ions from the surface of ZnO cluster leaving it deprotonated, and the relative energy between these geometries in kcal/mol.

ΔE (kcal/mol)	**VACUUM**	**ε = 5**	**WATER**
Reaction 1	−96.0	−60.3	−46.5
Reaction 2	−104.7	−38.9	−25.4
Reaction 3	−123.4	−87.2	−76.6
Reaction 4	−142.6	−63.5	−43.6

Table S4.1. Formation energies in kcal/mol for the investigated reactions reported in Figure 4.3 in vacuum and solution phases.

ΔE (kcal/mol)	**VACUUM**	**ε = 5**	**WATER**
Reaction 5	−40.2	−32.8	−29.1
Reaction 6	−38.3	11.4	27.8
Reaction 7	−95.1	−80.7	−75.1
Reaction 8	84.1	70.5	72.7

Table S4.2 Formation energies in kcal/mol for the investigated reactions corresponding to figure 4.5 in vacuum and solution phases.

ΔE (kcal/mol)	**VACUUM**	**ε = 5**	**WATER**
Reaction 1'	−97.1	−60.9	−48.6
Reaction 2'	−94.1	−39.1	−24.6
Reaction 3'	−134.0	−91.7	−69.0
Reaction 4'	−140.1	−64.0	−45.1

Table S4.3 Formation energies in kcal/mol for the investigated reactions corresponding to Figure 4.6 in vacuum and solution phases.

ΔE (kcal/mol)	**VACUUM**	**ε = 5**	**WATER**
Reaction 5'	−51.3	−38.1	−32.5
Reaction 6'	−35.5	10.8	27.0
Reaction 7'	−116.6	−91.7	−77.6
Reaction 8'	90.5	68.8	75.5

Table S4.4. Formation energies in kcal/mol for the investigated reactions corresponding to figure 4.7 in vacuum and solution phases.

Chapter 5

Modelling the Interaction between phospholipid and Metal Oxide: Insight into photocatalytic processes for virus degradation

5.1 Introduction

A photocatalyst is defined as a substance which is activated by adsorbing a photon and is capable of accelerating a reaction without being consumed.[1] In photocatalysis, reactions can take place by utilizing light and a semiconductor: in this mechanism, an electron-hole pair is generated on exposure of a semiconducting material to light, then the excited electron is used to reduce an acceptor species while the hole can simultaneously oxidize a donor species. Semiconducting oxide photocatalysts have been increasingly focused in recent years due to their potential applications in solar energy conversion and environmental purification. Heterogeneous photocatalysis have been proven to be of interest due to their efficiency in degrading recalcitrant organic compounds. Several semiconductors (TiO_2, ZnO, Fe_2O_3, CdS, ZnS) can act as photocatalysts but metal oxide semiconductors are considered to be the most suitable photocatalysts due to their photocorrosion resistance and wide band gap energies.[2] TiO_2 has been most commonly studied due to its ability to break down organic pollutants and even achieve complete mineralization. Photocatalytic and hydrophilic properties of TiO_2 makes it close to an ideal catalyst due to its high reactivity, reduced toxicity, chemical stability and low costs.[3] The applications of titania photoelectrolysis has since been greatly focused in environmental applications including water and wastewater treatment.

This study provides insight for the effects of photocatalysis to degrade coronavirus using metal oxide semiconductors TiO_2 and ZnO. The anatase form of TiO_2 exhibits exceptionally favourable photocatalytic activity. The TiO_2 displays high band gap energy (3.2 eV for

anatase) and allows the absorption of photons in the near UV range (lambda 387 nm).[4] The TiO_2 makes the photocatalytic degradation process inexpensive and facile under the solar light. The electrons of the valence band are excited under the solar light irradiation and jump into the conduction band, creating the electron-hole pairs.[5] The holes (h+) in the valence band convert the water molecules and hydroxyl groups into the hydroxyl radicals. Simultaneously, photogenerated electrons in the conduction band reduce the molecular oxygen, which is prone to interact with H_2O and forms the strong oxidizer H_2O_2. These strong oxidizers attack the organic pollutants near the photocatalysts and gradually degrade them into the harmless and non-toxic species, including CO_2 and H_2O. Figure 5.1 represents the photocatalytic degradation of organic pollutants, along with the role of the photogenerated hole and electron pairs.[5] Zinc oxide nanomaterials have shown immense potential as photocatalysts because of their high quantum efficiency, good stability, low cost, and environmentally-friendly nature.[6] The zinc oxide exhibits band gap 3.25 eV in the same range of TiO_2 and has been widely used in the photocatalytic degradation of the organic contaminants in the wastewater.[7] The photocatalytic mechanism of zinc oxide is quite similar to the TiO_2; therefore, ZnO nanomaterials have also been considered as an alternative to the titania for the detoxification of water.[8]

In this work we employ advanced computational modeling strategies, based on first principles electronic structure calculations, to investigate some of potential key steps of the reactive adsorption process. Considering the phospholipid molecule as a simplified model to approximate the virus envelope, the idea is to first study the thermodynamics of its adsorption on top of the considered metal oxide surface, and then to investigate the plausible degradation mechanisms that could be involved. In this preliminary study, we focused on the interaction between TiO_2 / ZnO and phospholipid models which assemble the environment of the coronavirus and could adsorb on the surface, employing different models and methods to calculate the energy associated to the adsorption of phospholipid at the metal oxide surface.

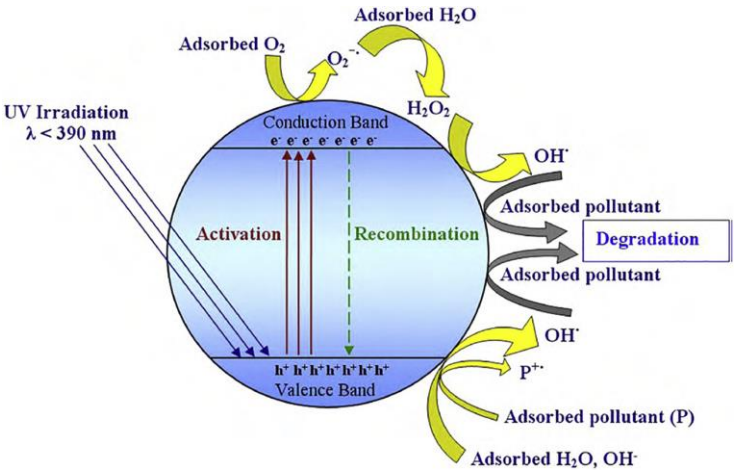

Figure 5.1. Schematic demonstration of photocatalytic reaction. The photogenerated electron-hole pairs facilitate the degradation of organic pollutants.[5]

5.2 Computational methodologies

Our aim is to investigate the interaction between phospholipid and TiO_2 or ZnO metal oxides which have proved already good photocatalytic degradation behaviour according to previous studies.[9-16] Based on the size of the investigated adsorbates and as a trade-off between accuracy and computational efforts, we modelled these reactive processes by employing phospholipid molecule and TiO_2 and ZnO slabs. We used the experimental TiO_2 cell parameters (a= 15.138 Å, b= 10.24 Å) to build our supercells, leaving 10 Å vacuum along the nonperiodic direction orthogonal to the surface direction. The model used is a 4×1×2 slab of anatase TiO_2 exposing the majority (101) surface. To carry out a comparative analysis, we modeled ZnO slab using the experimental cell parameters (a= 13.00 Å, b= 10.414 Å) to build our supercells of the $10\bar{1}0$ surface which is the majority surface exposed in ZnO, leaving 10 Å vacuum along the nonperiodic direction ($\vec{c}$). We have chosen phospholipid molecule by taking into consideration phospholipid envelop that the virus holds. The calculations have been performed by CP2K-6.1 program package.[17] The geometry of all the species involved in the considered reactive processes have been optimized by means of Density Functional Theory, using the generalized gradient approximation (GGA) employing the PBE exchange–correlation functional.[18] Van der Waals interactions were taken into account with a revised Vydrov-van Voorhis (rVV10) nonlocal density functional, with b and c parameters of 6.3 and 0.0093 respectively, employing a cutoff of 400 Ry.[19]

5.3 Results and Discussion

5.3.1 Interaction between phospholipid and metal oxide surfaces

5.3.1.1 TiO_2

We have started by optimizing a simplified model of phospholipid such that methyl groups substitute the long alkyl chains from fatty acids, which constitute the internal part of the membrane (figure 5.2). We investigated the adsorbtion of the phospholopid to TiO_2 surface. The coordination of the reduced phospholipid to undercoordinated surface titanium atoms through the oxygen atoms of the phosphate group can be considered as the most important contribution for the phospholipid adsorption. Starting from this configuration, we further optimized the adsorption of oxygen atoms from the carboxylate group to the surface. The optimized structures for different adsorption modes of Phospholipid are reported in figure 5.3. We have explored different Ti positions and adsorption modes (monodentate, bidentate) to study their corresponding stability. As expected, the most stable optimized configuration shows four coordinating oxygen atoms, two from the phosphate group (adsorbed on two adjacent Ti centres by a bridged bidentate coordination) and the other two from the carboxylate, see figure 5.3a. Such structure is stabilized by 5.0 kcal/mol compared to a structure which shows the same oxygen coordination from the phosphate group but not from the carboxylate ones, see figure 5.3b. We optimized also other less stable adsorption configurations which differ for the position of the two Ti centres involved in the adsorption (figure 5.3c and 3d right). This indicates that the most important interaction is related to the adsorbed oxygen of the phosphate group and thus making the bigger contribution to stabilize the system. The optimized structures resulted in average Ti–O bond distances of ca. 2.1 and 2.3 Å for the contribution of the phosphate oxygen atoms and longer, ca. 2.4 Å, for the carboxylate oxygen.

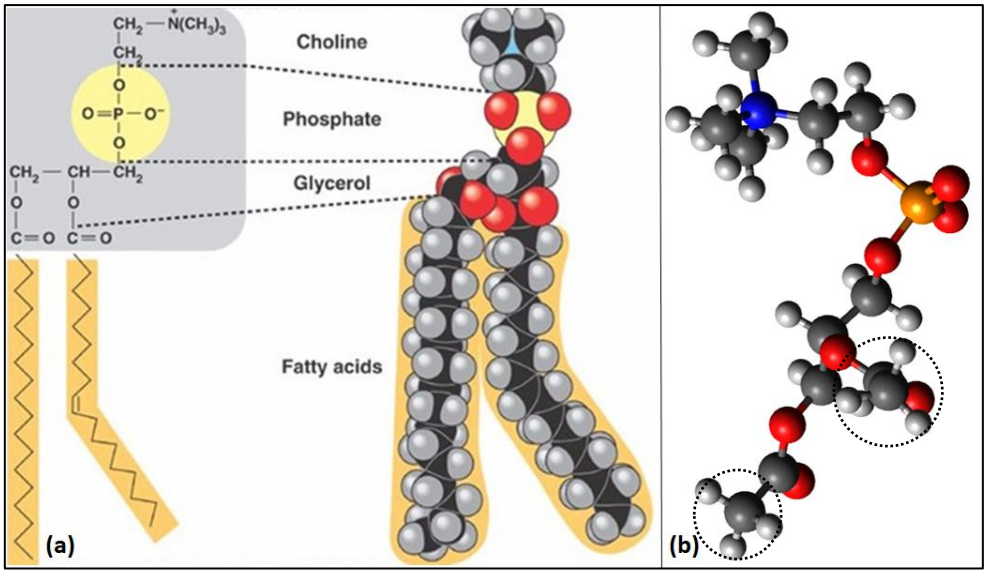

Figure 5.2. Representation of phospholipid structure (a), and the optimized phospholipid by substituting the long alkyl chains from fatty acids by methyl groups (b).

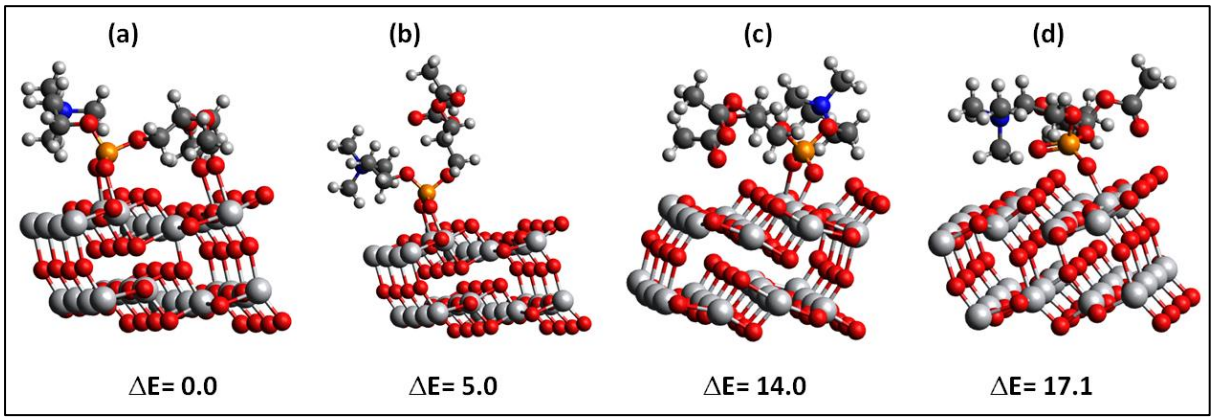

Figure 5.3. Optimized geometries of possible adsorption systems on the surface and the relative energy difference between the configurations in kcal/mol.

We focus on the energetics associated to the binding of phospholipid molecule to the TiO_2 surface, which gives indications on the occurrence of these processes. We replicate our TiO_2 model along $\vec{a}$ and $\vec{b}$ directions to have a bigger surface in order to avoid any interactions that may occur between the phospholipid molecules of different replicas and thus to simulate only the contribution of one molecule of phospholipid adsorbed on the surface. The studied reactions are exothermic proving that the phospholipid chemically adsorbs on the TiO_2 surface (figure 5.4). Moreover, by comparing the ΔE of the adsorption reactions we found that the adsorption system associated to larger surface is more favoured than the one of smaller surface by 17.6 kcal/mol presenting same adsorption geometry. This energy

difference can be explained by the interactions like steric hindrance between the phospholipid molecules of different copies that destabilize the system in the smaller oxide models. We avoid this kind of interactions by replicating the surface in a way to consider phospholipid as a real isolated molecule which results in a more stabilized adsorption system.

We further optimized the full structure of phospholipid by adding the long alkyl chains as in the 1-palmitoyl-2-oleoyl-sn-glycero-3-phosphocoline (POPC) phosphatidylcoline, which we considered as a model to describe the virus envelope. According to the most stable optimized system studied in the previous part, we investigated the reactions of the phospholipid attaching most stable adsorption sites with or without including the van der Waals forces, which can be particularly important when such long chains are involved, see figure 5.5. These forces have been considered to explore the interactions between long alkyl chains of fatty acid. We observe that the adsorption of phospholipid on the TiO_2 surface including van der Waals interaction is much more favoured, by 110.0 kcal/mol considering the same adsorption structure. The more stabilized energy indicates the important contribution of these forces on the adsorption of phospholipid to the surface. Overall, this preliminary results highlight that phospholipid molecules can be strongly adsorbed to TiO_2 surface which suggest that this material, given its well known photocatalytic properties, could be an important candidate for air purification from viruses.

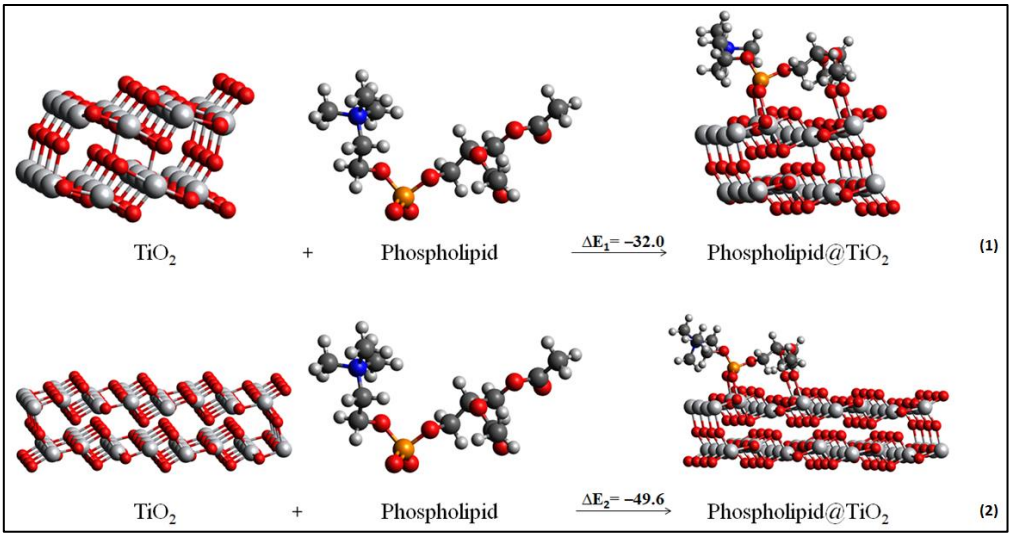

Figure 5.4. Investigated reactions considering the most stable adsorption systems as products. The relative energies are reported in kcal/mol.

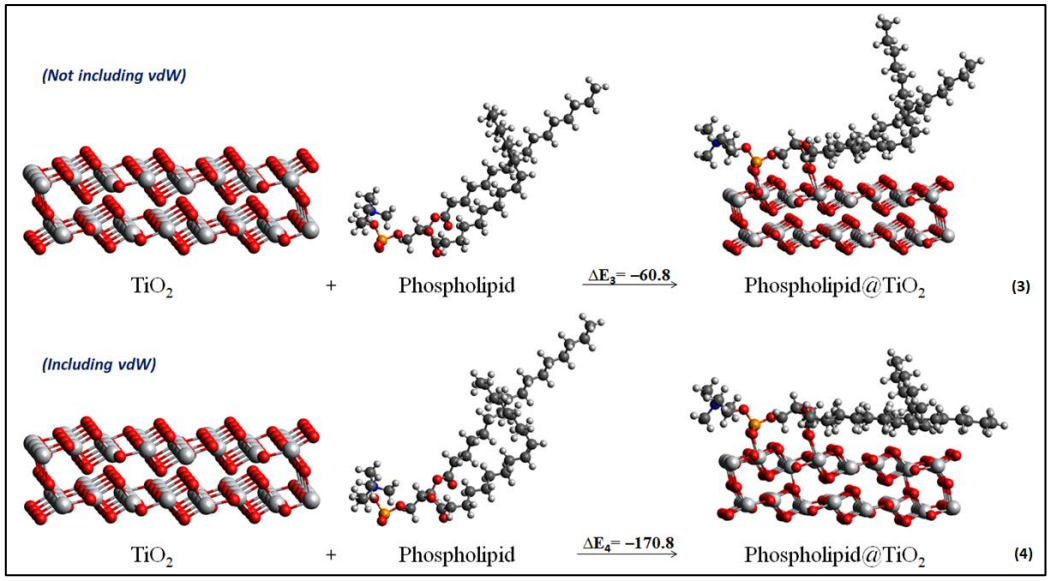

Figure 5.5. Investigated reactions considering the adsorption of phospholipid by adding the fatty acid chains. The relative energies are reported in kcal/mol.

5.3.1.2 ZnO

Following the same strategy applied above, we want to study the adsorption of phospholipid on ZnO surface to investigate its stabilty on this surface. We started from the ZnO slab modeled in the previous chapter, we cut this slab in the $\vec{c}$ direction in order to reduce the computational costs of calculations. This model is a quite good in reproducing the properties of the studied system as it shows good results and comparble to the bigger slab model. We verified whether this model can be reasonably used to evaluate the therodynamics of the adsorption reactions considering the same configuration for the simplified phospholipid molecule, which we took from the above results for TiO_2. We have also inspect the adsorbtion of the reduced phspholopid to ZnO surface. We started by optimizing the coordination of the oxygen atoms of phosphate to the undercoordinated surface zinc atoms, which is considered the most promising coordination for the phospholipid adsorption. We have also optimized the adsorption of oxygen atoms from the carboxylate group to ZnO slab. The optimized structures for different adsorption modes of Phospholipid are reported in figure 5.6. The most stable optimized configuration is obtained from coordinating two oxygen atoms from the phosphate group and two from the carboxylate group adsorbed on two adjacent Zn centres by a bridged bidentate coordination, see figure 5.6a. This system shows a slightly more favoured adsorption energy by 1.48 kcal/mol compared to the other system having the same oxygen coordination from the phosphate group but not from the carboxylate

ones, see figure 5.3b. We optimized also other less stable adsorption configuration which differs for the position of the Ti centres involved in the adsorption (figure 5.6c). The Zn–O bond distances have been optimized ca. 2.0 and 2.1 Å for the contribution of the phosphate oxygen and longer, ca. 2.3 and 2.4 Å, for the carboxylate oxygen.

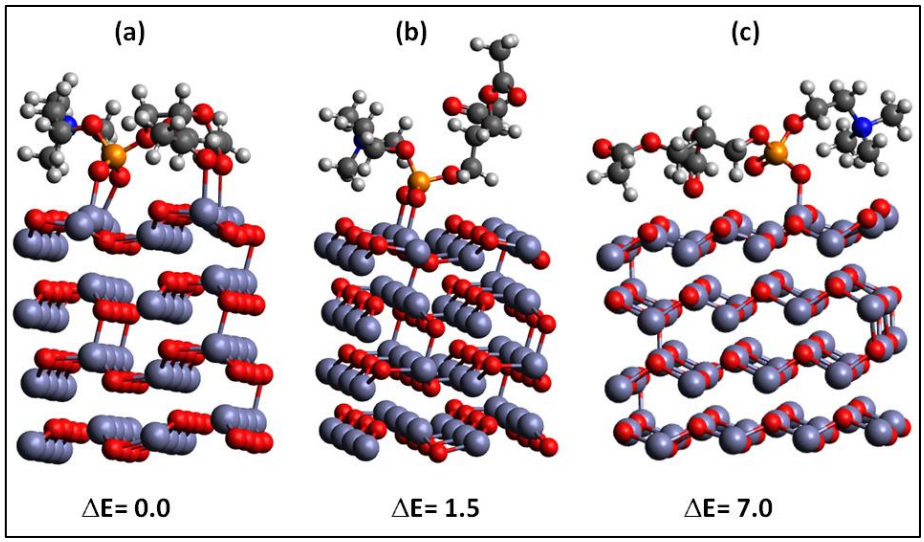

Figure 5.6. Optimized geometries of possible adsorption systems on the ZnO surface and the relative energy difference between the configurations in kcal/mol.

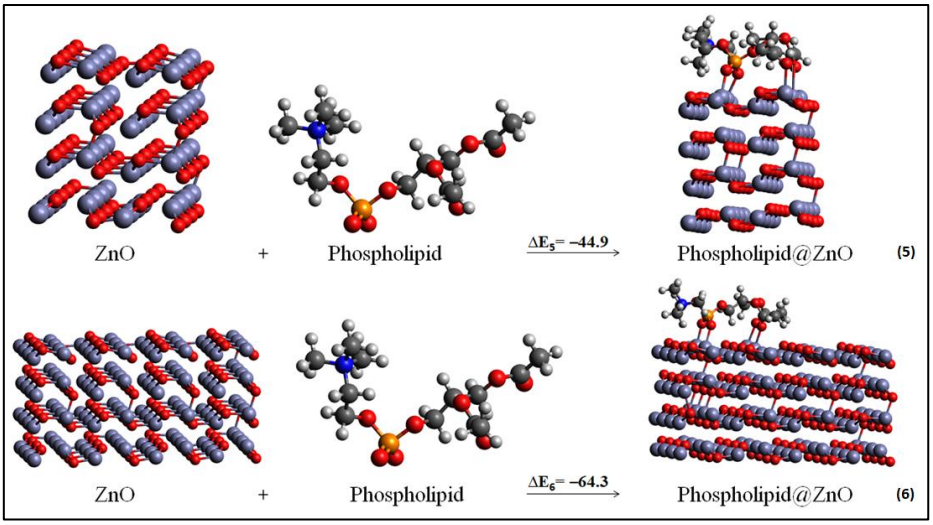

Figure 5.7. Investigated reactions considering the most stable adsorption systems as products. The relative energies are reported in kcal/mol.

We focus on the reactions which lead to the most stable adsorption, schematized in Figure 5.7 together with the related ΔE. The studied reactions are exothermic proving that the phospholipid chemical adsorbs on the ZnO surface. We enlarged the ZnO slab by replicating

it in the $\vec{b}$ direction to avoid any interactions between the phospholipid molecules. An appreciable increase in energy, 19.4 kcal/mol, is computed for the coordination of phospholipid on enlarged surface, reaction 7, showing a more favourable adsorption than the one of reactions 5.

We further considered the adsorption of the phospholipid with its fatty acids chains on the ZnO surface. Following the same trend of the TiO_2 study, we investigated the reactions of the phospholipid attaching most stable adsorption sites with or without including the van der Waals forces, see figure 5.8. The adsorption of phospholipid on the ZnO surface including van der Waals forces is found to be much more favoured by 96.9 kcal/mol over the adsorption that does not include these forces. Since its expected to have van der Waals interactions between the long alkyl chains, these interactions have important contribution on the stabilizing the adsorption of phospholipid to the surface. The increase of the exothermicity of these two reactions exhibits the increase of stability and the favoured adsorption by longer chains fatty acids.

The studied reactions of ZnO slabs manifest the higher capacity of ZnO to adsorb phospholipid comparing the results to TiO_2. ZnO is a better candidate to adsorb phospholipid and thus could be a good material also to degrade the virus of phospholipid envelop.

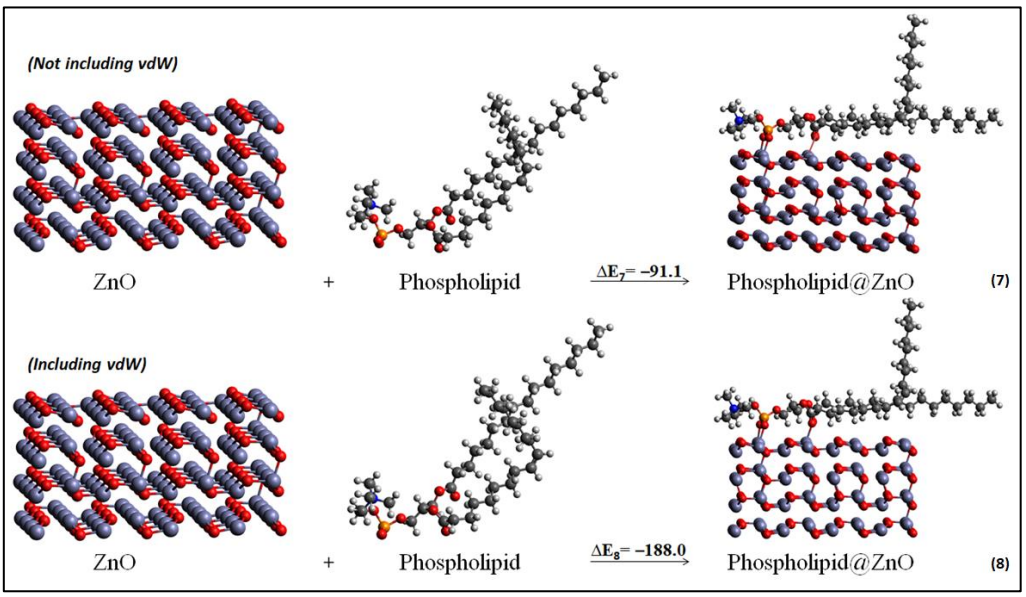

Figure 5.8. Investigated reactions considering the adsorption of phospholipid by adding the fatty acid chains. The relative energies are reported in kcal/mol.

5.4 Conclusions

This is a preliminary study for the photocatalysis of metal oxides and their ability to degrade a virus from its phospholipid envelop, which is supposed to be susceptible of degradation by the investigated metal oxides. Favourable results have been obtained after optimizing the interaction between phospholipid and TiO_2/ZnO surfaces of different geometries using DFT method. Including alkyl chains of phospholipid indicate more favoured results from energetic point of view and, particularly, the inclusion of van der Waals forces ensure the more stability of the studied systems with the fatty acid chains. Thermodynamically, reactions between the phospholipid and ZnO result in more stable adsorption systems than TiO_2 adsorption. Therefore, knowing their photocatalytic properties, TiO_2 and ZnO are both very good candidates to photodegrade the phospholipidic membrane of viruses, with the latter that is expected to adsorb phospholipids in a stronger way. However, further studies should be done to explore the photodegradation mechanisms of coronavirus using TiO_2 and ZnO as photocatalysts.

References

[1] M. Fox, Photocatalytic Oxidation of Organic Substances. In: Kluwer (ed.) Photocatalysis and Environment: Trends and Applications, New York Academic Publishers, **1988**, p. 445–467.

[2] M. A. Fox, M. T. Dulay, Heterogeneous Photocatalysis, Chemical Reviews, **1993**, 93, 341–357.

[3] A. Fujishima, T. N. Rao, D. A. Tryk, Titanium Dioxide Photocatalysis, Journal of Photochemistry and Photobiology C Photochemistry Reviews, **2000**, 1, 1-21.

[4] C. M. Teh, A.R. Mohamed, Roles of titanium dioxide and ion-doped titanium dioxide on photocatalytic degradation of organic pollutants (phenolic compounds and dyes) in aqueous solutions: a review. J Alloys Compd., **2011**, 509, 1648–60.

[5] A. R. Khataee, M. B. Kasiri, Photocatalytic degradation of organic dyes in the presence of nanostructured titanium dioxide: influence of the chemical structure of dyes, J Mol Catal A Chem **2010**, 328, 8–26.

[6] K. M. Lee, C. W. Lai, K. S. Ngai, J. C. Juan, Recent developments of zinc oxide based photocatalyst in water treatment technology: a review. Water Res., **2016**, 88, 428–48.

[7] S. Maiti, S. Pal, K. K. Chattopadhyay, Recent advances in low temperature, solution processed morphology tailored ZnO nanoarchitectures for electron emission and photocatalysis applications, Cryst. Eng. Comm., **2015**, 17, 9264–95.

[8] N. Daneshvar, D. Salari, A. Khataee, Photocatalytic degradation of azo dye acid red 14 in water on ZnO as an alternative catalyst to TiO2, J Photo. Chem. Photobiol. A Chem., **2004**, 162, 317–22.

[9] D. Chen, Y. Cheng, N. Zhou, P. Chen, Y. Wang, K. Li, S. Huo, P. Cheng, P. Peng, R. Zhang, L. Wang, H. Liu, Y. Liu, R. Ruan, Photocatalytic degradation of organic pollutants using TiO2-based

photocatalysts: A review, Journal of Cleaner Production, **2020**, 268, 121725

[10] T. Scott, H. Zhao, W. Deng, X. Feng, Y. Li, Photocatalytic degradation of phenol in water under simulated sunlight by an ultrathin MgO coated Ag/TiO2 nanocomposite, Chemosphere, **2019**, 216, 1-8.

[11] M. Zulfiqara, M. F. R. Samsudina, S. Sufiana, Modelling and optimization of photocatalytic degradation of phenol via TiO2 nanoparticles: An insight into response surface methodology and artificial neural network, Journal of Photochemistry & Photobiology A: Chemistry, **2019**, 384, 112039.

[12] M. S. F. A. Zamri and N. Sapawe, Kinetic Study on Photocatalytic Degradation of Phenol Using Green Electrosynthesized TiO2 Nanoparticles, Materials Today: Proceedings, **2019**, 19, 1261–1266.

[13] R. Gusain, K. Gupta, P. Joshi, O. P. Khatri, Adsorptive removal and photocatalytic degradation of organic pollutants using metal oxides and their composites: A comprehensive review, Advances in Colloid and Interface Science, **2019**, 272, 102009.

[14] K.M. Parida, S. Parija, Photocatalytic degradation of phenol under solar radiation using microwave irradiated zinc oxide, Solar Energy, **2006**, 80, 1048–1054.

[15] S. Chakrabarti, B. K. Dutta, Photocatalytic degradation of model textile dyes in wastewater using ZnO as semiconductor catalyst, Journal of Hazardous Materials B112, **2004**, 269–278.

[16] P. Bansal, D. Sud, Photodegradation of commercial dye, CI Reactive Blue 160 using ZnO nanopowder: Degradation pathway and identification of intermediates by GC/MS, Separation and Purification Technology, **2012**, 85, 112–119.

[17] T. D. Kühne, M. Iannuzzi, M. Del Ben et al., CP2K: An electronic structure and molecular dynamics software package - Quickstep: Efficient and accurate electronic structure calculations, J. Chem. Phys., **2020**, 152, 194103; doi: 10.1063/5.0007045.

[18] J. P. Perdew, K. Burke, M. Ernzerhof, Generalized gradient approximation made simple, Phys. Rev. Lett., **1996**, 77, 3865–3868.

[19] F. Tran, J. Hutter, Nonlocal van der Waals functionals: the case of rare-gas dimers and solids, J. Chem. Phys., **2013**, 138, 204103.

Chapter 6

Conclusions and perspectives

In this thesis we discussed the metal oxides and their engagement in the different domains. We focused our study on the environmental geochemistry, cultural heritage and photocatalytic degradation fields based on metal oxides interactions.

In environment, we focused our theoretical study on the assessment of the surface effect on the isotopic signature to identify if ZnO nanoparticles have different Zn isotope composition from bulk ZnO crystals in equilibrium conditions. ZnO bulk structure, slab surface, and nanoparticle are the three kinds of structural models which have been considered to discuss the surface effect and the isotopic properties of ZnO nanoparticles. These properties were determined from the vibrational frequencies through the determination of reduced partition function ratios (β-factors). We optimized bulk ZnO structure and we determined the equilibrium fractionation factor for this structure where Zn atoms are four-fold coordinated with O atoms. The stiffness of the interatomic bonds that controls the β-factor was evaluated by the interatomic force constant. We further investigated the $(1\,0\,\bar{1}\,0)$ and $(2\,\bar{1}\,\bar{1}\,0)$ surfaces using periodic slab models. For both models, Zn β-factors show very similar results to that of the bulk, however, surface Zn atoms mark higher β-factors due to the change of coordination from fourfold in the bulk structure to threefold at the surface. β-factors increase proportionally with interatomic force constant and thus reflects the strong dependence of isotopic fractionation with interatomic force constants. The studied ZnO slab surfaces $(1\,0\,\bar{1}\,0)$ and $(2\,\bar{1}\,\bar{1}\,0)$ have been used to explore the interaction and the adsorption of water on these surfaces. The adsorption of water removes the three-fold coordination effect at the surface and thus results in a similar β-factors signature along all the Zn atoms of the studied slabs. Moreover, we inspect the ZnO nanocluster consisting in the polar surface (0001) at the top and bottom and the apolar surface $(1\,0\,\bar{1}\,0)$ at the latteral sides. We adsorbed water molecules at the (0001) surface, as we did for slab surfaces to saturate the undercoordinate

surface atoms. Results of the nanoparticles here are consistent with the ones derived from the calculations done on the bulk structure and slab models, with small variations due to more important structural relaxation in the nanoparticle calculation. The correlation between β-factors and force constants for this nanoparticle is the same as for previous bulk and slab models. This follows the general rule of short bonds concentrating heavy isotopes. In conclusion, the structural relaxation occurring at the surface of ZnO nanoparticles and during the adsorption of water will thus lead to changes of the local atomic β-factors. The present study indeed shows significant variations in the β-factors of Zn atoms. The slab models under vacuum indicate that the first Zn layer of (1 0 $\bar{1}$ 0) and (2 $\bar{1}$ $\bar{1}$ 0) surfaces will be enriched in heavy Zn isotopes with a fractionation of +0.4 ‰ at 273 K relative to the bulk structure. However, the adsorption of water on the same surfaces will erase this effect by increasing Zn coordination number from 3 to 4. Our modelling of a ZnO nanoparticle suggests that this surface effect can impact the global isotopic signature of the smallest nanoparticle. We can expect to find stronger surface effects in materials displaying strong surface relaxation, with chemical elements associated with large isotopic variations, and with possibly redox processes mediated by the nanoparticle surfaces.

In cultural heritage field, zinc oxide has been employed as a pigment in paints that degrades in oil by forming metal soaps (zinc ion complexes with long-chain fatty acids) which come from the aging process of the oil binding medium. Our results have validated the hypothesized that ZnO degradation is initialized by the interaction of ZnO pigment with the carboxylic functionalities formed by the autoxidation reactions. We focused in clarifying the different steps of ZnO degradation process to help the conservators work. We investigated the interaction between ZnO and different oil carboxylic acids which are common degradation products which adsorb on the ZnO surface. We associate this adsorption step to the initialization of the degradation pathway and then we characterized possible intermediates and final products.We focus on the energetics associated to the binding of acetic acid/acetate to the ZnO surface, which gives indications on the occurrence of these processes. The adsorption reactions are exothermic proving that the acetic acid and acetate chemical adsorb on the ZnO surface and that these adsorption systems might be plausible intermediate of the global reaction pathways of the degradation. We further validated our cluster approach by optimizing the involved species using a periodic slab approach, The obtained results are compatible with those of the cluster approach thus confirming the adequacy of the model in studying this kind of reactivity pathway. Following the hypothesized degradation mechanism,

zinc ions migrate from ZnO during paint drying and bind to the carboxylate groups. We focused on this degradation step, namely the formation of Zn(AcO)2 from the released Zn ion from ZnO surface and the two acetate units, which represent an intermediate phase during oil drying and results in the final appearance of metal soap. By comparing the two studied reaction pathways, we found that the adsorption of acetic acid/acetate on the ZnO surface is thermodynamically favored over the release of Zn ions from the surface to form Zn complexes. These results are consistent with the hypothesis that the reaction pathway leading to the formation of metal soaps is initiated by the adsorption of carboxylic acid/carboxylate on the surface of ZnO cluster. This adsorption presents a pathway from the global reaction that leads to the metal soap formation. We evaluated how the acid chain length affects the acid-ZnO interaction and complexation by considering longer alkyl chains (hexanoic acid) to carry out a comparative analysis. The energetics associated with these reactions shows a similar trend found for acetic acid/acetate. However, the reaction energies with hexanoic acid/hexanoate are computed larger than the analogous ones involving the acetic acid. The increase of the exothermicity of these reactive steps with hexanoic acids is related to the increase of the electron donating capability of the longer chain. Therefore, we might conclude that the degradation is favoured by longer chains carboxylic acids. The acetic acid remains however a good model to individuate the main reactive steps of the formation of Zn complexes. We observe that the adsorption of hexanoic acid/hexanoate on the ZnO surface is favoured over the release of Zn ion from the surface to form Zn complexes in agreement with the results obtained for acetic acid. These two investigated reactions represent a simplified model of the key steps of the more complex ZnO degradation pathways. To conclude we could say that from small models of ZnO clusters and carboxylic acid/carboxylate, interesting results have been obtained after the optimization of different geometries using DFT method. Reactions between the ZnO cluster and the acetic acid/acetate as well as adsorption of the acid/acetate on the cluster surface have been investigated. In addition, more realistic models with more extended ZnO clusters and longer chains of carboxylic acids/carboxylate have been considered. Thermodynamically, it is effectively favourable to extract the zinc atom from the ZnO cluster to form metal soap. This reaction pathway is initiated by the adsorption of the carboxylic acid/carboxylate on the surface of the pigment which has been more favoured. Longer alkyl chains of carboxylic acids do not have a significant effect on the cluster by comparing the results to those of acetic acids from structural and energetic point of view. Thus, even a small model of carboxylic acid is quite good in reproducing the properties of the studied systems in which reasonable results have been obtained. The cluster approach

has been double checked using slab approach. Thus, we can explore different models using slab and periodic calculations. Also, we can study defects that could catalyze these degradation reactions.

In photocatalysis, reactions can take place by utilizing light and a semiconductor: in this mechanism, an electron-hole pair is generated on exposure of a semiconducting material to light, and then the excited electron is used to reduce an acceptor species while the hole can simultaneously oxidize a donor species. This work provides insight for the effects of photocatalysis to degrade coronavirus using metal oxide semiconductors TiO_2 and ZnO. In this preliminary study, we focused on the interaction between TiO_2/ZnO and phospholipid models which assemble the environment of the coronavirus and could adsorb on the surface. We optimized a simplified model of phospholipid such that methyl groups substitute the long alkyl chains from fatty acids. We investigated different adsorption modes of the phospholopid to TiO2 surface. The most stable optimized configuration shows four coordinating oxygen atoms, two from the phosphate group (adsorbed on two adjacent Ti centres by a bridged bidentate coordination) and the other two from the carboxylate group, where the most important interaction is related to the adsorbed oxygen of the phosphate group and thus making the bigger contribution to stabilize the system. The energetics associated to the binding of phospholipid molecule to the TiO_2 surface gives indications on the occurrence of these processes. We duplicate the TiO_2 surface and by comparing the ΔE of the adsorption reactions we found that the adsorption system associated to larger surface is more favoured than the one of smaller surface presenting same adsorption geometry. This energy difference can be explained by the interactions between the phospholipid molecules of different copies that destabilize the system in the smaller oxide models. We avoid this kind of interactions by replicating the surface in a way to consider phospholipid as a real isolated molecule which results in a more stabilized adsorption system. We further optimized the full structure of phospholipid by adding the long alkyl chains which we considered as a model to describe the virus envelope. We investigated the reactions of the phospholipid attaching most stable adsorption sites with or without including the van der Waals forces, which can be particularly important when such long chains are involved. We noticed the increase of stability for adsorption reactions by longer alkyl chains. As well as, the obtained results from the inclusion of these forces are much more favoured than systems not including such interactions, considering the same adsorption structure. This indicates the important contribution of these forces on the adsorption of phospholipid to the surface. These

preliminary results highlight that phospholipid molecules can be strongly adsorbed to TiO_2 surface which suggest that this material, given its well known photocatalytic properties, could be an important candidate for air purification from viruses. Following the same strategy applied TiO_2, we studied the adsorption of phospholipid on ZnO surface to investigate its stabilty on this surface. The energetics associated with the adsorption reactions for ZnO shows a similar trend found for TiO2, However ZnO shows higher capacity to adsorb phospholipid. ZnO is a better candidate to adsorb phospholipid and thus could be a good material also to degrade the virus of phospholipid envelop. To conclude, this preliminary study for the photocatalysis of metal oxides shows their ability to degrade a virus from its phospholipid envelop, which is supposed to be susceptible of degradation by the investigated metal oxides. Favourable results have been obtained after optimizing the interaction between phospholipid and TiO_2/ZnO surfaces of different geometries using DFT method. Including alkyl chains of phospholipid indicate more favoured results from energetic point of view and, particularly, the inclusion of van der Waals forces ensure the more stability of the studied systems with the fatty acid chains. Thermodynamically, reactions between the phospholipid and ZnO result in more stable adsorption systems than TiO_2 adsorption. Therefore, knowing their photocatalytic properties, TiO_2 and ZnO are both very good candidates to photodegrade the phospholipidic membrane of viruses, with the latter that is expected to adsorb phospholipids in a stronger way. However, further studies should be done to explore the photodegradation mechanisms of coronavirus using TiO_2 and ZnO as photocatalysts.

Conclusions et Perspectives (en Français)

Dans cette thèse, nous avons discuté des oxydes métalliques et de leur implication dans les différents domaines. Nous avons concentré notre étude sur les domaines de la géochimie environnementale, du patrimoine culturel, et de la dégradation photocatalytique.

Pour l'application environnementale, nous avons concentré notre étude théorique sur l'évaluation de l'effet de la surface sur la signature isotopique du zinc afin d'identifier si les nanoparticules de ZnO ont une composition isotopique de Zn différente de celle des cristaux de ZnO massifs en conditions d'équilibre thermodynamique. La structure cristalline de ZnO, la surface de « slabs » et les nanoparticules sont les trois types de modèles structuraux qui ont été considérés. Ces propriétés ont été déterminées à partir des fréquences vibrationnelles par la détermination de rapports de fonction de partitions réduites (facteurs β). Nous avons optimisé la structure de ZnO et nous avons déterminé le facteur de fractionnement à l'équilibre pour cette structure où les atomes de Zn sont coordonnés à quatre atomes d'oxygènes. La rigidité des liaisons interatomiques qui contrôlent le facteur β a été évaluée par la constante de force interatomique. Nous avons ensuite étudié les surfaces $(1\,0\,\bar{1}\,0)$ et $(2\,\bar{1}\,\bar{1}\,0)$ à l'aide de modèles de « slabs » périodiques. Pour les deux modèles, les facteurs β de Zn montrent des résultats très similaires à ceux du cristal en masse, cependant, les atomes de Zn de surface affichent des facteurs β plus élevés en raison du changement de coordination de quatre dans la structure en masse à trois à la surface. Les facteurs β augmentent proportionnellement avec la constante de force interatomique. Les surfaces de ZnO étudiées $(1\,0\,\bar{1}\,0)$ et $(2\,\bar{1}\,\bar{1}\,0)$ ont été utilisées pour explorer l'interaction et l'adsorption de l'eau. L'adsorption d'eau complète la coordination de Zn à la surface et se traduit ainsi par une signature de facteurs β similaire le long de tous les atomes de Zn des « slabs » étudiées. De plus, nous inspectons le nanocluster de ZnO constitué de la surface polaire (0001) en haut et en bas et de la surface apolaire $(1\ 0\ 1\bar{}0)$ sur les facettes latérales. Nous avons adsorbé des molécules d'eau à la surface (0001), comme nous l'avons fait pour les surfaces de « slab » pour saturer les atomes de surface sous-coordonnés. Les résultats des nanoparticules ici sont cohérents avec ceux dérivés des calculs effectués sur les modèles de structure en masse et de « slab », avec de petites variations dues à une relaxation structurale plus importante dans le calcul des nanoparticules. La corrélation entre les facteurs β et les constantes de force pour

cette nanoparticule est la même que pour les modèles précédents. Cela suit la règle générale des liaisons courtes concentrant les isotopes lourds. En conclusion, la relaxation structurale se produisant à la surface des nanoparticules de ZnO et lors de l'adsorption de l'eau conduira donc à des modifications des facteurs β atomiques locaux. Notre étude montre en effet des variations significatives des facteurs β des atomes de Zn. Les modèles de « slabs » indiquent que la première couche de Zn des surfaces $(1\,0\,\bar{1}\,0)$ et $(2\,\bar{1}\,\bar{1}\,0)$ sera enrichie en isotopes lourds de Zn avec un fractionnement de +0,4 ‰ à 273 K par rapport au centre du cristal. Cependant, l'adsorption d'eau sur les mêmes surfaces effacera cet effet en augmentant le nombre de coordination Zn de 3 à 4. Notre modélisation d'une nanoparticule de ZnO suggère que cet effet de surface peut impacter la signature isotopique globale des plus petites nanoparticules. Nous pouvons nous attendre à trouver des effets de surface plus forts dans les matériaux présentant une forte relaxation de surface, avec des éléments chimiques associés à de grandes variations isotopiques, et avec éventuellement des processus redox liés aux surfaces des nanoparticules.

Dans le domaine du patrimoine culturel, l'oxyde de zinc a été utilisé comme pigment dans les peintures qui se dégradent dans l'huile en formant des savons métalliques (complexes d'ions zinc avec des acides gras à longue chaîne) qui proviennent du processus de vieillissement du liant de l'huile. Nos résultats ont validé l'hypothèse selon laquelle la dégradation du ZnO est initialisée par l'interaction du pigment ZnO avec les fonctionnalités carboxyliques formées par les réactions d'auto-oxydation. Nous nous sommes concentrés sur la clarification des différentes étapes du processus de dégradation de ZnO. Nous avons étudié l'interaction entre ZnO et différents acides carboxyliques d'huile qui sont des produits de dégradation courants s'adsorbant à la surface du ZnO. Nous associons cette étape d'adsorption à l'initialisation de la voie de dégradation puis nous caractérisons d'éventuels intermédiaires et produits finaux. Les réactions d'adsorption sont exothermiques prouvant que l'acide acétique et l'acétate s'adsorbent sur la surface de ZnO et que ces systèmes d'adsorption pourraient être des intermédiaires plausibles des voies réactionnelles globales de la dégradation. Nous avons ensuite validé notre approche « cluster » en optimisant les espèces impliquées à l'aide d'une approche des surfaces en « slabs » périodiques. Les résultats obtenus dans les deux cas sont compatibles confirmant ainsi l'adéquation du modèle pour étudier ce type de réactivité. Suite au mécanisme de dégradation, les ions zinc migrent de ZnO pendant le séchage de la peinture et se lient aux groupes carboxylate. Nous nous sommes concentrés sur cette étape de dégradation, à savoir la formation de Zn $(AcO)_2$ à partir de l'ion Zn libéré de la surface de

ZnO et des deux unités d'acétate, qui représentent une phase intermédiaire lors du séchage de l'huile et aboutissent à l'apparition finale de savon métallique. En comparant les deux voies de réaction étudiées, nous avons constaté que l'adsorption d'acide acétique/acétate sur la surface de ZnO est thermodynamiquement favorisée par rapport à la libération d'ions Zn de la surface pour former des complexes de Zn. Ces résultats sont cohérents avec l'hypothèse selon laquelle la voie de réaction conduisant à la formation de savons métalliques est initiée par l'adsorption d'acide carboxylique/carboxylate à la surface du cluster ZnO. Cette adsorption présente un chemin réactionnel qui conduit à la formation de savon métallique. Nous avons évalué comment la longueur de la chaîne acide affecte l'interaction et la complexation acide-ZnO en considérant des chaînes alkyle plus longues (acide hexanoïque). L'énergétique associée à ces réactions montre une tendance similaire à celle de l'acide acétique/acétate. Cependant, les énergies de réaction avec l'acide hexanoïque/hexanoate sont plus grandes que celles impliquant l'acide acétique. L'augmentation de l'exothermicité de ces étapes réactives avec les acides hexanoïques est liée à l'augmentation de la capacité de donneur d'électrons de la chaîne la plus longue. Par conséquent, nous pourrions conclure que la dégradation est favorisée par les acides carboxyliques à chaînes plus longues. L'acide acétique reste cependant un bon modèle pour individualiser les principales étapes réactives de la formation des complexes de Zn. Nous observons que l'adsorption de l'acide hexanoïque/hexanoate sur la surface de ZnO est favorisée par rapport à la libération de l'ion Zn de la surface pour former des complexes de Zn en accord avec les résultats obtenus pour l'acide acétique. Ces deux réactions étudiées représentent un modèle simplifié des étapes clés des voies de dégradation plus complexes du ZnO. Pour conclure, nous pouvons dire qu'à partir de petits modèles d'agrégats de ZnO et d'acide carboxylique/carboxylate, des résultats intéressants ont été obtenus après l'optimisation de différentes géométries à l'aide de la méthode DFT. Les réactions entre le cluster ZnO et l'acide acétique/acétate ainsi que l'adsorption de l'acide/acétate sur la surface du cluster ont été étudiées. De plus, des modèles plus réalistes avec des clusters ZnO plus étendus et des chaînes plus longues d'acides carboxyliques/carboxylate ont été envisagés. Thermodynamiquement, il est effectivement favorable d'extraire l'atome de zinc du cluster ZnO pour former un savon métallique. Cette voie de réaction est initiée par l'adsorption de l'acide carboxylique/carboxylate sur la surface du pigment qui est plus favorable. Les chaînes alkyles plus longues des acides carboxyliques n'ont pas d'effet significatif sur le cluster en comparant les résultats à ceux des acides acétiques du point de vue structural et énergétique. Ainsi, même un petit modèle d'acide carboxylique est assez bon pour reproduire les propriétés des systèmes étudiés dans lesquels

des résultats raisonnables ont été obtenus. L'approche cluster a été vérifiée à l'aide de l'approche « slab ». Ainsi, nous pouvons explorer différents modèles en utilisant des calculs de « slabs » périodiques. Aussi, on peut étudier des défauts qui pourraient catalyser ces réactions de dégradation.

En photocatalyse, des réactions peuvent avoir lieu en utilisant la lumière et un semi-conducteur: dans ce mécanisme, une paire électron-trou est générée lors de l'exposition d'un matériau semi-conducteur à la lumière, puis l'électron excité est utilisé pour réduire une espèce acceptrice tandis que le trou peut simultanément oxyder une espèce donneuse. Ce travail donne un aperçu des effets de la photocatalyse pour dégrader le coronavirus à l'aide de semi-conducteurs à oxyde métallique TiO_2 et ZnO. Dans cette étude préliminaire, nous nous sommes concentrés sur l'interaction entre TiO_2/ZnO et des modèles phospholipidiques qui ressemblent à l'environnement du coronavirus et pourraient s'adsorber à la surface. Nous avons optimisé un modèle simplifié de phospholipide où les groupes méthyles remplacent les longues chaînes alkyle des acides gras. Nous avons étudié différents modes d'adsorption du phospholopide à la surface de TiO_2. La configuration optimisée la plus stable montre quatre atomes d'oxygène de coordination, deux appartenant au groupe phosphate (adsorbés sur deux centres Ti adjacents par une coordination bidentate pontée) et les deux autres au groupe carboxylate, où l'interaction la plus importante est liée à l'oxygène adsorbé du groupe phosphate et apportant ainsi la plus grande contribution à la stabilisation du système. L'énergétique associée à la liaison de la molécule phospholipidique à la surface de TiO_2 donne des indications sur l'occurrence de ces processus. Nous avons dupliqué la surface de TiO_2 et en comparant les ΔE des réactions d'adsorption nous avons trouvé que le système d'adsorption associé à une plus grande surface est plus favorable que celui de plus petite surface présentant la même géométrie d'adsorption. Cette différence d'énergie peut s'expliquer par les interactions entre les molécules de phospholipides de différentes images qui déstabilisent le système dans les modèles d'oxydes plus petits. Nous évitons ce genre d'interactions en répliquant la surface de manière à considérer le phospholipide comme une véritable molécule isolée, ce qui se traduit par un système d'adsorption plus stabilisé. Nous avons encore optimisé la structure complète du phospholipide en ajoutant les longues chaînes alkyle, comme un modèle pour décrire l'enveloppe du virus. Nous avons étudié les réactions des phospholipides fixant les sites d'adsorption les plus stables avec ou sans les forces de van der Waals, qui peuvent être particulièrement importantes lorsque de si longues chaînes sont impliquées. Nous avons remarqué l'augmentation de la stabilité des réactions d'adsorption par

des chaînes alkyles plus longues. De même, les résultats obtenus à partir de la prise en compte de ces forces sont bien plus favorables que les systèmes n'incluant pas de telles interactions, considérant la même structure d'adsorption. Ceci indique la contribution importante de ces forces sur l'adsorption des phospholipides à la surface. Ces résultats préliminaires mettent en évidence que les molécules de phospholipides peuvent être fortement adsorbées à la surface de TiO_2, ce qui suggère que ce matériau, compte tenu de ses propriétés photocatalytiques bien connues, pourrait être un candidat important pour la purification de l'air des virus. Suivant la même stratégie appliquée au TiO_2, nous avons étudié l'adsorption du phospholipide sur la surface de ZnO pour étudier sa stabilité sur cette surface. L'énergétique associée aux réactions d'adsorption pour ZnO montre une tendance similaire à celle trouvée pour TiO_2. Cependant ZnO montre une plus grande capacité à adsorber les phospholipides. Le ZnO est un meilleur candidat pour adsorber les phospholipides et pourrait donc être un bon matériau également pour dégrader l'enveloppe virale des phospholipides. En conclusion, cette étude préliminaire pour la photocatalyse des oxydes métalliques montre leur capacité à dégrader un virus à enveloppe phospholipidique. Des résultats probant ont été obtenus après optimisation de l'interaction entre les surfaces phospholipidiques et TiO_2/ZnO de différentes géométries à l'aide de la méthode DFT. L'inclusion de chaînes alkyles de phospholipides indique des résultats plus favorables du point de vue énergétique et, en particulier, l'inclusion de forces de van der Waals assure une plus grande stabilité des systèmes étudiés avec les chaînes d'acides gras. Thermodynamiquement, les réactions entre le phospholipide et ZnO donnent des systèmes d'adsorption plus stables que l'adsorption sur TiO_2. Par conséquent, connaissant leurs propriétés photocatalytiques, TiO_2 et ZnO sont tous deux de très bons candidats pour photodégrader la membrane phospholipidique des virus, ce dernier étant censé adsorber les phospholipides de manière plus forte. Cependant, d'autres études devraient être menées pour explorer les mécanismes de photodégradation du coronavirus en utilisant TiO_2 ou ZnO comme photocatalyseur.